UNIVERSITAT POLITÈCNICA DE CATALUNYA
BARCELONATECH
Departament d'Enginyeria Electrònica

"NOVEL METAL INSULATOR METAL CAPACITORS BASED ON ELECTROSPRAYED COLLOIDAL NANOPARTICLES"

Thesis submitted as a compendium of publications in partial fulfillment of the requirement for the PhD Degree issued by the Universitat Politècnica de Catalunya, in its Electronic Engineering Program.

Bremnen Marino Véliz Noboa

Supervisor: Alexandra Bermejo Broto

Barcelona, 2019

Electronic Engineering Department

To my family and to God for blessing my family

Abstract

This work develops a novel capacitor device based on the use of nanotechnology. The device starts from the exiting metal-insulator-metal (MIM) concept, but instead of a continuous insulator layer, dielectric nanoparticles are used. Nanoparticles are mainly of silicon oxide (silica) and polystyrene (PS) and the diameter values are 255nm and 295nm respectively. The nanoparticles contribute to a very high surface to volume ratio and are easily available at low cost. The deposition technology developed in this work is based on the use of the electrospray technique, which is a bottom-up fabrication technology that allows batch processing and achieves a good compromise between large area and low deposition time. With the objective of increasing the deposit surface, the electrospray set-up has been tuned to allow deposition areas from $1cm^2$ to $25cm^2$.

The fabricated devices, the so called nanoparticles metal insulator metal (NP-MIM) capacitors, offer higher capacitance values than a similar conventional capacitor with a continuous insulator layer. In the case of silica NP-MIMs, a factor as high as 1000 of capacitance enhancement is achieved, whereas polystyrene NP-MIMs exhibit capacitance gains in the range of 11. In addition, silica NP-MIMs show capacitive behaviours in a specific frequency ranges which depends on the humidity and thickness of the nanoparticles layers thickness, while polystyrene NP-MIMs always maintain their capacitive behaviour.

The fabricated devices have been characterized by scanning electron microscopy (SEM) measurements complemented with focusing ion beam (FIB) drilling to characterise the topography of the NP-MIMs. The devices have also been characterized by impedance spectroscopy measurements, at different temperatures and humidifies. The origin of the enhanced capacitance is associated in part to humidity in the nanoparticles interfaces. A circuital model based on distributed elements has been developed to fit and predict the electrical behaviour of the NP-MIMs.

In summary, this thesis shows the design, fabrication, characterization and modelling of a new promising nanoparticles metal-insulator-metal capacitor that may pave the way to the development of a novel MIM-supercapacitor technology.

Resumen

Este trabajo desarrolla un novedoso dispositivo condensador basado en el uso de la nanotecnología. El dispositivo parte del concepto existente de metal-aislador-metal (MIM), pero en lugar de una capa aislante continua, se utilizan nanopartículas dieléctricas. Las nanopartículas son principalmente de óxido de silicio (sílice) y poliestireno (PS) y los valores de diámetro son 255nm y 295nm respectivamente. Las nanopartículas contribuyen a una alta relación superficie/volumen y están fácilmente disponibles a bajo costo. La tecnología de depósito desarrollada en este trabajo se basa en la técnica de electrospray, que es una tecnología de fabricación ascendente (bottom-up) que permite el procesamiento por lotes y logra un buen compromiso entre una gran superficie y un bajo tiempo de depósito. Con el objetivo de aumentar la superficie de depósito, la configuración de electrospray ha sido ajustada para permitir áreas de depósito de $1cm^2$ a $25cm^2$.

El dispositivo fabricado, los llamados condensadores de metal aislante de nanopartículas (NP-MIM) ofrecen valores de capacidad más altos que un condensador convencional similar con una capa aislante continua. En el caso de los NP-MIM de sílice, se alcanza un factor de hasta 1000 de mejora de la capacidad, mientras que los NP-MIM de poliestireno exhibe una ganancia de capacidad en el rango de 11. Además, los NP-MIM de sílice muestran comportamientos capacitivos en específicos rangos de frecuencias que depende de la humedad y el grosor de la capa de nanopartículas, mientras que los NP-MIM de poliestireno siempre mantienen su comportamiento capacitivo.

Los dispositivos fabricados se han caracterizado mediante medidas de microscopía electrónica de barrido (SEM) complementadas con perforaciones de haz de iones focalizados (FIB) para caracterizar la topografía de los NP-MIMs. Los dispositivos también se han caracterizado por medidas de espectroscopia de impedancia, a diferentes temperaturas y humedades. El origen de la capacitancia aumentada está asociado en parte a la humedad en las interfaces de las nanopartículas. Se ha desarrollado un modelo de un circuito basado en elementos distribuidos para ajustar y predecir el comportamiento eléctrico de los NP-MIMs.

En resumen, esta tesis muestra el diseño, fabricación, caracterización y modelización de un nuevo y prometedor condensador nanopartículas metal-aislante-metal que puede abrir el camino al desarrollo de una nueva tecnología de supercondensadores MIM.

Acknowledgments

Fist at all, I would like to take the opportunity to express my sincere gratitude to Alexandra Bermejo, for the trust placed in me as a doctoral student. I am grateful for her valuable guidance, as well as her continues support though the course of this thesis. Under her supervision I have learned a lot.

I would like to say thank to Albert Orpella for his estimable collaboration when I needed support. A special thanks to Luis Castañer for sharing his knowledge and experience.

I would like to thank to Gema Lopez, Arnau Coll and the clean room technical staff for the training and support in the management of the different instruments and laboratory equipment. Thanks to Jordi Vives co-author of one of the articles presented here, and thanks to the rest of my colleagues that in one way or another accompanied during the development of this thesis.

Last but not least, I would like thank to all member of my family, to my father for his advice and encouragement, and an exceptional gratitude to my wife and my children for their company, unconditional love and the great effort involved during these last years.

Peace is not just the absence of war. Peace is above all the presence of justice, health, education, social security, decent salaries, basic needs satisfied.

The insulting opulence next to the most intolerable poverty, are also daily bullets against human dignity.

Rafael Correa, former Ecuadorian president.

Contents

List of Figures

List of Tables

CHAPTER I
Introduction

1.1. Context

Nanoparticles are irrupting in the day-by-day, many consumer products are made of nanoparticles in order to benefit our daily life [1], for instance silver nanoparticles are used in shampoos and detergents, or zinc oxide nanoparticles in sunscreens. Silicon oxide nanoparticles are used as an anti-caking agent to increase the taste value and prolong the shelf-life of food, fumed silica oxide nanoparticles are used in toothpastes and cosmetics as a light abrasive additive. Within the energy storage research area, the inclusion of carbon nanotubes, graphene, transition metal oxide, silicon and silica nanoparticles as active material in electrodes, are improving the performance of the supercapacitors [2] [3] [4] and lithium batteries [5] [6].

The revolutionary growing of the technologies at the nanoscale has allowed the synthesis, manipulation and characterization of different kind of nanoparticles and in turn the fabrication of novel nanostructures. On one hand, the fabrication of nanostructures has been dominated by top-down [7] approaches as a legacy of the semiconductor industry, thus various new, but expensive nanolithographic techniques [8] such as electron beam lithography, x-ray lithography, scanning probe lithography and nanoimprinting have emerged to improve the pattering resolution at the nanometre scale. On the other hand, bottom-up assembly approaches, where the nanostructures are self-assembled from smaller pieces, are pretty cheaper and faster than top-down assembly approaches [9]. In many applications, such as the ones within the photonic research field, monodisperse nanoparticles are used to make periodic and ordered nanostructures termed as colloidal crystals (opals and inverse opal) self-assembled by bottom-up methods such as drop casting [10] [11], vertical deposition [12], spin-coating [13], dip-coating [14], shear ordering [15], Lagmuir-blodgett [16] and electrospray techniques among others [17].

Due to the low cost and simplicity of the electrospray technique, the MNT group has developed a specific set-up using this technology as an innovative method to self-

assemble silica [18] and polystyrene [19] nanoparticles in order to fabricate metamaterials [20]. However, as far as we know, similar nanostructures have not been reported yet for energy store applications. It is in this context when it comes down to the idea of using dielectric nanospheres instead of a continuous dielectric film as an insulating layer to fabricate Metal Insulator Metal (MIM) capacitors. Preliminary evidence based on impedance spectroscopy characterisation suggested that in this new type of MIM capacitor, the effect of using these nanospheres may cause an increase on the expected capacitance for an equivalent conventional MIM capacitor with continuous dielectric layer of same dimensions, signifying that these new devices are promising for its use as supercapacitors [21].

Thereby, the main aim of this PhD work is to explore an alternative Metal-Insulator-Metal (MIM) device using electrosprayed dielectric nanoparticles for energy store applications. Design and fabrication of the MIM capacitor is carried out using different dielectric nanoparticles materials, mainly monodisperse silicon oxide and polystyrene nanospheres. This work shows a compressive analysis of the MIM capacitor using impedance spectroscopy characterisation to model the physics in the interfaces of the MIM and the physical phenomena of electrical double layer that could be present in the nanospheres interfaces.

1.2. Thesis structure

This thesis is presented as a compendium of papers published in recognized international journals in the field of nanotechnology and electrochemistry. The document is structured into five charters. The first chapter is the introduction of the thesis including the main goals, the design of the capacitors and the experimental characterization methods.

Chapter 2 shows the state of the art, focused on high specific capacitance MIM capacitors and supercapacitors. As it will be seen later, impedance spectroscopy equivalent circuit usually employed to model supercapacitors resulted suitable to model the nanoparticles metal-insulator-metal (NP-MIM) capacitors shown in this thesis.

Chapter 3 contains the full text of the three publications and Chapter 4 the global discussion of the results and main performance parameters following to the set goals.

Chapter 5 shows the conclusions derived from this thesis and the potential future lines of research. Finally, the appendix includes conference publications and complementary information that has not been published yet, but are relevant to the thesis.

1.3. Objectives

Main objective

The purpose of this thesis is to research on the understanding and fabrication of nanoparticles based Metal-Insulator-Metal (NP-MIM) structures using electrosprayed dielectric nanospheres as the insulator layer, exploring the performance by impedance spectroscopy characteristics to analyse its use as an alternative energy store device.

Specific objectives

- Design and fabrication of NP-MIM capacitors, where the insulator layer is deposited by electrospraying of monodisperse dielectric nanoparticles, mainly silicon oxide and polystyrene materials.
- Impedance spectroscopy characterization and modelling of the NP-MIM structures.
- Analyse the use of theses NP-MIM capacitors as energy store devices.
- Scaling-up of the nanoparticles based structures deposition area using electrospray technique.
- Analyse the possibility of using these NP-MIM capacitors as humidity sensors.

1.4. Design

Figure.1a shows a generic schema of the nanoparticles metal insulator metal (NP-MIM) structure. Figure.1b shows the hypothetical conventional equivalent (same dimensions) MIM capacitor with a continuous insulator layer.

Aluminium layers were employed both as bottom electrode and top electrode using microelectronic standard fabrication process steps. Electrospray technique is used to

deposit the nanoparticles by means of a high voltage between the bottom electrode and a needle that acts as nanoparticle gun. This fabrication process steps are the following:

A. Clean the glass microscope slide substrate sequentially with acetone, propanol, deionized water and nitrogen to remove dust or any residual contaminant from the surface.

B. Pour on the glass substrate surface the SPR 220-7 photoresist and to spin it in order to obtain a 7μm thick photoresist film.

C. Post-bake process to remove the excess solvent in order to dry and stabilize the photoresist film.

D. Expose with ultraviolet light the photoresist through a mask (nano-MIM2 base mask) which contains the pattern of the bottom electrodes and paths.

E. Develop the photoresist using a MF24 solution to remove the exposed photoresist.

F. Deposit an aluminium layer on the sample using thermal evaporation deposition.

G. Definition of the bottom aluminium layout on the glass substrate by a lift-off process.

H. A new photoresist film is spun coated on the sample surface.

I. New lithography process (nano-MIM2 pous mask) and development are performed to open two windows in the photoresist, one window for the NP-MIM structure and the other window for the electrical connection with the bottom electrode.

J. The nanoparticles are electrosprayed on the corresponding opened window on the bottom electrode.

K. Finally, the top electrode is a thin aluminium film deposited onto the nanoparticles and onto the photoresist layer using a shadow mask.

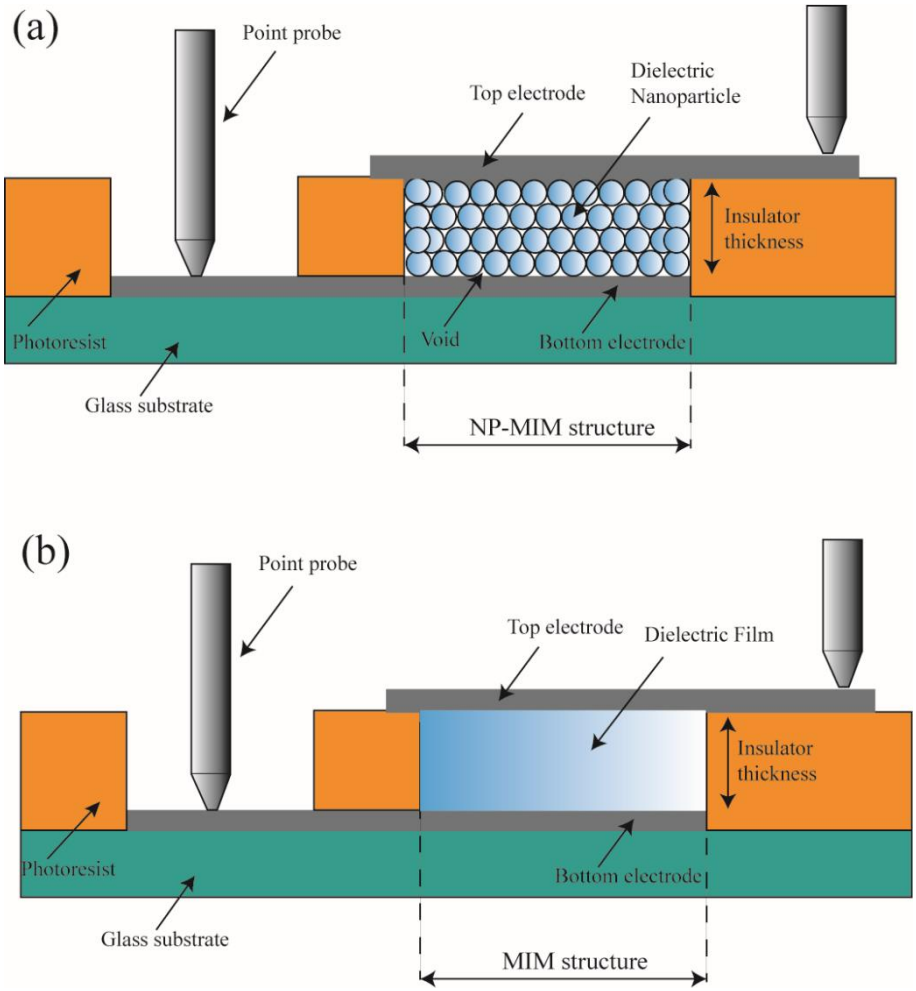

Figure 1. (a) Nanoparticles Metal-Insulator-Metal structure schema, (b) equivalent conventional Meta-Insulator-Metal schema.

Electrospray deposition method is a low cost, rapid and simple technique that can work at room temperature. The electrospray system consists on an infusion pump, a microfluidic tube, a needle, a high voltage source and a digital camera, as it is observed in Figure 2. The nanoparticle suspension contained in a syringe is pressed at a constant flow by the infusion pump, then the suspension travels through the fluidic microchannel to the positively polarized needle, where the suspension is electrosprayed focusing the nanoparticles on the substrate. The surface substrate is connected to the negative terminal of the high voltage source. A digital camera inspects the formation of the cone of Taylor in the needle tip. Taylor cone is stable shape created between the capillary and the jet region when the potential difference reaches a threshold value.

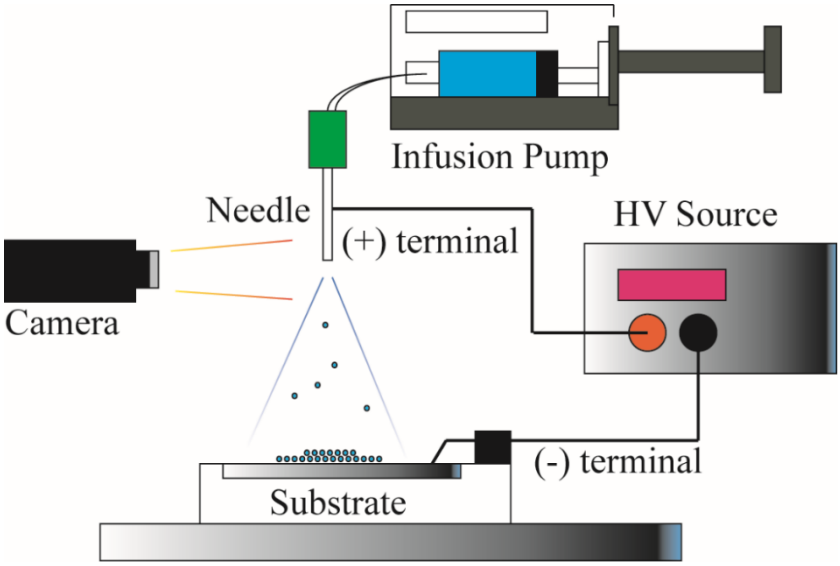

Figure 2. Schematic of how the colloidal nanoparticles are deposited by an electrospray system.

Three individual masks are used in the NP-MIM structure fabrication; each mask containing eight samples, that contains three NP-MIM structures as the same time. The first mask (Figure 3b) is designed to fabricate the bottom electrode. The second mask, (Figure 3a) patterns the photoresist, and the last mask (Figure 3c) is the shadow mask used for top electrode metal deposition. The NP-MIM fabrication may potentially avoid any photolithography steps, by using shadow masks, thus decreasing the cost of the final device.

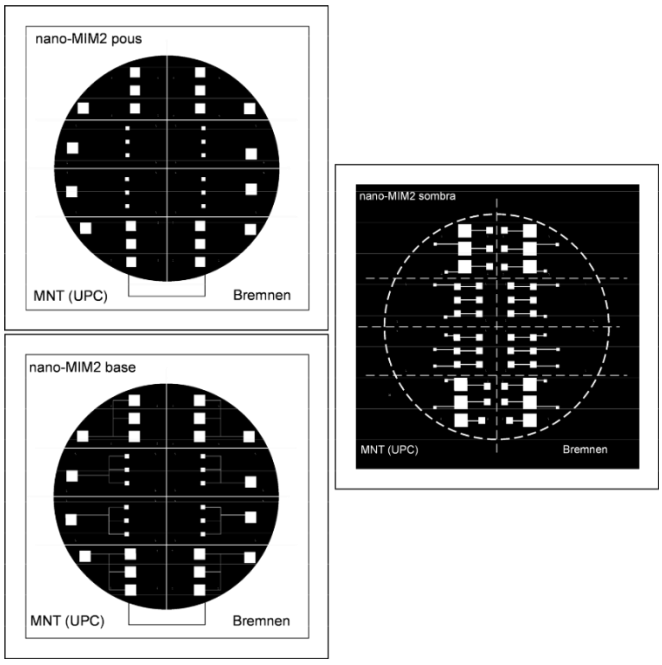

Figure 3. Designed masks used for the photolithography process in the fabrication of NP-MIM structures.

1.5. Journals papers

The following papers form part of the compendium of publications according to the goals of this thesis.

1.5.1. Paper #1

Paper [22] entitled: “Impedance modelling of silica nanoparticle metal insulator metal capacitors”. Published in Electrochimica Acta.

Brief description: “In this paper, some silica NP MIM capacitors are fabricated with 255 nm diameter silica nanospheres as insulator layer using electrospray technique, resulting in an enhanced capacitance (up to 1000) compared to a conventional planar configuration. The capacitance enhancement is found to be associated to charge in the nanoparticle interfaces. Besides, an in-depth study of electrochemical impedance spectroscopy modelling and charge-discharge transients is provided. Impedance spectroscopy measurements fitted very well with a Randles equivalent circuit formed by sub-circuits that describes the nanoparticles and the nanoparticle-metal interfaces. Maltab simulations prove that the charge-discharge transient measurements perfectly agree with the Randles equivalent circuit.”

1.5.2. Paper #2

Paper [23] entitled: “Capacitance study of a polystyrene nanoparticle capacitor using impedance spectroscopy”. Published in Nanotechnology.

Brief Description: In this paper, a polystyrene NP MIM capacitor is fabricated with 295nm diameter polystyrene nanoparticles as insulator layer using electrospray technique. Measured capacitance values are up to 11.7 larger than the expected for a conventional metal insulator metal capacitor of planar geometry and continuous polystyrene layer calculated with the classic formula. Electrochemical impedance spectroscopy modelling showed the deterioration of the metal-nanoparticles interfaces and a slight decrease in the capacitance with the temperature increase which is associated to charges localized at the nanoparticles interfaces due to the environmental humidity.

1.5.3. Paper #3

Paper [24] entitled: “Large area deposition of ordered nanoparticle layers by electrospray”. Published in Colloid and Interface Science Communications.

Brief description: In this paper, the deposition area scaling-up of the nanoparticle based structures is performed. Two approaches are implemented using the electrospray technique. An area of 25 cm^2 is achieved using an electrospray system formed by an array of four needles, while up to 7.5 cm^2 areas are achieved by using a guard ring electrode placed in the electrospray jet trajectory. COMSOL simulations of the electric field distribution are carried out by the two electrospray configurations.

1.6. Characterization Methods

In this thesis, two characterizations methods have been mainly used:

Electrical Impedance Spectroscopy (EIS) characterization was carried out to analyses the electrical behaviour of the NP-MIM capacitors in different frequency ranges. The HIOKI IM3590 impedance analyser and the Agilent 4294A impedance analyser have been used for this purpose.

Scanning electron microscopy (SEM) and Focused Ion Beam (FIB) characterization was used to determine the nanoparticles diameters, the orography and the thickness of the nanoparticles layers. The SEM microscopy used was the ZEIS NEON 40.

1.6.1. Electrical Impedance Spectroscopy (EIS)

There are many impedance measurement methods [25] such as bridge method, I-V method, network analysis method or auto-balancing bridge method. The last one is the used because it owns wide frequency coverage with high accuracy. Electrical impedance spectroscopy [26] is the most used characterisation tool in electrochemical materials and devices analysis. All methods are based on the measurement of an alternating current $\tilde{I}$ resulted from the application of a small sinusoidal wave potential $\tilde{V}$ at a wide range of frequencies.

$$Z = \frac{\tilde{V}}{\tilde{I}} = |Z|(\cos\theta + j\sin\theta) \quad (1)$$

Where |Z| and θ are the module and phase of the impedance and they are dependent on the frequency. The real and the imaginary impedance components, Z' and Z'' are depicted by the equations (2) and (3):

$$Z' = |Z|\cos\theta \quad (2)$$

$$Z'' = |Z|\sin\theta \quad (3)$$

The admittance can be calculated from Z as (4):

$$Y = \frac{1}{Z} = Y' + jY'' \quad (4)$$

The values of |Z|, θ, Z', Z'', *Y*' and *Y*'' data can be acquired by an impedance analyser including the established frequency range.

The complex capacitance [27] [28] depends on the angular frequency and it is defined as (5):

$$C^* = \frac{1}{j\omega Z} = C' + jC'' = -\frac{Z''}{\omega|Z|^2} + j\frac{Z'}{\omega|Z|^2} \quad (5)$$

Where C' is the real capacitance or simply termed as capacitance, corresponds to the one measured by constant charge-discharge current. For a MIM structure of parallel plates configuration, C' defined as (6):

$$C' = \epsilon\frac{A}{d} = -\frac{Z''}{\omega|Z|^2} \quad (6)$$

Where *A* is the electrode area, *d* is the dielectric thickness (or separation between the parallel plates), and ϵ is the dielectric permittivity of the dielectric.

The Imaginary Capacitance C'' (5) is related to the energy dissipation including both dielectric loss and conductivity.

Other useful equations are the normalized powers respect to the apparent power defined as:

$$P/|S| = \cos\theta = Z'/|Z| \quad (7)$$

$$Q/|S| = \text{sen}\,\theta = Z''/|Z| \quad (8)$$

1.6.2. Impedance modelling

The usual modelling elements used in electrical impedance spectroscopy are: Resistor R, Capacitance C, Constant Phase element (CPE) [29] and Warburg element W [30].

The resistor is usually a charge transfer resistor (also named polarization resistance) that is the resistance of the electrons through an interface (as electrode-electrolyte) occurred when a voltage is applied. The capacitance states for a double layer capacitance that is the space charge stored at an interface when applying a voltage. A constant phase element is a frequency dependent element associated to a distributed capacitance (as a double layer capacitance) due to a non-uniform potential and current distribution caused by rough surfaces, heterogeneities or electrode porosity. The Warburg element is another frequency element used extensively to model the ions diffusion in a material. The Warburg impedance is observed at low frequencies, exhibiting a phase shift of 45º.

Table.1 sums up the description of each element.

Table 1. Basic modelling elements used in electrical impedance spectroscopy

Element	Impedance Z		Description
Resistor	R	**(9)**	*R* is the resistance
Capacitor	$\frac{1}{j\omega C}$	**(10)**	*C* is the capacitance
Constant Phase element	$\frac{1}{(j\omega)^{\alpha}Q}$	**(11)**	*Q* is the constant phase coefficient, 0<α<1
Warburg element (semi-infinite)	$\frac{\sqrt{2}A_W}{(j\omega)^{1/2}} = \frac{A_W}{(\omega)^{1/2}}(1-j)$	**(12)**	A_W is the Warburg coefficient
Inductor	$j\omega L$	**(13)**	*L* is the inductance

A Nyquist plot also known as complex plane impedance plot, it is the graphical representation of the impedance imaginary component as a function of the impedance real

component. The Nyquist plot of an ideal capacitor (or an ideal polarized electrode) consists on a capacitor in series with a resistor. The impedance Z, may be represented as:

$$Z = R - j\frac{1}{\omega C} \quad (14)$$

Where C and R are the capacitor and resistor values, respectively.

Where C and R are the capacitor and resistor values, respectively. Figure 4 shows the result of a Matlab circuit simulation consisting on capacitor C=60µF in series with a resistor R=100Ω, in a frequency range from 0.1Hz-10kHz. As it can be seen in Figure 4, the Nyquist plot is a vertical line for all the frequency range. At high frequencies, the imaginary part is cutting the real axis in value that represents the resistor value R.

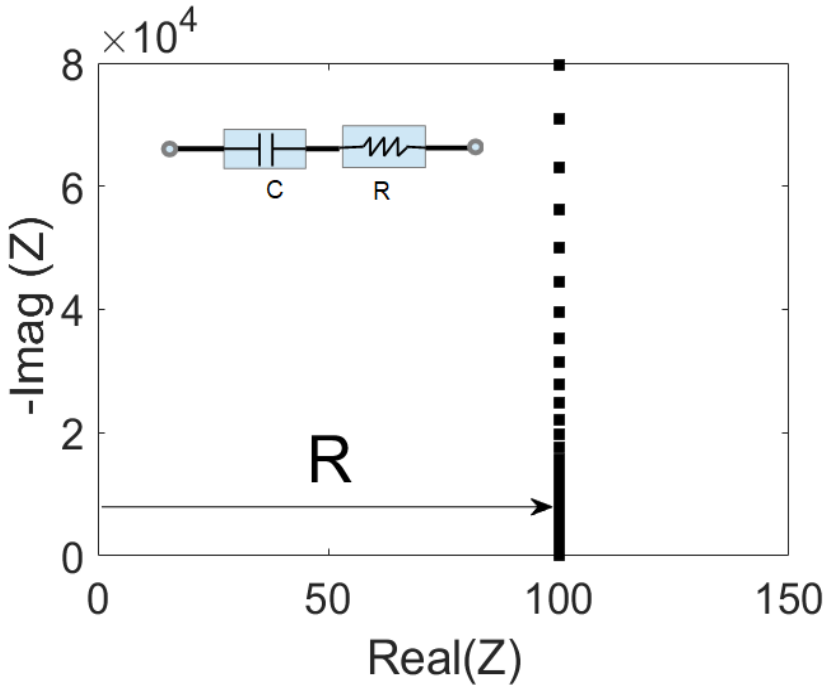

Figure 4. Ideal capacitor and its Nyquist plot. C=60µF, R=100Ω

Figure 5 shows the simulation of a model for a non-ideal polarisable electrode, named Simplified Randle circuit [31], that includes a contact resistor Rs in series with the parallel of a double layer capacitance, C [32] and the so-called charge transfer resistor R [33] [34].

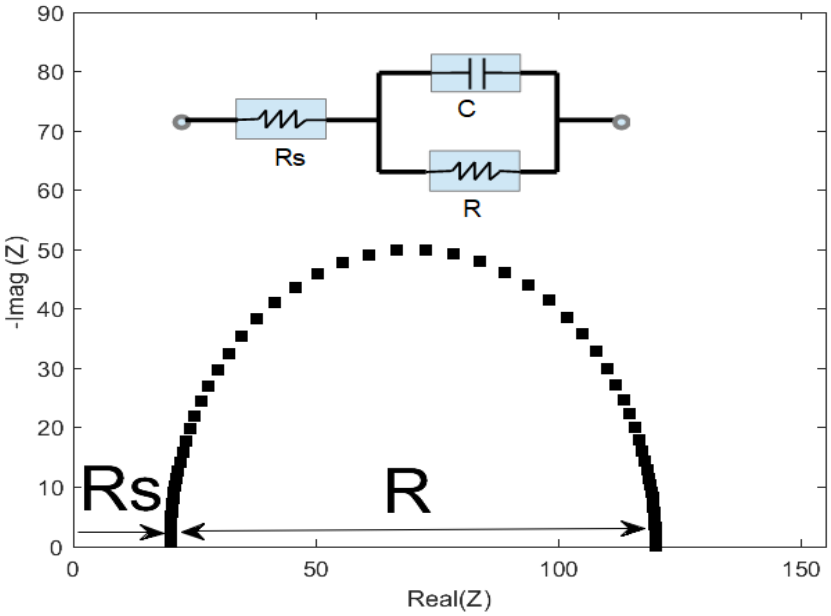

Figure 5. Simplified Randle Circuit and its Nyquist plot. C=60µF, R=100Ω, Rs=20 Ω.

The parameter values are Rs=20Ω, R=100 and C=60µF. As it can be seen in Figure 5, the Nyquist plot of the Simplified Randle model is represented by a semicircle of diameter R. The Simplified Randle impedance model is represented by the equation (13):

$$\mathrm{Z} = R_S + R||\frac{1}{j\omega C} = R_S + \frac{1}{\frac{1}{R} + j\omega C} = \left\{R_S + \frac{R}{1+(\omega RC)^2}\right\} - j\left\{\frac{\omega CR^2}{1+(\omega RC)^2}\right\} \quad (15)$$

The real component of the impedance tends to Rs, at high frequencies, whereas, it tends to Rs+R at low frequencies. Due to the micro or nanoscopic roughness surface at the interfaces, a capacitor is usually not enough to model a real device. Therefore, the capacitor can be replaced by a constant phase element. The effect in the Nyquist plot of the introduction of a constant phase element is the depression of the semicircle.

In Figure 6 is showed the equivalent circuit and Nyquist plot for a Randle model which takes into account the diffusion of carries (Aw). The parameters simulated were R=100Ω C=60µF, Rs=20Ω and Aw=20Ω$(jw)^{1/2}$. The Impedance for Randle model showed in Figure 6 is:

$$Z = Rs + \frac{\left(R + \frac{\sqrt{2}A_W}{(j\omega)^{1/2}}\right)\frac{1}{j\omega C}}{R + \frac{\sqrt{2}A_W}{(j\omega)^{1/2}} + \frac{1}{j\omega C}} \equiv Rs + \frac{1}{\frac{1}{R + \frac{\sqrt{2}A_W}{(j\omega)^{1/2}}} + j\omega C} \quad (16)$$

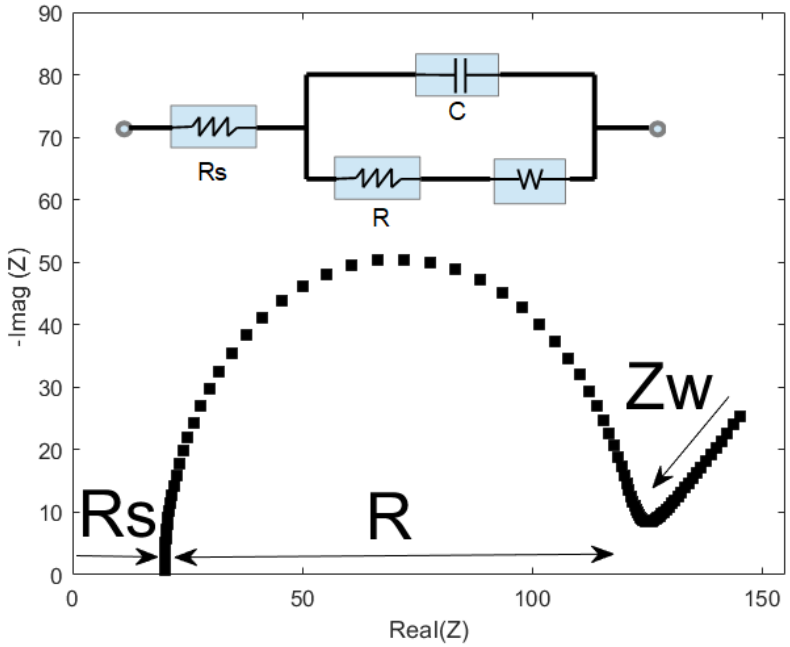

Figure 6. Randle circuit and its Nyquist plot. C=60µF, R=100Ω, Rs=20 Ω, Aw=20 Ω(jw)$^{1/2}$

The sloped straight line observed in Figure 6 is due to the Warburg impedance, also known as mass transfer impedance. Since Warburg real component and Warburg imaginary component are identical (see equation 10), the straight line has a slope 1. This impedance is dominant at low frequencies, but as the frequency increases, the Warburg impedance becomes negligible [31] [27].

A more complex model used for solid state devices is the Voigt structure, which consists in using parallel RC circuits connected in series, but without Warburg elements. The equivalent circuit is showed in Figure 7 and the impedance is calculated [33] as:

$$Z = \sum_{i=1}^{n} \left(\frac{1}{\frac{1}{R_i} + j\omega C_i} \right) \quad (17)$$

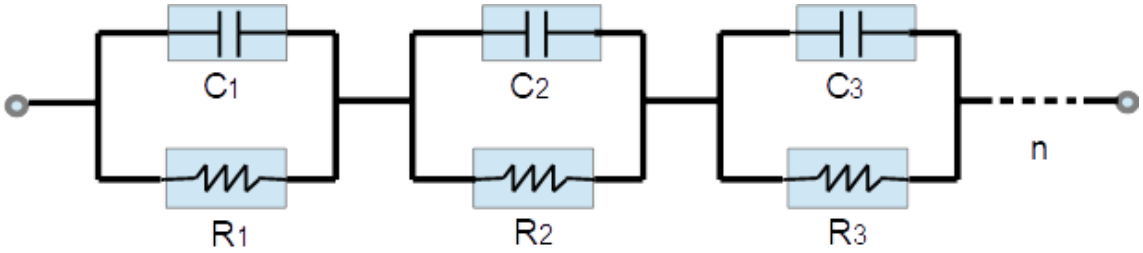

Figure 7. Voigt circuit model.

1.6.3. Scanning Electron Microscopy (SEM) and Focused Ion Beam (FIB)

SEM is a powerful method to take three dimensional images and thus topographical information of the devices at the nanoscopic scale. A SEM microscope uses a beam of electrons rather than a beam of light. The electrons are energised and focused using electrostatic and electromagnetic fields. In optical microscopes, the resolution is mainly limited to the wavelength of the light used. SEM microscopes overcome this drawback because electrons accelerated to high velocities can achieve shorter wavelengths than visible light. The incident electrons that impact with the sample generate secondary electrons, back scattered electrons and x-rays. SEM microscopes are based on the detection of secondary emission of electrons [35].

SEM microscopes usually provide a resolution between 1 nm and 10 nm [35]. Another characteristic is that they have large depth of field (focus depth), which allows a large part of the sample to be focused at the same time. The samples must be solids, as well as metallic or conductive, otherwise, the dielectric samples require to be coated with a thin conductive material as carbon. Additionally, SEM microscopes are expensive, require high vacuum conditions and are extremely sensitive to vibration.

A Focused Ion Beam (FIB) [36] instrument uses a beam of ions instead of electrons being gallium (Ga) the most common ions used in commercial FIB instruments. The ions are able to mill the sample surface thus allowing the micro or nano machining of the sample. Figure 8a shows the SEM/FIB microscope located in the Multiscale UPC facility [37].

Figure 8b and Figure 8c shows nanoparticles layer images taken with the SEM/FIB microscope.

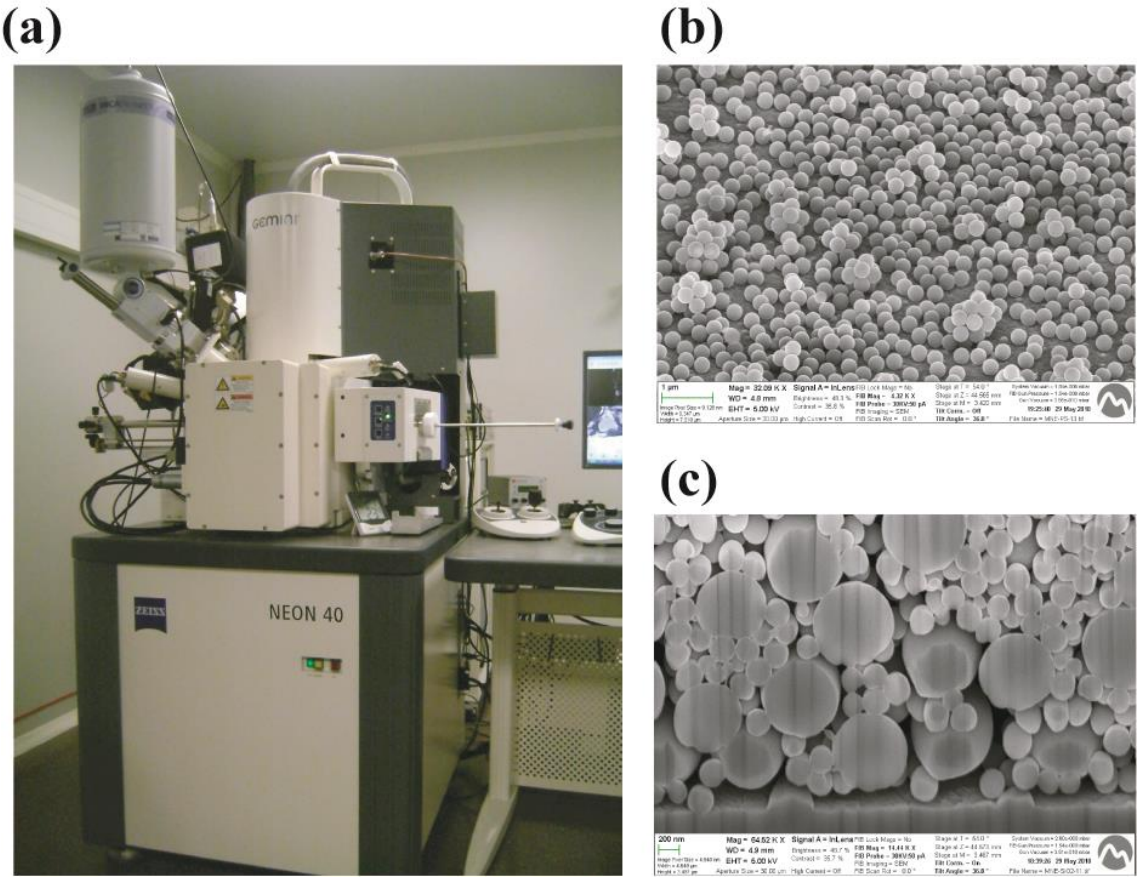

Figure 8. (a) Image of the SEM microscope of the UPC Multiscale facility, (b) SEM image of monodisperse nanoparticles (C) SEM images of nanoparticles of two sizes.

1.7. References

[1] C. Contado, “Nanomaterials in consumer products: a challenging analytical problem,” vol. 3, no. August, pp. 1–20, 2015.

[2] N. Devillers, S. Jemei, M.-C. Péra, D. Bienaimé, F. Gustin, Review of characterization methods for supercapacitor modeling, Journal of Power Sources (2013).

[3] L. F. Aval, M. Ghoranneviss, and G. B. Pour, “High-performance supercapacitors based on the carbon nanotubes, graphene and graphite nanoparticles electrodes,” Heliyon, no. September, p. e00862, 2018.

[4] B.-S. Lou, P. Veerakumar, S.-M. Chen, V. Veeramani, R. Madhu, and S.-B. Liu, “Ruthenium nanoparticles decorated curl-like porous carbons for high performance supercapacitors,” Sci. Rep., vol. 6, no. 19949, 2015.

[5] M. Aghajamali, H. Xie, M. Javadi, W. P. Kalisvaart, J. M. Buriak, and J. G. C. Veinot, “Size and Surface Effects of Silicon Nanocrystals in Graphene Aerogel Composite Anodes for Lithium Ion Batteries,” Chem. Mater., vol. 30, no. 21, pp. 7782–7792, Nov. 2018.

[6] G. Tan et al., “Solid-State Li-Ion Batteries Using Fast, Stable, Glassy Nanocomposite Electrolytes for Good Safety and Long Cycle-Life,” Nano Lett., vol. 16, no. 3, pp. 1960–1968, 2016.

[7] P. Iqbal, J. A. Preece, and P. M. Mendes, “Nanotechnology: The ‘ Top-Down ’ and ‘ Bottom-Up ’ Approaches,” 2012.

[8] G. Venugopal and S. Kim, “Nanolithography,” in Advances in Micro/Nano Electromechanical Systems and Fabrication Technologies, IntechOpen, 2013.

[9] H. Zheng and S. Ravaine, “Bottom-Up Assembly and Applications of Photonic Materials,” Crystals, vol. 6, no. 5, p. 54, 2016.

[10] J. Zhou et al., “Three-dimensional photonic band gap structure of a polymer-metal composite,” Appl. Phys. Lett., vol. 76, no. 23, p. 3337, 2000.

[11] A. Yadav et al., “Spectral properties of self-assembled polystyrene nanospheres photonic crystals doped with luminescent dyes,” Opt. Mater. (Amst)., vol. 35, no. 8, pp. 1538–1543, 2013.

[12] P. Jiang, J. F. Bertone, K. S. Hwang, and V. L. Colvin, “Single-crystal colloidal multilayers of controlled thickness,” Chem. Mater., vol. 11, no. 8, pp. 2132–2140, 1999.

[13] P. Jiang and M. J. McFarland, “Large-scale fabrication of wafer-size colloidal crystals, macroporous polymers and nanocomposites by spin-coating,” J. Am. Chem. Soc., vol. 126, no. 42, pp. 13778–13786, 2004.

[14] C. Deleuze, B. Sarrat, F. Ehrenfeld, S. Perquis, C. Derail, and L. Billon, “Photonic properties of hybrid colloidal crystals fabricated by a rapid dip-coating process,” Phys. Chem. Chem. Phys., vol. 13, no. 22, p. 10681, 2011.

[15] R. M. Amos, J. G. Rarity, P. R. Tapster, T. J. Shepherd, and S. C. Kitson, “Fabrication of large-area face-centered-cubic hard-sphere colloidal crystals by shear alignment,” Phys. Rev. E, vol. 61, no. 3, pp. 2929–2935, Mar. 2000.

[16] M. Szekeres et al., “Ordering and optical properties of monolayers and multilayers of silica spheres deposited by the Langmuir–Blodgett method,” J. Mater. Chem., vol. 12, no. 11, pp. 3268–3274, 2002.

[17] M. Grzelczak, J. Vermant, E. M. Furst, and L. M. Liz-marza, “Directed Self-Assembly of Nanoparticles,” Am. Chem. Soc. Nano, vol. 4, no. 7, pp. 3591–3605, 2010.

[18] A. Coll, S. Bermejo, and L. Castañer, “Self-assembly of ordered silica nanostructures by electrospray,” Microelectron. Eng., vol. 121, pp. 68–71, 2014.

[19] A. Coll, S. Bermejo, D. Hernández, and L. Castañer, “Colloidal crystals by electrospraying polystyrene nanofluids,” Nanoscale Res. Lett., vol. 8, no. 1, p. 26, 2013.

[20] J. F. Galisteo-Lõpez, M. Ibisate, R. Sapienza, L. S. Froufe-Pérez, Ú. Blanco, and C. Lõpez, “Self-assembled photonic structures,” Adv. Mater., vol. 23, no. 1, pp. 30–69, 2011.

[21] B. Véliz, S. Bermejo, A. Coll, and L. Castañer, “Metal-insulator-metal capacitor using electrosprayed nanoparticles,” Appl. Phys. Lett., vol. 105, no. 1, pp. 1–5, 2014.

[22] B. Véliz, S. Bermejo, A. Orpella, and L. Castañer, “Impedance modeling of silica nanoparticle metal insulator metal capacitors,” Electrochim. Acta, vol. 280, pp. 62–70, 2018.

[23] B. Véliz, A. Orpella, and S. Bermejo, “Capacitance study of a polystyrene nanoparticle capacitor using impedance spectroscopy,” Nanotechnology, vol. 30, no. 40, p. 8, 2019.

[24] B. Véliz, S. Bermejo, J. Vives, and L. Castañer, “Large area deposition of ordered nanoparticle layers by electrospray,” Colloid Interface Sci. Commun., vol. 25, pp. 16–21, 2018.

[25] Keysight Technologies, “Impedance Measurement Handbook, A guide to measurement technology and techniques, 6th Edition - Application Note.” [Online]. Available: https://literature.cdn.keysight.com/litweb/pdf/5950-3000.pdf. [Accessed: 04-Jul-2019].

[26] L. J Brad, Allen & R Faulkner, Electrochemical Methods: Fundamentals and Applications. JOHN WILEY & SONS INC, 2000.

[27] C. Rabelais, “TUTORIALS P ROGRAMME ISEE15Cap,” in 4to International Symposium on Enhanced Electrochemical Capacitors., 2015, no. June.

[28] C. Yang, C.-Y. V. Li, F. Li, and K.-Y. Chan, “Complex Impedance with Transmission Line Model and Complex Capacitance Analysis of Ion Transport and Accumulation in Hierarchical Core-Shell Porous Carbons,” J. Electrochem. Soc., vol. 160, no. 4, pp. H271–H278, 2013.

[29] J. Jorcin, M. E. Orazem, P. Nadine, and B. Tribollet, “CPE analysis by local electrochemical impedance spectroscopy,” vol. 51, pp. 1473–1479, 2006.

[30] J. R. M. E. Barsoukov, Impedance Spectroscopy: Theory, Experiment, and Applications, Second. John Wiley & Sons, 2005.

[31] A. I. Zia and S. C. Mukhopadhyay, “Impedance Spectroscopy and Experimental Setup,” in Electrochemical Sensing: Carcinogens in Beverages, vol. 20, Springer International Publishing Switzerland 2016, 2016, pp. 21–37.

[32] H. Ji et al., “Capacitance of carbon-based electrical double-layer capacitors,” Nat. Commun., vol. 5, no. Cmcm, pp. 1–7, 2014.

[33] D. Vladikova, “The Technique of the Differential Impedance Analysis,” in Advanced Techniques for Energy Sources Investigation and Testing, 2004, no. May, pp. 1–28.

[34] B. Pandit, D. P. Dubal, P. Gómez-Romero, B. B. Kale, and B. R. Sankapal, “V2O5 encapsulated MWCNTs in 2D surface architecture: Complete solid-state bendable highly stabilized energy efficient supercapacitor device,” Sci. Rep., vol. 7, no. January, pp. 1–12, 2017.

[35] R.F. Egerton, Physical Principles of Electron Microscopy. Springer, 2005.

[36] F. A. Giannuzzi, Lucille A; Stevie, Introduction to Focused Ion Beams, 1st ed. Springer US, 2005.

[37] U. P. de Catalunya, “Barcelona Research Center in Multiscale Science and Engineering,” 2019. [Online]. Available: https://multiscale.upc.edu/en/infrastructure/desktop-sem. [Accessed: 03-Sep-2019].

CHAPTER II

Thesis Background

2.1. MIM capacitors

2.1.1. Planar-MIMs.

Conventional MIM capacitors are typically electrostatic capacitors having low parasitic capacitances, low parasitic resistances and reliable capacitive characteristics. They are frequently used in radio frequency (RF) applications and analog mixed signal (MS) integrated circuits to function as passive components for filters, oscillators, couplers and analog to digital (or digital to analog) converters. Figure 9 shows the schematic of a typical MIM capacitor that is integrated in the back-end of line (BEOL) [1], that is, the last step of the integrated circuit manufacturing line where metal interconnect layers, insulator layers, vias and pads are fabricated.

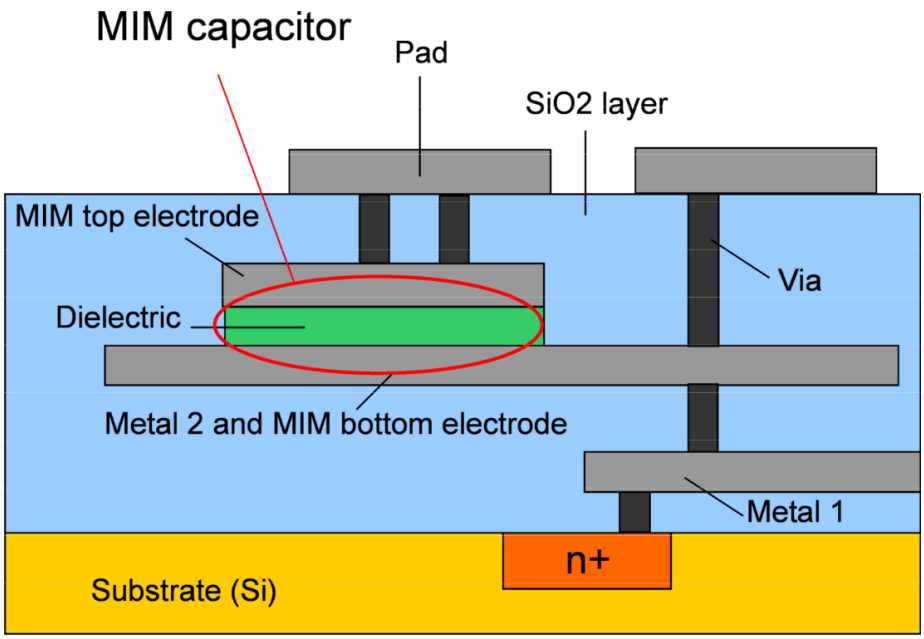

Figure 9. Schematic of an integrated MIM capacitor.

MIM capacitors are integrated in embedded components such as microprocessors, RAM memories, graphical processing units, Wi-Fi and Bluetooth transceivers, etc. The growing

demand of small and functional electronic devices such as mobile phones or tables, has given rise to the Systems On Chips (SoC) [2]. A SoC is a chip that packages computing components into a single chip. Therefore, optimization and cost reduction of passive components as MIM capacitors imply advances in the manufacture of MS and RF integrated circuits that will be reflected in the performance and integration of the SoCs.

An important parameter defining a MIM capacitor is the capacitance density that is the capacitance per unit area defined as:

$$C_d = \frac{k\epsilon_o}{d} \quad \textbf{(18)}$$

Where *k* is the relative permittivity of the dielectric material, ϵ_O is the vacuum dielectric constant (8.85×10^{-14} F/cm) and *d* is the dielectric thickness.

A term used for the MIM (or MOS) capacitors designers is the equivalent oxide thickness (EOT) that is defined as:

$$EOT = \left(\frac{3.9}{k}\right) IT_{high-k} \quad \textbf{(17)}$$

Where *k* is the relative dielectric constant of the high-k dielectric and $IT_{high\text{-}k}$ is its thickness, 3.9 is dielectric constant of the SiO_2. The EOT is equal to the silicon oxide layer thickness needed to produce the same capacitance as the high-k dielectric being used.

Ultra Large Scale Integration (ULSI) technology requires from MIM capacitors fabrication techniques carried out at low deposition temperatures (≤400 ° C). Silicon Oxide (SiO_2) and Silicon Nitride (Si_3N_4 or sometimes abbreviated as Nitride) are the classical dielectrics used in MIM capacitors providing both good linearity of voltage and temperature coefficients [3].

According to the International Technology Roadmap of Semiconductor (ITRS), the expected capacitance density in 2021for future MIMs in RF applications is in the range of 12fF/μm^2 (1.2μF/cm^2) [4] [5] with a leakage current less than 10nA/cm^2. Till now the main strategy to improve the MIMs performance is the use of high relative dielectric constants (high k) materials. Thus high k-dielectric materials [6] are of special interest to achieve higher capacitance densities. Some example are aluminum oxide (Al_2O_3) [7]

(*k*=8.5), hafnium oxide (HfO_2) [8] (*k*=22), lanthanum oxide (La_2O_3) [9] (*k*=30), titanium oxide (TiO_2) [10] [11] (*k*=80). Table 2 shows a list of high-k dielectric materials with their dielectric constant, band gap and density values.

Table 2. Main characteristics of dielectric materials [6] [12] [13]**.**

Dielectric material	Relative dielectric constant	Energy band gaps (eV)	Density (g/cm^3)
SiO_2	3.9	8.9	2.196
Si_3N_4	7.5	5	3
Al_2O_3	8.5	6.2	3.01
$HfSiO_4$	11	6.5	-
HfO_2	22	5.9	9.09
Ta_2O_5	22	4.4	8.316
ZrO_2	25	5.8	6.19
La_2O_3	30	6	6.5
a-$LaAlO_3$	30	5.6	-
TiO_2	80	3.5	3.2
$SrTiO_3$	2000	3.2	5.17

At the same time, the MIM capacitors must have high band gap, because dielectrics with a high energy band gap have low leakage current. Therefore, in order to decrease the leakage current, ternary metal oxides or combinations of stacked dielectric insulators are also being investigated [14] [15] [16]. For example a bilayer Al_2O_3/SiO_2 MIM capacitor [17] deposited with plasma enhanced atomic layer deposition (PEALD) at 200 °C showed a capacitance density of 10.1fF/μm^2 (1.01 $\mu F/cm^2$) and a leakage current density of 6.8 nA/cm^2 at 1V, where the low leakage current can be attributed to the SiO_2 layer.

Figure 10 shows an atomic layer deposited $Al_2O_3/ZrO_2/Al_2O_3$ MIM capacitor example [18] using a microwave annealing of 1400W for 5 minutes that exhibits a capacitance density of 9.06fF/μm^2 (0.9 $\mu F/cm^2$) and a leakage current of 12.3nA/cm^2 at 2V.

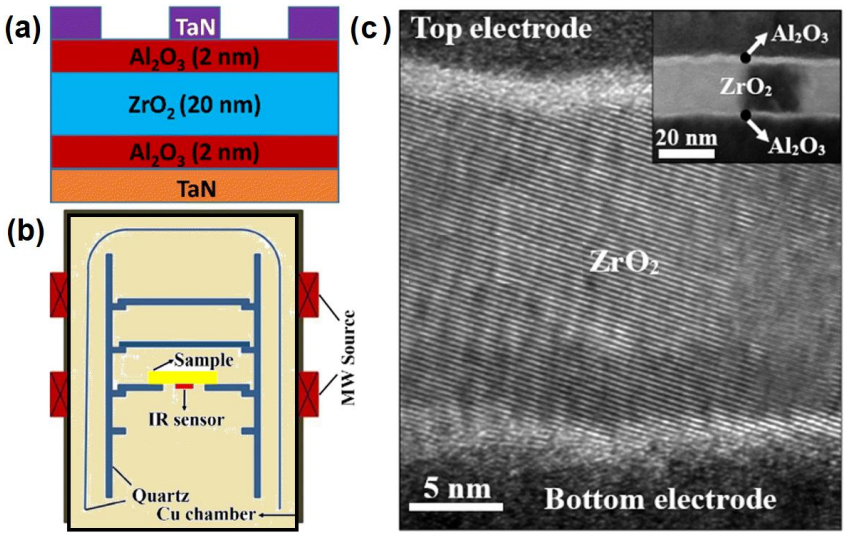

Figure 10. (a) Schematic of a $Al_2O_3/ZrO_2/Al_2O_3$ MIM capacitor, (b) Schematic of the microwave chamber for post-deposition annealing, (c) TEM picture (source [18]**).**

A summary of relevant MIM capacitors is presented in the table 3 [17], detailing the capacitance density C, the leakage current J, insulator thickness IT, fabrication method and anneal temperature. The MIM capacitors based on ZTO/BZTO ($ZrTiO_x/BaZr_yTi_1{-}yO_3$) and $SiO_2/HfO_2/SiO_2$ have capacitance density above 1.2µF/cm^2 and anneal temperature bellow 400ºC. Therefore they are potential technologies for the next generation of MIM capacitors according to the ITRS requirements [4].

Table 3. Comparison of main characteristic of relevant MIM capacitors [17]**.**

Dielectric stack	C (µF/cm^2)	J at 1V (nA/cm^2)	IT (nm)	Deposition method	Anneal temperature (ºC)
HfO_2/SiO_2 [19]	0.6	2	12/4	ALD/PECVD	420
Sm_2O_3/SiO_2 [20]	0.73	18	7.5/4	Sputter/PECVD	420
Er_2O_3/SiO_2 [21]	0.7	4.2	8.8/3.0	Sputter/PEALD	400
$SrTiO_3/Al_2O_3/SrTiO_3$ [22]	1.91	1	25.5/1.0/25.5	ALD	600
$ZrTiO_x/BaZr_yTi_1{-}yO_3$ [23]	1.34	7.5	17/7	E-Beam	400
Al_2O_3/SiO_2 [17]	1.01	6.8	3.7/1.9	PEALD	200
$SiO_2/HfO_2/SiO_2$ [24]	1.24	1	3/4/3	ALD	300
Expected future MIM	1.2	10	-	.	<400

2.1.2. Three-dimensional-MIMs

On the other hand, the high power density and significantly enhanced capacitance density due to new three dimensional MIM structures with large specific area, makes MIMs also attractive as an high energy storage alternative [25] for secondary power supply applications, for instance as ignition devices in uninterrupted power supply systems.

As an example of three-dimensional microstructure that offers an increment in the surface area, J. Mu et al [25] shows an 3D micro-trench MIM capacitor as the fabricated with a Al_2O_3 dielectric thickness of 40nm exhibiting a capacitance density above 3µF/cm^2 in the frequency range from 1kHz to 10kHz and a leakage current density of 0.12µA/cm^2 at 3V and 5.7µA/cm^2 at 17.5V.

A triple MIM capacitor stack formed in trench structures was fabricated using atomic layer deposition (ALD) method to build Al_2O_3 dielectric layers (10nm) and TiN electrodes (20nm) on 3D micro-pore doped silicon, showing a capacitance density of 44µF/cm^2 [26] when three stacked capacitors were connected in parallel. Besides, a breakdown voltage of 7V and a leakage current density of 1µA/cm^2 at 3V was reported. The pore diameter was 1.5µm and the pore-depth was 30µm. Figure 11 shows the schematic of the triple layer stack MIM capacitor.

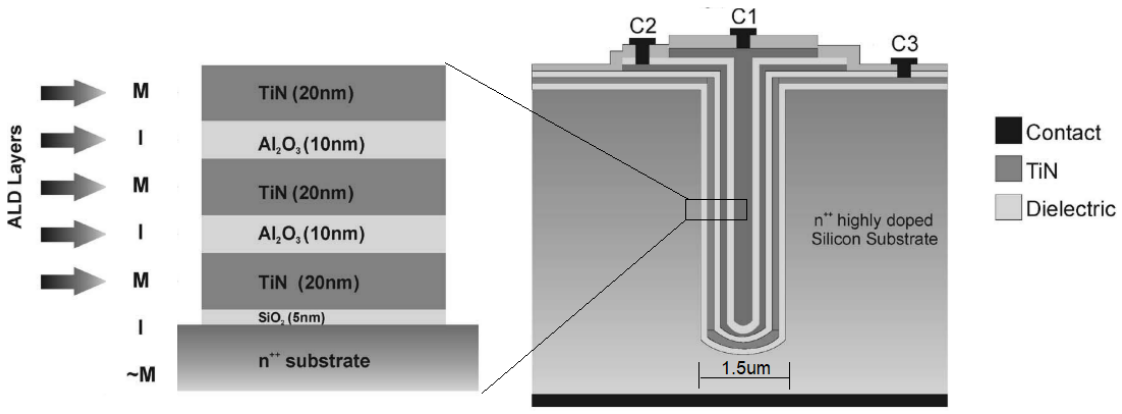

Figure 11. (Left) Diagram of the triple layer stack MIM capacitor, (right) schematic of the triple layer stack MIM capacitor in 3-D doped silicon substrate. Source [26]**.**

Among the other efforts to reach 3D MIM structures with pores, an ALD AlZnO/Al_2O_3/AlZnO (12/10/12 nm) MIM nano-capacitor in anodic aluminum oxide (AAO) template formed in silicon substrate exhibited a capacitance density of 1.53µF/cm^2 [27] at 100kHz. The pore depth obtained in the AAO template was 150nm

and the pore diameter was 80 nm. A part of the pores had a diameter of 20nm, but it did not contribute to the capacitance. A TEM image and schematic of this 3D MIM capacitor is showed in Figure 12.

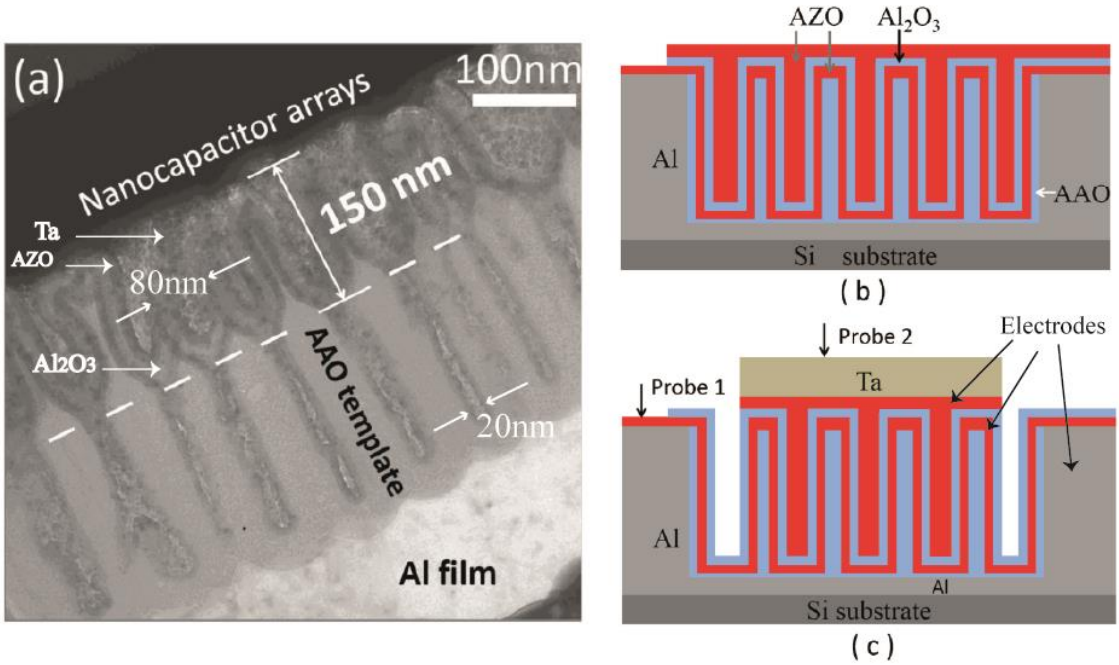

Figure 12. (a) Cross-sectional TEM image of a AlZnO/Al_2O_3/AlZnO MIM capacitor with anodic aluminum oxide (AAO) nanopores, (b) Schematic of atomic layer deposition of the AlZnO/Al_2O_3/AlZnO and (c) final schematic of the 3D AlZnO/Al_2O_3/AlZnO MIM capacitor [27].

MIM capacitors in anodic Al_2O_3 nano-pores have achieved high capacitance densities of up to 3.7μF/cm^2 [28] with pore diameter of 80nm and pore depth of 400nm. Nevertheless, conventional nano-porous anodic aluminum oxide (AAO) templates have the disadvantage of demanding from long fabrication times and the use of toxic or acid reagents [29] for the electrochemical oxidation of aluminum. In an attempt of avoiding anodization techniques, an ALD AlZnO/Al_2O_3/AlZnO MIM capacitors on ZnO nanowires electrodes formed onto silicon substrates is fabricated using hydrothermal synthesis, exhibiting a capacitance density of up to 9.2μF/cm^2 at 1kHz and a low leakage current of 34nA/cm^2 at 2V for 5nm Al_2O_3 dielectric thickness [30], TEM images of this technology are showed in Figure 13.

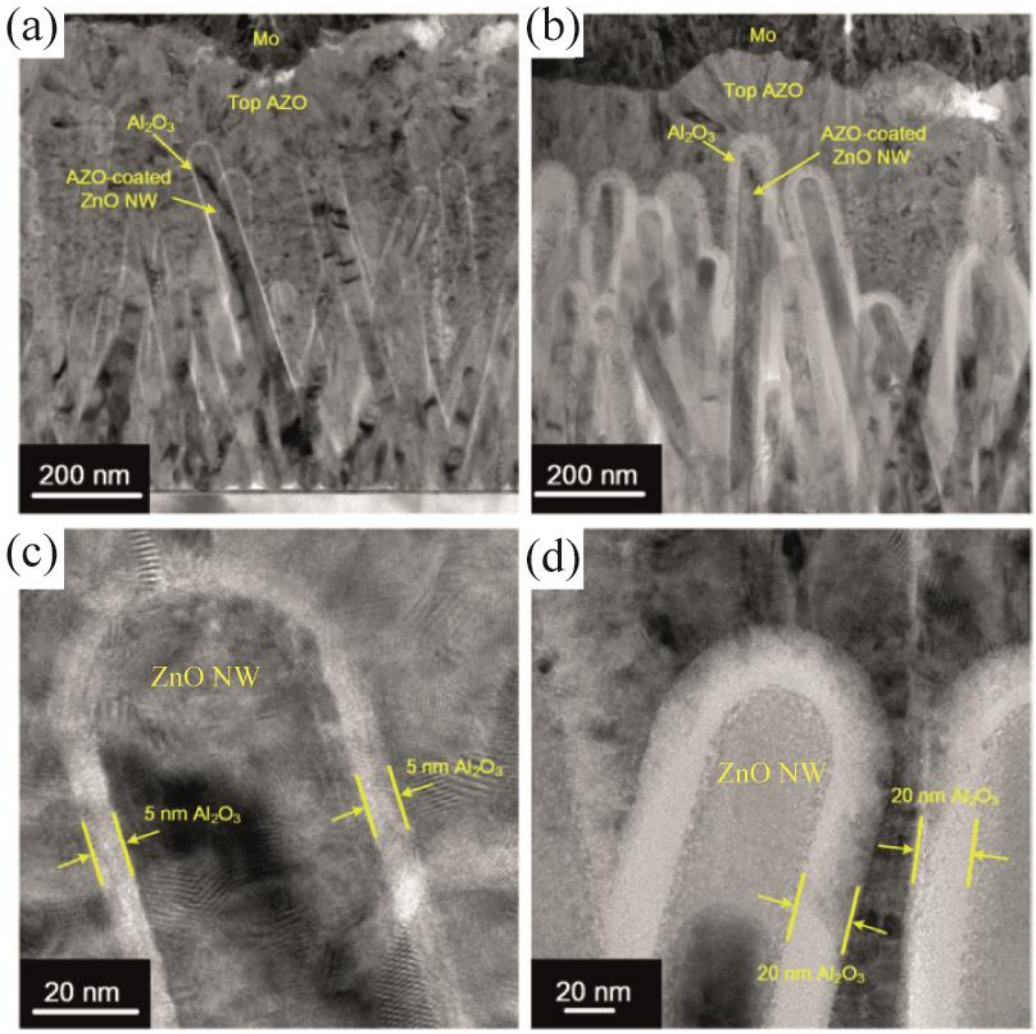

Figure 13. Cross-sectional TEM images of AlZnO/Al_2O_3/AlZnO MIM capacitors based on ZnO nanowires with (a) 5nm and (b) 20nm Al_2O_3 dielectric layers, (c) and (d) magnified cross-sectional TEM images of 3D-MIM capacitor with 5nm and 20nm respectively. Source [30]**.**

Recently, a nanoscale interdigitated electrodes capacitor [31], where the insulator is a nano-porous AAO template between carbon nanotube electrodes, showed a leakage current of about 22.8 nA/cm^2 at 15V and a capacitance density of about 47 µF/cm^2 and 68 µF/cm^2 for 6µm and 10µm thick AAO layer, respectively. The high capacitance is attributed to the large specific area. Whereas, an enhanced breakdown voltage value of 7.5MV/cm (15V) is attributed to the highly uniformity of the pore walls. The pore diameter covers the range of 20 to 23 nm. A schematic of this 3D interdigitated MIM capacitor is observed in Figure 14.

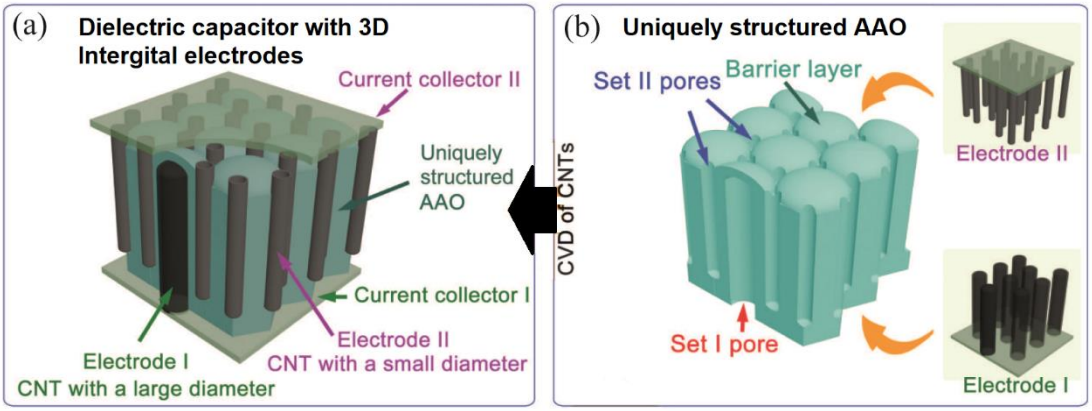

Figure 14. (a) Schematic of a three-dimensional nanoscale interdigitated electrodes capacitor, (b) Interdigital AAO template [31]**.**

Banerjee P. et al [32] reported an improve using a combination of AAO template and ALD deposition, and in turn increasing pore depth. Thus, a nano-tubular MIM capacitor (Figure 15) with 10µm pore depth and 50nm pore diameter in anodic aluminum oxide (AAO) exhibited a capacitance of 100µF/cm^2 at 20Hz.

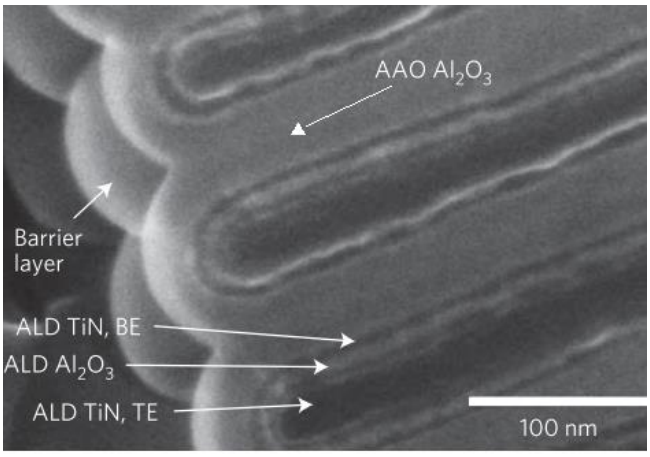

Figure 15. SEM cross-section of the bottom of the nano-tubular MIM. The Al_2O_3 template barrier with the ALD TiN electrodes and the ALD Al2O3 layer is observed (source [32]**).**

Table 4 summarizes the characteristics of the mentioned 3D-MIM capacitor technologies with high capacitance density for high energy storage applications. Anodic aluminum oxide (AAO) templates are mainly used for high energy storage applications because they can be economically scalable. In addition, they show high dielectric constant, high band gap and low density of aluminum oxide as was shown in Table 2.

Table 4. Comparison of different 3D MIM capacitors technologies

3D structure	MIM layers	C $\mu F/cm^2$	J at 2V nA/cm^2	IT nm	Deposition method
Micro-trench [25]	TiN/W/TiN/Al_2O_3/ TiN/W	3	120	10/50/10/40/10/ 50	ALD
Porous AAO template [27]	AlZnO/ Al_2O_3/AlZnO	1.53	-	12/10/12	Anodization of aluminium and ALD
Stand-up ZnO nano-wires [33]	AlZnO/Al_2O_3/AlZnO	9.2	34	10/5/150	Hydrothermal synthesis and ALD
Micro-stacked trench [26]	TiN/ Al_2O_3/ TiN/ Al_2O_3/TiN	44	1000	20/10/20/10/20	ALD
Interdigital and AAO template [31]	Au/CNT/Al_2O_3/ CNT/Au	68	22.8 (at 15V)	-	Anodization of aluminium and pyrolysis of acetylene
Nano-tubular AAO template [32]	TiN/ Al_2O_3/ TiN/	100	-	6.7/7/9.3	Anodization of aluminium and ALD

2.2. Supercapacitors

2.2.1. Supercapacitor concept

Supercapacitors (SCs) are electrochemical devices used as short-term energy store supplies [34] in many applications as electric vehicles, uninterruptible power systems or as voltage stabilizer in wind and photovoltaic systems, among others. Figure 16 shows some system examples where the energy support and the power transfer are required from SCs.

Figure 16. Examples of systems where SCs are found: trams (Barcelona), hydride cars (Toyota) and uninterruptible power supplies.

Table 5 shows a comparison of conventional capacitors, supercapacitors and batteries. SCs have a higher cycle life and power density than the batteries as it can be seen in Table 5. Furthermore, they are fabricated with no-polluting materials that do not produce hazardous waste such as lead or cadmium. These features position them as a good green alternative to the batteries.

The fact that the supercapacitors (up to 10kW/Kg) may storage energy to a higher power density than batteries (up to 1kW/Kg), indicates that SCs are faster transferring energy than batteries, but the supercapacitors are not as faster as conventional capacitors (over 10kW/Kg). Another leading feature of the supercapacitors is that they can handle more energy (1Wh/Kg) than the MIMs or other conventional capacitors (up to 0.1Wh/Kg). However, the energy density is still smaller than batteries (from 10 to 100 Wh/Kg).

Table 5. Comparison of capacitors, supercapacitors and batteries (source [35]**).**

Factor	Conventional capacitors	Supercapacitors	Batteries
Cycle-life	Almost infinite	>500000	About 1000
Power density (kW/Kg)	Greater than 10	Between 0.5 and 10	Less than 1
Energy density (Wh/Kg)	Lower than 0.1	Between 1 and 10	Between 10 and 100
Charge/Discharge Efficiency (%)	Around 100	Between 85 and 98	Between 70 and 85

The charge/discharge efficiency means that virtually all the energy stored in the MIM capacitors can be delivered, whereas supercapacitors have greater losses due to leakages and electrolyte degradation obtaining efficiencies from 85% to 98%.

The supercapacitors industry is in continuous growth. The global supercapacitors market is expected to reach USD 2billons in 2022 according to a study carried out by Zion Market (Figure 17). The increasing demand of the supercapacitors is associated to the use in smart grid applications (wind and solar energy), the pressing demand in the automotive industry (hybrid electric vehicles) and electric transportation systems (trains, subways, buses and elevators), among other applications.

Figure 17. Supercapacitors marked forecast (source [36]**).**

The energy density values achieved by SCs are due to the high capacitance density which is essentially determined by the enhancement of the contact area (high specific surface area) combined with electrolytes that provide electrochemical charges. The energy in the

SCs is mostly electrostatic due to the electrical double layers formed within the electrode-electrolyte interfaces, while in the batteries the stored energy is purely chemical.

The electrical double layers are formed by electrolyte ions that have diffused toward the electrode pores and the electrostatic charges of the electrodes. In Figure 18 shows an example of an SC is constituted by two porous electrodes (anode and cathode) such as activated carbon, soaked in an electrolyte, for instance sulphuric acid. A separator that is usually is fiberglass or a paper or a poly-tetrafluoroethylene (PTFE) membrane prevents electrodes from coming into electrical contact.

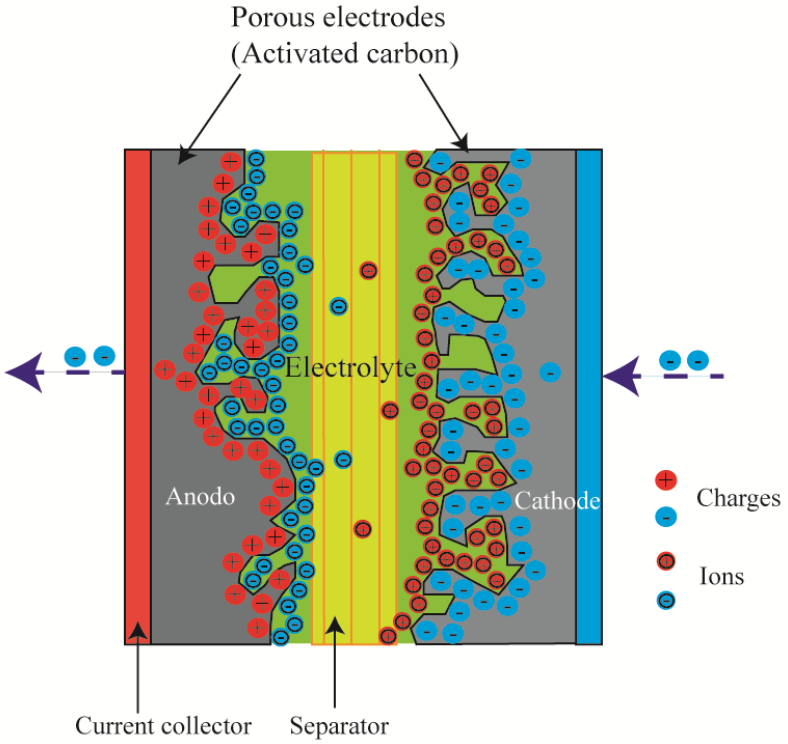

Figure 18. Schematic of a supercapacitor including the anode, cathode, electrolyte and the electrical double layers.

Supercapacitors are classified into three types: Electrical double layer capacitor (EDLC), pseudocapacitor and hybrid capacitor. EDLC are those whose charge accumulation is purely electrostatic and there is no transfer of charge across the electrode-electrolyte interface. The electrodes material of EDLC capacitors is usually based on carbon materials and derivatives.

Another kind of SC with enhanced specific capacitance is the Pseudocapacitor which is based on electrochemical reduction-oxidation (redox) mechanisms yielded in the

interface with conducting polymers or transition metal oxides (RuO_2, TiO_2, MnO_2) as electrodes. Finally, the hybrid capacitor based on the combination of both categories.

The operating voltage, capacitance and equivalent series resistance (ESR) are the main parameters defined for SCs. Table 6 shows typical values for commercial SCs.

Table 6. Some available commercial SCs and characteristics (source: [37]**).**

Manufacturer	Voltage (V)	Capacitance (F)	ESR (mΩ)
APowerCap	2.70	55	-
APowerCap	2.70	450	-
Asashi Glass	2.70	1375	2.50
BatScap	2.70	2680	0.20
Fuji	3.80	1800	1.50
Ioxus	2.70	3000	0.45
Ioxus	2.70	2000	0.54
JSR Micro	3.80	1100	1.15
JSR Micro	3.80	2300	0.77
LS Mtron	2.80	3200	0.25
Maxwell	2.70	2885	0.38
Maxwell	2.70	605	0.90
NessCap	2.70	1800	0.55
NessCap	2.70	3640	0.30
Panasonic	2.30	0.10	0.08
Panasonic	5.50	50	0.08
PowerStor	2.50	2.20	4.57
PowerStor	16.20	65	7.00
Skeleton	3.40	3200	0.47
Skeleton	3.40	850	0.80
VinaTech	2.70	336	3.50
VinaTech	3.00	342	6.60
Yunasko	2.70	510	0.90
Yunasko	2.75	1275	0.11
Yunasko	2.70	7200	1.40

The operating voltage, also known as window voltage, depends on the stability of the electrolyte (decomposition voltage of the electrolyte). Three type of electrolytes are used in SCs: aqueous such as sulfuric acid (H_2SO_4) or potassium hydroxide (KOH) [38], organic such as propylene carbonate (PC) or acetonitrile (AN) with tetraethyl-ammonium tetra-fluoroborate salt (TEABF4) [39], and ionic liquids in recent research [40]. Using activated carbon electrodes, the cell working voltage ranges from 2.3V to 2.7V for organic electrolytes, 0.8-1.0V for aqueous electrolytes and 3-4V for ionic liquid electrolytes [38].

As mentioned before, the main defining parameter of a SC is the capacitance, but there is a more specific parameter, that is the specific capacitance, that takes into account the charge storage ability of the supercapacitor active material, defined as:

$$C_S = \frac{dQ}{dV\forall} \quad \textbf{(19)}$$

Where ∀ may define the mass, the volume, or the surface area of the electrodes or the active material.

If ∀ is the mass, C_S is termed as gravimetric capacitance (F/g), also denoted as C_W.

If ∀ is the volume, C_S is termed as volumetric capacitance (F/cm^3), also denoted as C_V.

If ∀ is the electrochemical surface area (real area), C_S is termed as area-specific, normalized, differential, intrinsic, interfacial or double layer capacitance (μF/ cm^2), also denoted as C_D.

If ∀ is the geometric area, C_S is termed as areal capacitance (F/cm^2).

The specific surface area (SSA) is the total surface area of the microspores electrode measured using the standard technique known as Brunauer–Emmett–Teller (BET) method [41] which is based on the phenomenon of adsorption of a gas (Nitrogen at 77K) into a solid, the units are m^2/g [42]. The specific surface area is useful to estimate the double layer capacitance. For instance, if the C_W = 11mF/cm^2 and the SSA_{BET} =2371m^2/g, then the double layer capacitance is 9.9 μF/ cm^2 [43].

2.2.2. Supercapacitors classification.

As mention before, the supercapacitors area may be classified according to the conductive electrode material. The electrode material is often referred to as the **active material**. While the electrolyte, the binder and the current collector are called **inactive materials**. Figure 19 shows a classification of the supercapacitors regarding the active material used in each one.

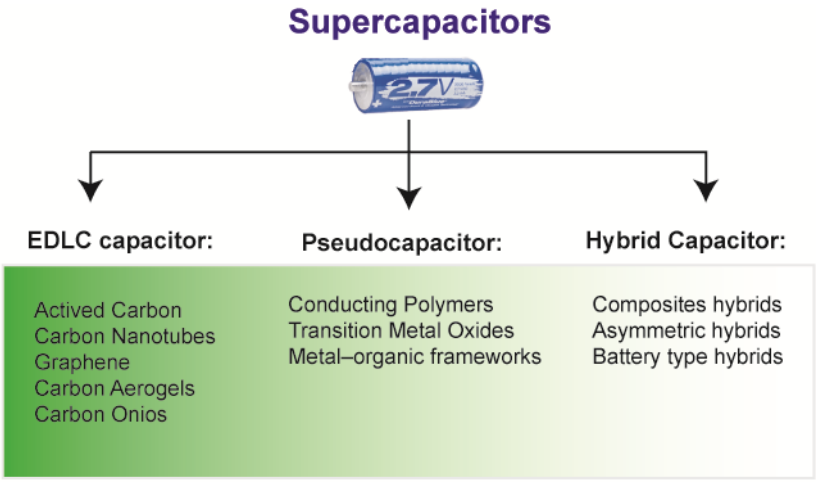

Figure 19. Classification of supercapacitors: The Electrical Double Layer, Pseudo and Hybrid Capacitors.

Figure 20 summarizes some active materials used in SCs and their specific capacitances [44]. Carbon based material are widely studied but do not top the list of materials that provide greater specific capacitance.

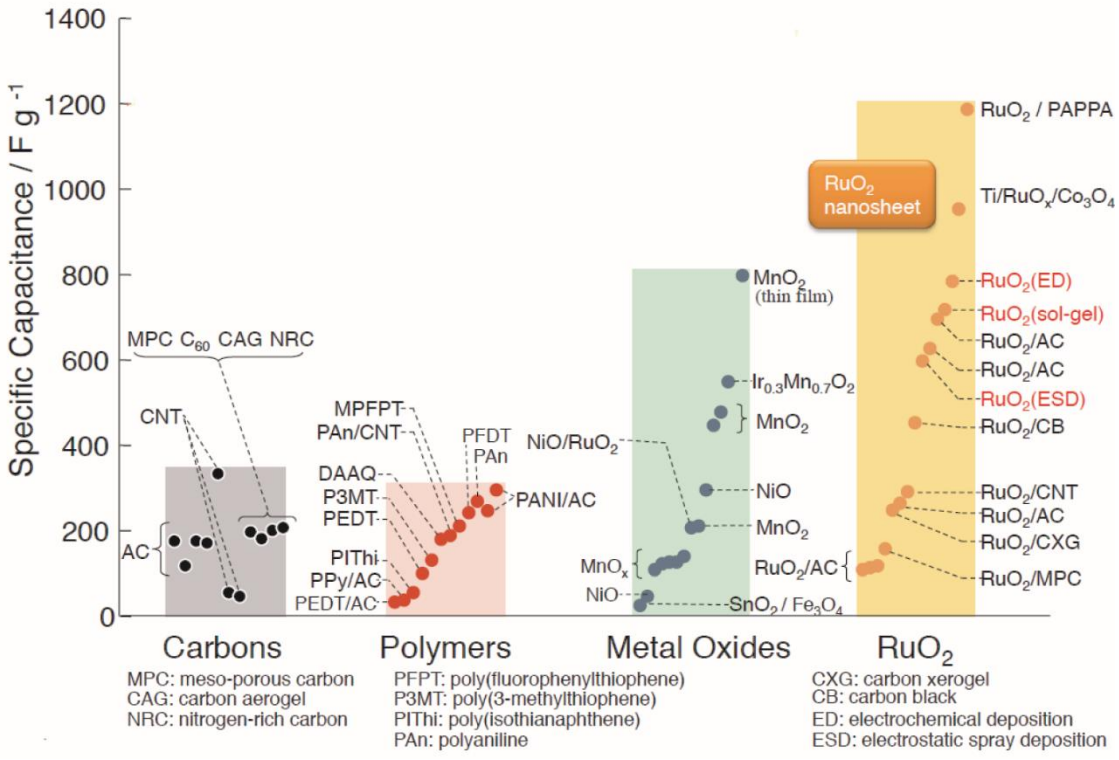

Figure 20. Specific capacitance of active materials in supercapacitors (source [44]**).**

Composites of redox-active materials as ruthenium oxide (RuO_2) exhibit higher capacitances than carbon-based and conducting polymer materials. However, despite this potential, the success of RuO_2 has been inadequate by its excessive cost and toxicity. As it can be seen, there are many technology approaches on the fabrication of SCs. Therefore, SCs have an extensive range of possibilities that require a very specific study for each material. This thesis is focused on capacitors which may be half way between MIMs and EDLCs supercapacitors, for this reason, this section is mainly showing characteristics of EDLCs and not of pseudo-capacitors or hybrids.

2.2.3. Advances in Electrical Double Layer capacitors

Activated carbon is the material mostly used as active material in the SC industry. It is usually a powder transformed into a solid electrode with a high specific surface area of **1000-3000m^2/g** [45] [46] [43], including a binder such as polytetra-fluoroethylene (PTFE), poly-methylcellulose, polystyrenestyrene/butadiene copolymer or ethylene/acrylic acid copolymer [47]. The raw material (precursor) of the activated carbon can be coal, coconut, shells, peat, wood and petroleum based residues, that is, materials with a high carbon content which are processed by thermal activation (900ºC) with oxidizing gases (such as CO_2, H_2O or O_2) or chemical activation (such as KOH). Figure 21 sums up the preparation process of activated carbon.

Electrodes based on activated carbon have specific capacitances between **100-300F/g** or a double layer capacitances of **15-50µF/cm^2** depending on the electrolyte [38] [46] or the activation method [43]. With organic electrolytes, the specific capacitance is about of **100F/g** or **70F/cm^3** [48].

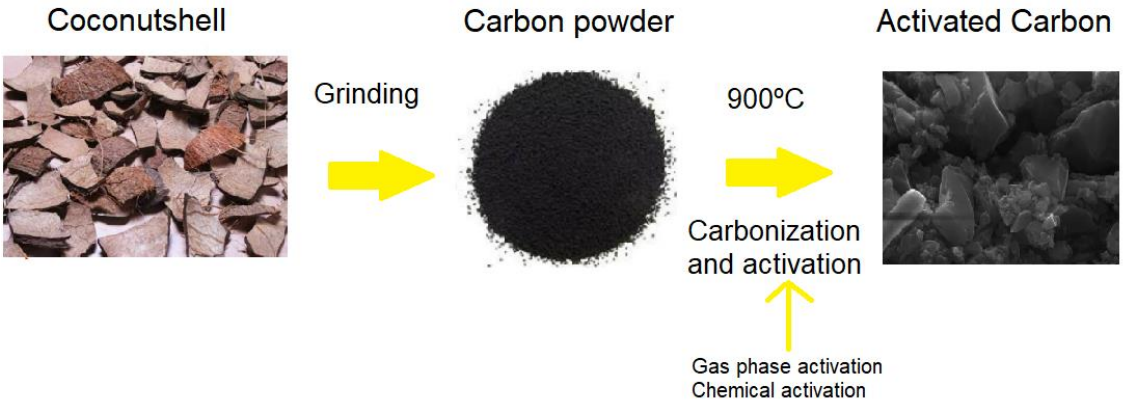

Figure 21. Diagram of the fabrication process of activated carbon.

The density of an activated carbon is in the range of **0.4-0.8g/cm^3**, the thickness is usually in the range of **100-300µm**, then the capacitance of an electrode of a thickness (t), area (A) and density (ρ) can be calculated as [38]:

$$C = (F/g)\rho tA \quad \textbf{(20)}$$

Activated carbon is composed by structures with size pores [43] in the range of micropores (<2nm), mesopores (2-50nm), and macropores (>50nm). The pore diameters are classified by International Union of Pure and Applied Chemistry (IUPACH) [49]. The structures with micropores are the most used [38] mainly in supercapacitors with aqueous electrolytes like KOH. They are, however, not so effective for organic electrolyte because organic ions are bigger than those pores [45].

Experimentally, capacitance does not always have a lineal relation with the surface area of an active carbon, first, due to that all pores may not be accessible to the electrolyte ions; and second, because the double layer varies with various types of activated carbons (different precursors and activation methods).

Figure 22 shows the SEM images of two carbon electrode samples. The first (left) electrode sample, it is fabricated by a mixture of 92% activated carbon, 5% acetylene black and 3% PTFE that shows carbon grains with a size up to 10 µm, whereas PTFE and acetylene black particles (binder) are in the order of 0.1 µm. The second electrode (right) has grains with sizes ranging around 1µm and 0.1µm, it is a carbon electrode extracted from a commercial SC cell package. It should be noted that PTFE is the binder used to hold activated carbon grains together and carbon black is an additive to raise the electrode conductivity.

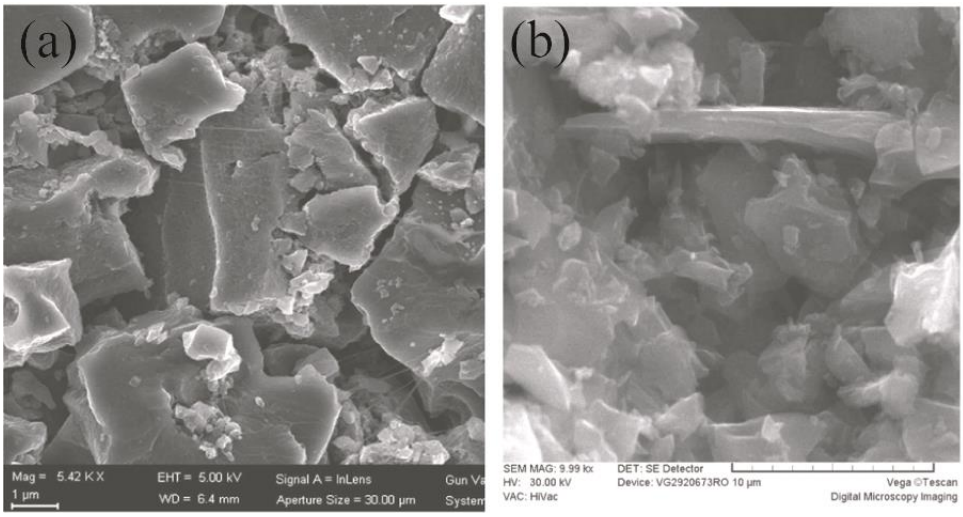

Figure 22. SEM images of activated carbon electrodes extracted (a) from a specific fabricated electrodes and (b) a commercial one (source [50]**).**

Inverse opal carbon templates [51] using silica colloidal crystal as a opal template and a polymer as carbon precursor have been tested as electrode material for EDLC capacitors. An inverse opal carbon structure using poly-furfuryl alcohol as a precursor in an organic electrolyte, showed a specific capacitance up to 100F/g and a specific surface area from 600 to 1200m^2/g. The fabrication process can be seen in Figure 23. The silica nanoparticles crystal was sintered at 1100ºC. Afterwards, poly-furfuryl alcohol was poured over the silica opal template. Then, it was carbonated at 1000ºC producing a carbon/silica composite. Finally, the silica nanoparticles were etched off with a hydrofluoric acid solution, resulting a cavernous carbon template.

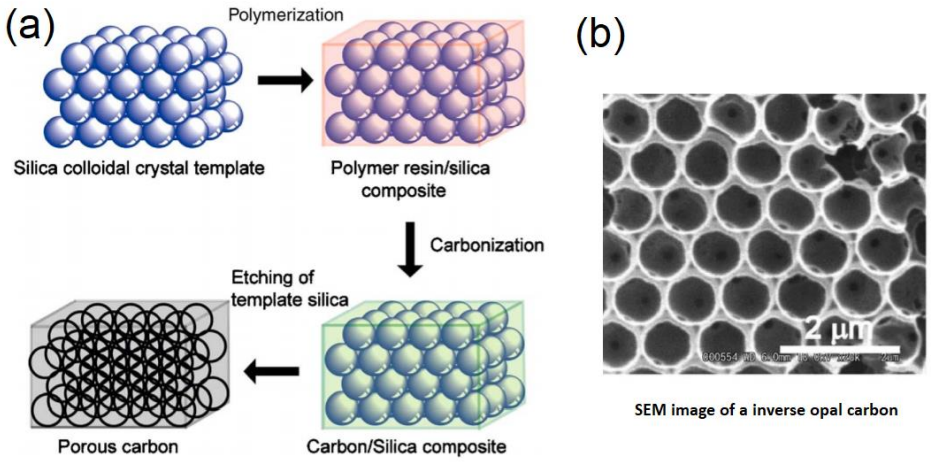

Figure 23. Inverse opal carbon template: (a) Fabrication steps (b) SEM image (source [51]**).**

Carbide derived carbons (CDCs) [52] are carbons derived from metal carbides compounds such as TiC, SiC, Mo_2C, B_4C, by selective chlorine (Cl_2) etching of metals. Electrodes based on CDCs provide uniform distribution of pores and high specific area from 1000 to 2000 m^2/g [53]. A specific capacitance ranging from 100F/g to 130F/g [52] was obtained for CDC SC electrodes using micro-sized titanium carbide (TiC) particles as precursor in organic electrolytes. Figure 24 shows a SEM image of carbon powder synthetized from TiC particles. The fabrication of templated CDC have given good results, as an example, a mesoporous SiC derived carbon (CDC) [54] showed a specific capacitance up to 170F/g using tetraethylammonium tetrafluoroborate ($TEABF_4$) solution in acetonitrile, and a specific surface area up to 2430 m^2/g.

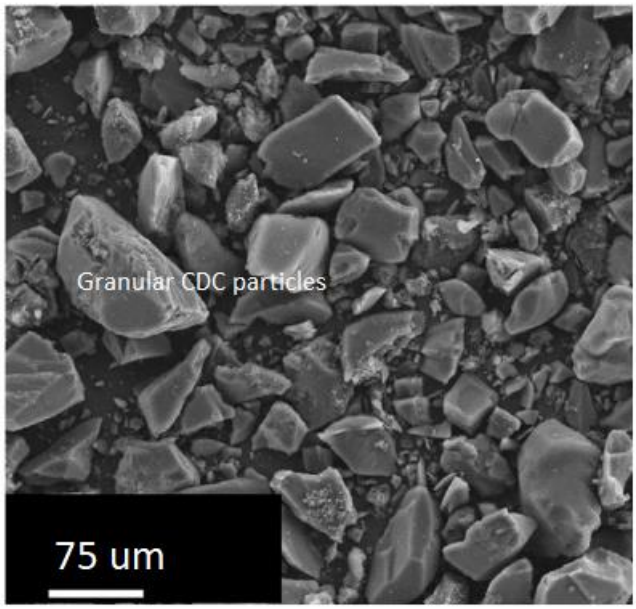

Figure 24. A SEM image of the surface of carbide derived carbon synthetized from TiC. (source [52]**).**

Carbon nanotubes (CNTs) are large molecules consisting of carbon atoms rolled in a cylinder shape [55] with diameters in the nanometre range and lengths from micrometres to centimetres. CNTs are nano-materials widely researched as SC active material because of their high surface area, electrical conductivity, corrosion resistance and temperature stability. There are two CNT types: single-walled carbon nanotube (SWNT) or multiple-walled carbon nanotube (MWNT). A SWNT consist of a cylindrical wall of single-layer carbon atoms (graphene). Whereas a MWNT are several concentric nanotubes inside other nanotubes with diameter between 3 to 30nm [56].

The CNT structures usually achieve better performance than activated-carbon mainly because their micro and meso-pores distribution give them better electrolyte accessibility [57] than activated carbon structures to reach high capacitances. Moreover, CNTs are electrically more conductive (5000Scm^{-1}) [58] than activated carbon (0.5-2Scm^{-1}) [59] which produces a higher energy transfer than in activated carbon.

The CNTs can be synthetized by different methods such as arc-discharge method, laser-ablation method, catalytic decomposition of hydrocarbons, pyrolysis of hydrocarbons, plastic and chemical vapour deposition CVD processes. However, no method is still viable for large scale commercial production due to the high manufacturing cost [60].

Figure 25 shows the SEM image of a randomly entangled SWNTs electrode [61] in a KOH electrolyte that achieved a maximum specific capacitance of 180F/g. The nanotubes were synthetized using the arc-discharge method with a heat treatment temperature at 1000ºC. A binder was used for the adhesion of the nanotubes between them.

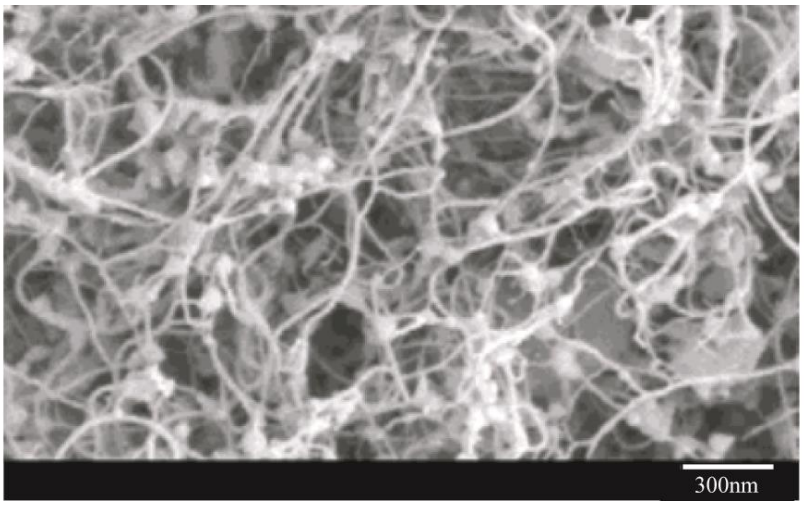

Figure 25. SEM images of randomly entangled and cross-linked SWNT (source [61]**).**

Figure 26 shows a TEM image of commercial catalytically grown MWNTs that were functionalized with nitric acid to introduce oxygenate groups. The MWNTs cell using a H_2SO_4 electrolyte exhibited a specific capacitance of up to 102F/g [62]. A benefit of functionalization is that it contributes to a good self-adhesion of the MWNTs.

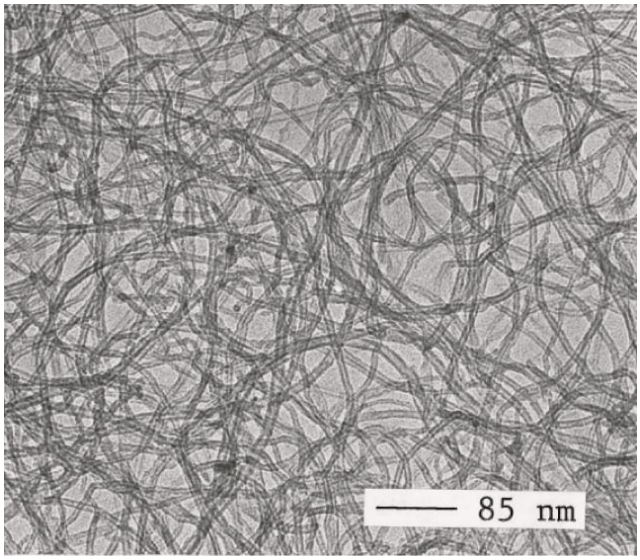

Figure 26. TEM image of randomly entangled and cross-liked MWNTs with an average diameter of 8nm (source:[62]**).**

The porosity of the CNTs can be improved by chemical KOH activation in order to enhance the specific surface area (structures with 470m^2/g improved their surface to weight value up to 1470-3802 m^2/g after activation) [63], and to obtain enhanced capacitance density values of MWNT supercapacitors [64] (from 15F/g to 90F/g after activation). Besides, the capacitance may be enhanced with thermal annealing processes oxidizing of CNTs till a specific temperature [55], since the capacitance can also decrease due to the reduction of the surface area. For instance Li et al [65] annealed entangled MWCNT at different temperatures finding that the specific capacitance increased from 23F/g to 48F/g with at a temperature treatment of 650ºC, but the specific capacitance dropped for higher heating temperature values. In the literature, a BET specific surface area has been reported of up to 1600 m^2/g for SWNT and around 400 m^2/g for MWNT have been reported [57].

The CNTs can be arranged in aligned or non-aligned forms. Aligned CNTs are more desirable because they have shown to provide more surface access to the electrolyte. A vertical aligned CNT electrode [66] showed a capacitance density of 440 F/g using 1-ethyl-3-methylimidazolium tetrafluoroborate ($EMIBF_4$) as ionic liquid electrolyte. Aligned carbon nanotubes can be produced by plasma-enhanced chemical vapour deposition (PECVD) [67] [68] on thin film of iron or nickel, while chemical vapour deposition (CVD) can produce non-aligned CNTs as it observed in Figure 27. Carbon arc-discharge, pyrolysis of hydrocarbons and pulsed laser vaporization [58] are different

processed to synthetize non-aligned CNTs, that also have applications in other industries [69] [70].

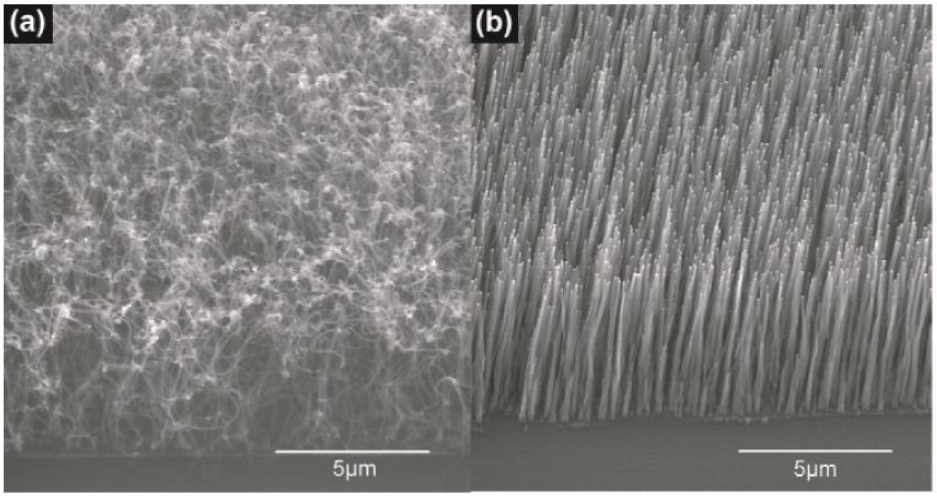

Figure 27. SEM pictures of different CNT arrangements: (a) curly and non-aligned CNTs using thermal CVD, (b) vertical aligned CNTs using PECVD (source [67]**).**

Vertical aligned single-walled carbon nanotubes (SWNT) [71] have also been also grown with water-assisted chemical vapor deposition synthesis reaching heights of up to 2.5mm in a 10 minute growth time with a high carbon purity of 99.98%. Figure 28 shows images of a very dense SWCNT forest synthesized with this mentioned method.

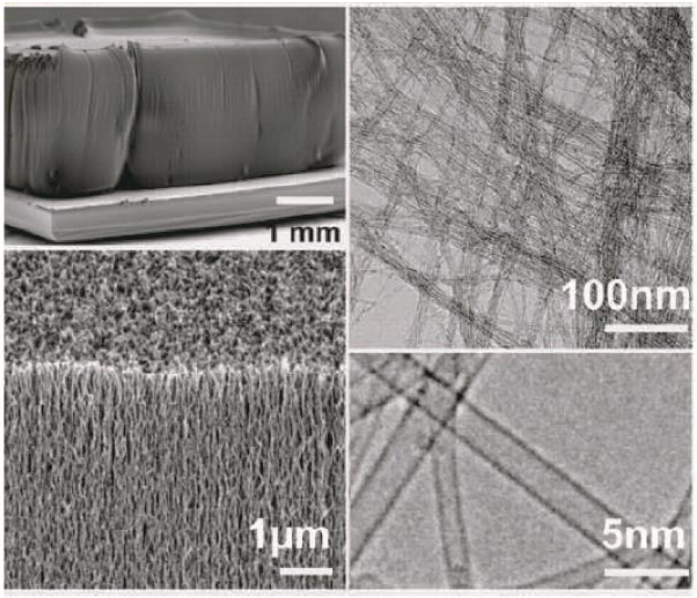

Figure 28. SWNT forest synthesized with water assisted CVD (source [71]**).**

As an example of a hybrid SC, Polyaniline (PANI), a conducting polymer, added in the CNTs contributed to an increase in the specific pseudo-capacitance as it has been reported

in a structure of a SC based on Vertical Aligned Carbon Nanotubes and PANI nanocomposite electrodes [72]. The device showed a specific capacitance of 403.3 F/g in $HClO_4$ electrolyte and 314.6 F/g in $EMIBF_4$ electrolyte; the schematic of the designed structure of the SC electrode is observed in Figure 29, disordered entangle CNTs are vertical aligned and PANI is polymerized on the VA-CNTs.

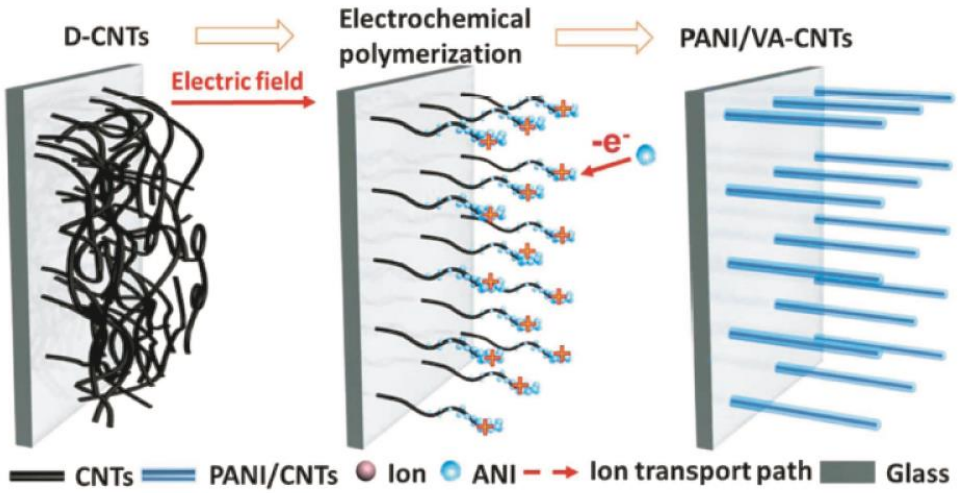

Figure 29. Schematic illustration of the fabrication of the PANI/VA-CNTs electrodes (source [72] **).**

On the other hand, **graphene** is a single graphite atom layer which has a much higher conductivity (10^6 Scm^{-1}) than CNTs ($5x10^3 Scm^{-1}$) [58] and a very high specific surface area of 2630 m^2/g [58]. Graphene was first synthesized by Geim and Novoselov in 2004 [73] from a commercial pyrolytic graphite sheet [74], previously etched in oxygen plasma. The graphite was stuck, pressed and detached from a scotch tape, leaving thin graphite flakes that were put on a silicon wafer. Then, it was discovered that the thin graphite flakes contented few layer of graphene. Nowadays, there are different synthesize methods including: mechanical exfoliation of graphite in solutions [75] [76] , thermal chemical vapor deposition (CVD), plasma enhanced CVD [74] and synthesis of graphene oxide and the reduction [77]. The control of these processes and the fact that graphene has a theoretical maximum specific capacitance of 550F/g [78], are opening novel opportunities to the large scale fabrication of graphene-based SCs.

Figure 30a shows the structure of a flexible SC [79] using two graphene electrodes and poly vinyl alcohol/phosphoric acid (PVA/H_3PO_4) gel electrolyte and polyethylene-terephthalate (PET) as substrate, showing a capacitance of 12.4μF/cm^2. The graphene was

fabricated by means of a rapid thermal annealing (RTA) process of Ni/carbon/SiO_2/Si substrate and it was then transferred to the PET substrate.

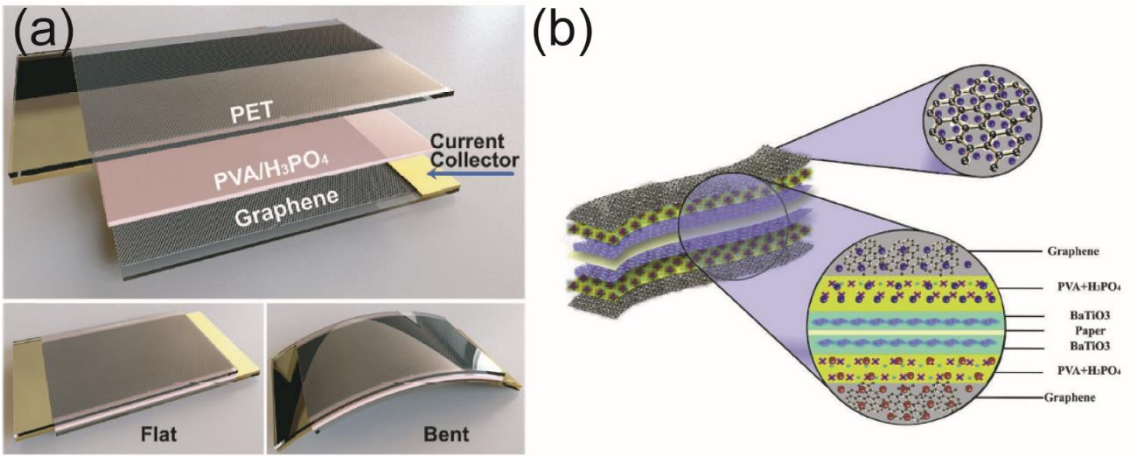

Figure 30. Images of a (a) flexible graphene supercapacitor (source [79]**) on PET substrate. Schematic of another (b) flexible graphene supercapacitor (source** [80]**) on paper substrate.**

L. Fekri et al [80] reported another flexible SC example, consisting of both sides paper substrates using graphene as electrode material, PVA/H_3PO_4 as gel electrolyte and $BaTiO_3$ as gel separator. The resulting specific capacitance ranges in this case from 87F/g to 410F/g. The schematic of symmetric SC is showed in Figure 30b. In these examples, PVA/H_3PO_4 makes up a known solid polymer electrolyte (SPE), where H_3PO_4 works as an ionic liquid and PVA as a polymeric matrix. A SPE has the ability to be flexible, transparent, lightweight and stable with temperature.

Graphene oxide (GO) is an insulator material, but reduced graphene oxide (RG-O) platelets yielded after a heating treatment of oxide graphene suspensions, gained electrical conductivity (5230 S/m) due to the removal of oxygen groups. So, Yanwu Zhu et al [81] reported a specific capacitance of about 120F/g for two SCs fabricated with RG-O platelets as electrodes with an electrolyte of propylene carbonate (PC) with $TEABF_4$. Figure 31 shows the SEM image of wrinkled platelets of RG-O obtained by exfoliation of graphene oxide suspension in PC at 150ºC followed by vacuum drying.

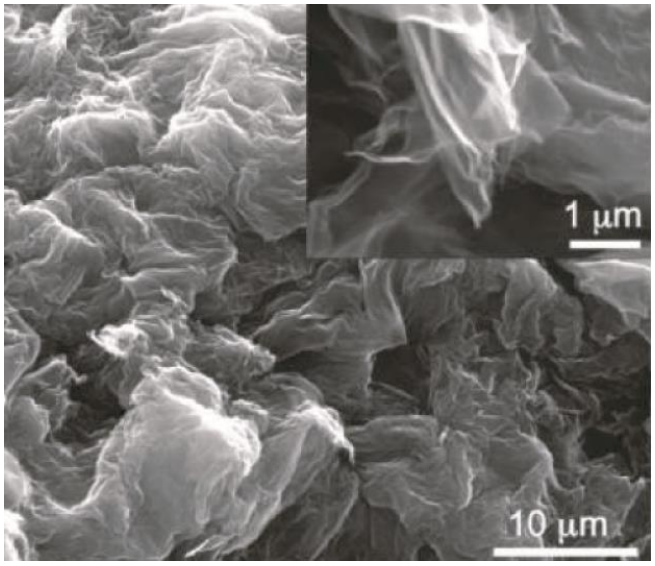

Figure 31. SEM image of RG-O platelets obtained by heating graphene oxide in PC (source [81] **).**

Without using a binder, porous graphene electrodes were fabricated by the electrospray of graphene oxide (GO) nanoparticles on stainless steel substrates. Crumpled reduce graphene oxide (C-RGO) structures were obtained after a hydrazine-thermal reduction treatment process. The SC cell exhibited a specific capacitance 366F/g [82] using KOH as aqueous electrolyte. Figure 32 shows a schematic of the fabrication process. This work made electrospray to attract attention as a method of depositing graphene. A. Varea et al [83] analyzed the electrospray deposition condition to deposit GO and RGO onto rigid and flexible substrates from GO and RGO nanoparticles dispersed in isopropanol using electrospray technique under ambient conditions.

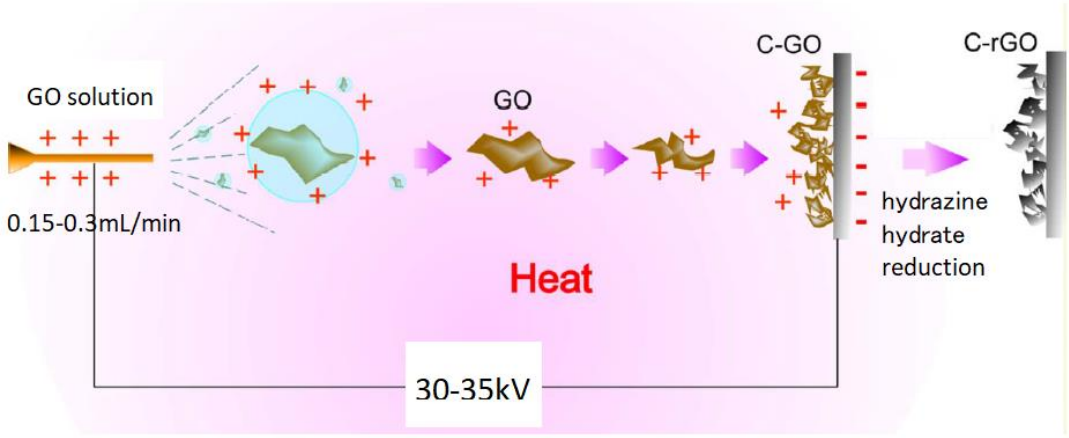

Figure 32. Schematic of the fabrication process of C-RGO from GO solution using electrospray technique. C-GO is reduced in the hydrazine hydrate vapour at 85 °C, source [82]**.**

Recently, J. Yan et al [84] fabricated a graphene SC using the electrospray technique with a moving stage. The GO solution was electrosprayed at 8kV on polyamide nanofiber film/aluminium foil, then a post-treatment was performed with a GO film as it can be seen in Figure 33. Summarizing, the electrosprayed GO film was separated from the foil in order to obtain a reduced GO by means of the immersion of GO into a hydro-iodic (HI) acid solution at 100 ºC. The specific capacitance in KOH electrolyte was 174 F/g.

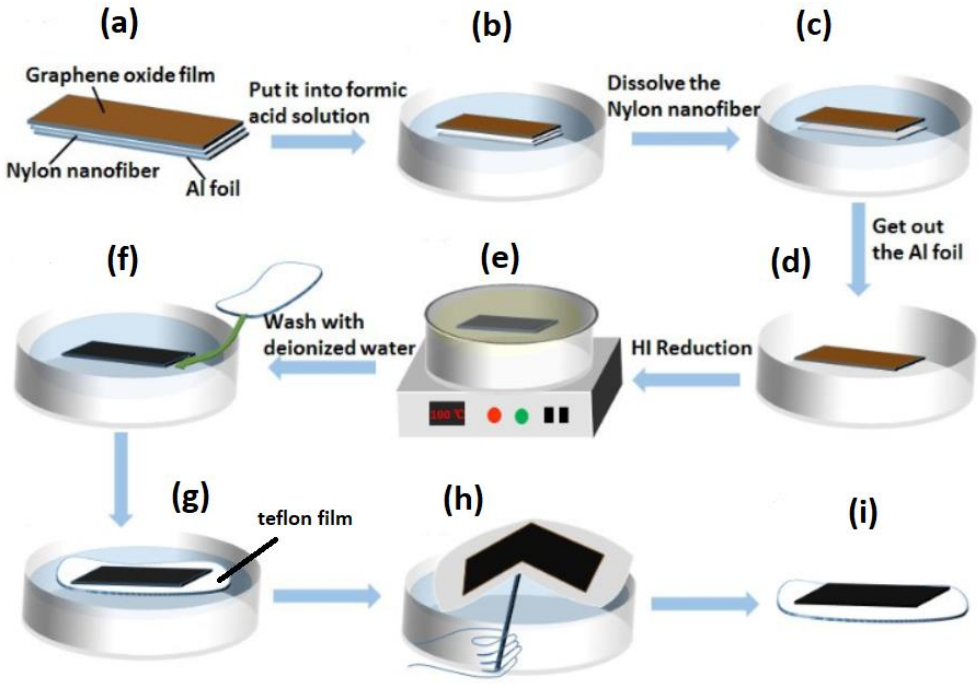

Figure 33. Schematic of the fabrication of a RGO electrode. (source [84]**).**

Table 7 sums up several mentioned electrode materials used in EDL supercapacitors, it is included the electrolyte, the specific capacitance, the electrode cost and electrode conductivity are included. The capacitance of the different active materials varies with the type of electrolyte used, but carbon nanotubes and graphene electrodes using ion liquid electrolytes show higher capacitances and higher conductivities, thus both materials are the best in terms of performance. However, physicochemical modification of activated carbon continues improving the performance of SC electrodes with capacities as high as 450F/g [85]. For that reason and added to the fact that they are more economical than CNT or graphene electrodes, activated carbon is still the active material that dominates currently full-scale manufacture of SC. In terms of costs, graphene could be competing a candidate as long as it reduces their costs. Graphene electrodes have moderate costs at the present time. All of these factors should be considered to improve the existing technologies.

Finally, the gravimetric capacitance is an important parameter in the electrochemical field, because they characterize the capacitance over the electrode mass more than capacitance over the area. Therefore, the areal capacitance and double layer capacitance (defined in the section 2.2.1.) are rarely itemized. In order to present a broader catalog of parameters, Table 8 sums up these specific capacitances found in the literature.

Table 7. Comparison of different carbon based electrode materials used in EDLCs.

Electrode	**Electrolyte**	**Cs (F/g)** [86]	**Cost** [87]	**Conductivity** [87]
Activated carbon [38] [43] [85]	Aqueous: KOH or H_2SO_4	100-450	Low	Low
Activated carbon [88] [39]	Organic: $(C_2H_5)_4NBF_4$ with acetonitrile or acetonitrile with tetraethylammoniumtetrafluoroborate (Et_4NBF_4)	~100	Low	Low
Inverse opal carbon [89] [90]	Aqueous: KOH	130-220	High	Low
Inverse opal carbon [51]	Organic: Tetraethylammonium tetrafluoroborate (Et_4NBF_4) in acetonitrile	~100	High	Low
Carbide derived carbon [52]	Organic: Tetraethylammonium tetrafluoroborate (Et_4NBF_4) in acetonitrile (CH_3CN)	100-130	Moderate	Moderate
Carbide derived carbon [86] [52]	Ionic liquids: 1-Ethyl-3-methylimidazolium bistrifluoromethylsulfonylimide (EMIM TFSI) in acetonitrile (CH_3CN)	100-150	Moderate	Moderate
Carbon nanotubes [86]	Aqueous: NaOH or KOH	20 - 180	High	High
Carbon nanotubes [66]	Ionic liquid: 1-ethyl-3-methylimidazolium tetrafluoroborate $EMIBF_4$	~440	High	High
Reduced Graphene oxide (rGO) [86]	Organic:Tetraethylammonium tetrafluoroborate (Et_4NBF_4)	10 - 150	Moderate	high
Graphene oxide [91]	Aqueous: KOH	~190	Moderate	high
(Curved) Graphene [92]	Ionic liquid: $EMIMBF_4$.	100-250	Moderate	high
Graphene [80]	Ionic liquid: PVA/H_3PO_4	87 - 410	Moderate	high

Table 8. Areal capacitance and double layer capacitance of carbon materials

Electrode material	**Areal capacitance (mF/cm^2)**	**Double layer capacitance ($\mu F/cm^2$)**
Activated carbon	10-50 [46]	5-50 [58] [93] [46]

Nanotube	8 [94] - 16 [42]	6-24 [35]
Graphene	~ 40 (rGO-gel) [78] in KOH	~21 [74] [95] in a ionic liquid (BMIM- PF6). 2-9 [93] in KOH

2.3. References

[1] J.-. Arnould, P. Benech, S. Cremer, J. Torres, and A. Farcy, “RF MIM capacitors using Si/sub 3/N/sub 4/ dielectric in standard industrial BiCMOS technology,” in *2004 IEEE International Symposium on Industrial Electronics*, 2004, vol. 1, pp. 27–30 vol. 1.

[2] “CUSTOM SYSTEM-ON-CHIP (SOC),” *Arm Limited*, 2019. [Online]. Available: https://www.arm.com/why-arm/custom-socs. [Accessed: 15-Sep-2019].

[3] S. Van Huylenbroeck, S. Decoutere, R. Venegas, S. Jenei, and G. Winderickx, “Investigation of PECVD dielectrics for nondispersive metal-insulator-metal capacitors,” *IEEE Electron Device Lett.*, vol. 23, no. 4, pp. 191–193, 2002.

[4] B. J. Hutchinson, “An Investigation of High- k Materials in Metal-Insulator-Metal Capacitor Structures,” NATIONAL UNIVERSITY OF IRELAND, CORK, 2017.

[5] “The International Technology Roadmap for Semiconductors (ITRS). Table RFAMS4 On-Chip Passives Technology Requirements,” 2012. [Online]. Available: http://www.itrs2.net/2012-itrs.html. [Accessed: 18-Oct-2019].

[6] M. A. Zulkifeli, S. N. Sabki, S. Taking, N. A. Azmi, and S. S. Jamuar, “The effect of different dielectric materials in designing high performance Metal-Insulator-Metal (MIM) capacitors,” *Int. J. Electr. Comput. Eng.*, vol. 7, no. 3, pp. 1554–1561, 2017.

[7] S. B. Chen, C. H. Lai, A. Chin, J. C. Hsieh, J. Liu, and A. L. F. Characteristics, “High-Density MIM Capacitors Using High-K Al2O3 and AlTiOx Dielectrics,” *Electronics*, vol. 23, no. 4, pp. 201–204, 2002.

[8] M. M. Krasnov, S. E. Avetisov, N. V. Makashova, and V. R. Mamikonian, “A High Performance MIM Capacitor Using HfO2 Dielectrics,” *IEEE ELECTRON DEVICE Lett.*, vol. 23, no. 6, pp. 27–30, 2002.

[9] M. Y. Yang, D. S. Yu, and A. Chin, “High-Density RF MIM Capacitors Using

High-k La2O3 Dielectrics," *J. Electrochem. Soc.*, vol. 151, no. 7, p. F162, 2004.

[10] B. Hudec *et al.*, "Electrical properties of TiO2-based MIM capacitors deposited by TiCl4 and TTIP based atomic layer deposition processes," *Microelectron. Eng.*, vol. 88, no. 7, pp. 1514–1516, 2011.

[11] D. Kannadassan, R. Karthik, M. Shojaei Baghini, and P. S. Mallick, "Nanostructured metal-insulator-metal capacitor with anodic titania," *Mater. Sci. Semicond. Process.*, vol. 16, no. 2, pp. 274–281, 2013.

[12] J. Robertson, "High dielectric constant oxides," *Eur. Physcial J. Appl. Phys.*, vol. 28, pp. 265–201, 2004.

[13] S. A. Sherrill, P. Banerjee, G. W. Rubloff, and S. B. Lee, "High to ultra-high power electrical energy storage," *Phys. Chem. Chem. Phys.*, vol. 13, no. 46, pp. 20714–20723, 2011.

[14] S. U. Park *et al.*, "Analysis of reliability characteristics of high capacitance density MIM capacitors with SiO2-HfO2-SiO2 dielectrics," *Microelectron. Eng.*, vol. 88, no. 12, pp. 3389–3392, 2011.

[15] C.-S. Ho, S.-J. Chang, S.-C. Chen, J. J. Liou, and H. Li, "A Reliable Si3N4/Al2O3-HfO2 Stack MIM Capacitor for High-Voltage Analog Applications," *Electron Devices, IEEE Trans.*, vol. 61, no. 8, pp. 2944–2949, 2014.

[16] K. Lee *et al.*, "Leakage current suppression in spatially controlled Si-doped ZrO2 for capacitors using atomic layer deposition," *Thin Solid Films*, vol. 657, no. October 2017, pp. 1–7, 2018.

[17] D. Z. Austin, D. Allman, D. Price, S. Hose, and J. F. Conley, "Plasma Enhanced Atomic Layer Deposition of Al2O3 /SiO2 MIM Capacitors," *Ieee Electron Device Lett.*, vol. 36, no. 5, pp. 496–498, 2015.

[18] B. Zhu, X. Wu, W. J. Liu, S. J. Ding, D. W. Zhang, and Z. Fan, "Dielectric Enhancement of Atomic Layer-Deposited Al2O3 /ZrO2 /Al2O3 MIM Capacitors by Microwave Annealing," *Nanoscale Res. Lett.*, vol. 14, pp. 2–7, 2019.

[19] S. J. Kim *et al.*, "Improvement of Voltage Linearity in High- MIM Capacitors Using HfO 2 – SiO 2 Stacked Dielectric," *Ieee Electron Device Lett.*, vol. 25, no.

8, pp. 538–540, 2004.

[20] J. Yang *et al.*, “Effective Modulation of Quadratic Voltage Coefficient of Capacitance in MIM Capacitors Using Sm2O3/SiO2 Dielectric Stack,” *IEEE Electron Device Lett.*, vol. 30, no. 5, pp. 460–462, 2009.

[21] T. H. Phung *et al.*, “High Performance Metal-Insulator-Metal Capacitors with Er 2 O 3 on ALD SiO 2 for RF Applications,” *J. ofThe Electrochem. Soc.*, vol. 158, no. 12, pp. 1289–1292, 2011.

[22] J. H. Lee, Y. C. Lin, B. H. Chen, and C. Y. Tsai, “New metal-insulator-metal capacitor based on SrTiO3/Al2O3/SrTiO3laminate dielectric,” in *2010 10th IEEE International Conference on Solid-State and Integrated Circuit Technology*, 2010, pp. 1024–1026.

[23] C. Lin, Y. Wu, R. Jiang, and M. Yu, “MIM Capacitors Based onZrTiOxBaZryTi1−yO3Featuring Record-Low VCC and Excellent Reliability,” *IEEE Electron Device Lett.*, vol. 34, no. 11, pp. 1418–1420, 2013.

[24] S. Park *et al.*, “Analysis of reliability characteristics of high capacitance density MIM capacitors with SiO 2 – HfO 2 – SiO 2 dielectrics,” *Microelectron. Eng.*, vol. 88, pp. 3389–3392, 2011.

[25] J. Mu, X. Chou, Z. Ma, J. He, and J. Xiong, “High-performance MIM capacitors for a secondary power supply application,” *Micromachines*, vol. 9, no. 2, pp. 1–10, 2018.

[26] J. H. Klootwijk *et al.*, “Ultrahigh capacitance density for multiple ALD-Grown MIM capacitor stacks in 3-D silicon,” *IEEE Electron Device Lett.*, vol. 29, no. 7, pp. 740–742, 2008.

[27] L. Li *et al.*, “Three-dimensional AlZnO / Al2O3 / AlZnO nanocapacitor arrays on Si substrate for energy storage,” *Nanoscale Res. Lett.*, vol. 7, no. 1, p. 1, 2012.

[28] G. Zhang *et al.*, “Transparent nanotubular capacitors based on transplanted anodic aluminum oxide templates,” *ACS Appl. Mater. Interfaces*, vol. 7, no. 9, pp. 5522–5527, 2015.

[29] Y. K. Hong, B. H. Kim, D. Il Kim, D. H. Park, and J. Joo, “High-yield and

environment-minded fabrication of nanoporous anodic aluminum oxide templates," *RSC Adv.*, vol. 5, no. 34, pp. 26872–26877, 2015.

[30] L. Wei *et al.*, "Low-Cost and High-Productivity Three- Dimensional Nanocapacitors Based on Stand-Up ZnO Nanowires for Energy Storage," *Nanoscale Res. Lett.*, vol. 11, 2016.

[31] F. Han *et al.*, "Dielectric capacitors with three-dimensional nanoscale interdigital electrodes for energy storage," *Sci. Adv.*, vol. 1, no. 9, pp. 1–7, 2015.

[32] P. Banerjee, I. Perez, L. Henn-Lecordier, S. B. Lee, and G. W. Rubloff, "Nanotubular metal-insulator-metal capacitor arrays for energy storage," *Nat. Nanotechnol.*, vol. 4, no. 5, pp. 292–296, 2009.

[33] L. Wei *et al.*, "Low-Cost and High-Productivity Three-Dimensional Nanocapacitors Based on Stand-Up ZnO Nanowires for Energy Storage," *Nanoscale Res. Lett.*, vol. 11, no. 1, p. 213, 2016.

[34] M. Al, H. Gualous, N. Omar, and J. Van, "Batteries and Supercapacitors for Electric Vehicles," in *New Generation of Electric Vehicles*, InTech, 2012.

[35] A. González, E. Goikolea, J. A. Barrena, and R. Mysyk, "Review on supercapacitors: Technologies and materials," *Renew. Sustain. Energy Rev.*, vol. 58, pp. 1189–1206, 2016.

[36] "Supercapacitor Market," *Zion Market Research*, 2019. [Online]. Available: https://www.zionmarketresearch.com/market-analysis/super-capacitor-market. [Accessed: 07-Jun-2019].

[37] M. Yassine and D. Fabris, "Performance of commercially available supercapacitors," *Energies*, vol. 10, no. 9, 2017.

[38] A. Burke, "R&D considerations for the performance and application of electrochemical capacitors," *Electrochim. Acta*, vol. 53, no. 3 SPEC. ISS., pp. 1083–1091, 2007.

[39] P. L. Taberna, P. Simon, and J. F. Fauvarque, "Electrochemical Characteristics and Impedance Spectroscopy Studies of Carbon-Carbon Supercapacitors," *J. Electrochem. Soc.*, vol. 150, no. 3, p. A292, 2003.

[40] J. Palma, M. Anderson, G. A. Tiruye, D. Mu, and R. Marcilla, “Performance of solid state supercapacitors based on polymer electrolytes containing different ionic liquids,” *J. Power*, vol. 326, pp. 560–568, 2016.

[41] K. S. W. Sing, “Adsorption methods for the characterization of porous materials,” *Adv. Colloid Interface Sci.*, pp. 3–11, 1998.

[42] J. E. S. J. Signorelli, Riccardo; C-Ku, Daniel; G.Kassakain, “Electrochemical Double-Layer Capacitors Using Carbon Nanotube Electrode Structures,” *Proc. IEEE*, vol. 97, no. 11, pp. 1837–1847, 2009.

[43] K. Kierzek, E. Frackowiak, G. Lota, G. Gryglewicz, and J. Machnikowski, “Electrochemical capacitors based on highly porous carbons prepared by KOH activation,” *Electrochim. Acta*, vol. 49, no. 4, pp. 515–523, 2004.

[44] N. P. Katsuhiko and Simon, “New Materials and New Configurations for Advanced Electrochemical Capacitors,” *J. Electrochem. Soc.*, vol. 17, no. 1, pp. 34–37, 2008.

[45] S. Sinha, “Studies of activated carbons used in double-layer capacitors,” *J. Power Sources*, vol. 74, no. 1–2, pp. 99–107, 1998.

[46] E. Frackowiak and F. Béguin, “Carbon materials for the electrochemical storage of energy in capacitors,” *Carbon N. Y.*, vol. 39, no. 6, pp. 937–950, 2001.

[47] M. V. KIAMAHALLEH, S. H. S. ZEIN, G. NAJAFPOUR, S. A. SATA, and S. BUNIRAN, “Multiwalled Carbon Nanotubes Based Nanocomposites for Supercapacitors: a Review of Electrode Materials,” *Nano*, vol. 07, no. 02, p. 1230002, 2012.

[48] N. Zhang, S; Pan, “Supercapacitors Performance Evaluation,” *Adv. Energy Mater.*, 2015.

[49] I. Union, O. F. Pure, and A. Chemistry, “REPORTING PHYSISORPTION DATA FOR GAS / SOLID SYSTEMS with Special Reference to the Determination of Surface Area and Porosity,” *Pure Appl. Chem.*, vol. 57, no. 4, pp. 603–619, 1985.

[50] V. V. N. N. Obreja, A. Dinescu, and A. C. Obreja, “Activated carbon based electrodes in commercial supercapacitors and their performance,” *Int. Rev. Electr.*

Eng., vol. 5, no. February, pp. 272–281, 2010.

[51] S. Tabata, Y. Isshiki, and M. Watanabe, "Inverse opal carbons derived from a polymer precursor as electrode materials for electric double-layer capacitors," *J. Electrochem. Soc.*, vol. 155, no. 3, pp. 42–49, 2008.

[52] B. Dyatkin, O. Gogotsi, B. Malinovskiy, Y. Zozulya, P. Simon, and Y. Gogotsi, "High capacitance of coarse-grained carbide derived carbon electrodes," *J. Power Sources*, vol. 306, pp. 32–41, 2016.

[53] T. Ariyanto, B. Dyatkin, G.-R. Zhang, A. Kern, Y. Gogotsi, and B. J. M. Etzold, "Synthesis of carbon core–shell pore structures and their performance as supercapacitors," *Microporous Mesoporous Mater.*, vol. 218, pp. 130–136, 2015.

[54] Y. Korenblit *et al.*, "High-rate electrochemical capacitors based on ordered mesoporous silicon carbide-derived carbon," *ACS Nano*, vol. 4, no. 3, pp. 1337–1344, 2010.

[55] H. Pan, J. Li, and Y. Ping, "Carbon Nanotubes for Supercapacitor," *Nano Rev.*, vol. 5, pp. 654–668, 2010.

[56] K. Z. Kukovecz Á., Kozma G., "Multi-Walled Carbon Nanotubes," in *Springer Handbook of Nanomaterials*, Vajtai R, Ed. Springer, Berlin, Heidelberg, 2013, pp. 147–188.

[57] T. Chen and L. Dai, "Carbon nanomaterials for high-performance supercapacitors," *Mater. Today*, vol. 16, no. 7–8, pp. 272–280, 2013.

[58] L. Dai, L. Dai, D. W. Chang, J. Baek, and W. Lu, "Carbon Nanomaterials for Advanced Energy Conversion and Storage," *Nano micro small*, vol. 8, no. 8, pp. 1130–1166, 2012.

[59] A. Barroso-Bogeat, M. Alexandre-Franco, C. Fernández-González, A. Macías-García, and V. Gómez-Serrano, "Electrical conductivity of activated carbon-metal oxide nanocomposites under compression: A comparison study," *Phys. Chem. Chem. Phys.*, vol. 16, no. 45, pp. 25161–25175, 2014.

[60] J. Sengupta, "Carbon Nanotube Fabrication at Industrial Scale: Opportunities and Challenges," in *Handbook of Nanomaterials for Industrial Applications*, Elsevier

Inc., 2018, pp. 172–194.

[61] B. Kay *et al.*, “Electrochemical Properties of High-Power Supercapacitors Using Single-Walled Carbon Nanotube Electrodes **,” *Adv. Funct. Mater.*, vol. 11, no. 5, pp. 387–392, 2001.

[62] C. Niu, E. K. Sichel, R. Hoch, D. Moy, and H. Tennent, “High power electrochemical capacitors based on carbon nanotube electrodes electrodes,” *Appl. Phys. Lett.*, vol. 70, no. 1489, 1997.

[63] B. Adeniran and R. Mokaya, “Low temperature synthesized carbon nanotube superstructures with superior CO 2 and hydrogen storage capacity †,” *Mater. Chem. A*, vol. 3, pp. 5148–5161, 2015.

[64] E. Frackowiak, S. Delpeux, K. Jurewicz, and K. Szostak, “Enhanced capacitance of carbon nanotubes through chemical activation,” *Chem. Phys. Lett.*, vol. 361, no. July, pp. 35–41, 2002.

[65] C. Li *et al.*, “Oxidation of multiwalled carbon nanotubes by air : benefits for electric double layer capacitors,” *Powder Technol.*, vol. 142, pp. 175–179, 2004.

[66] H. Zhang, G. Cao, Y. Yang, and Z. Gu, “Comparison between electrochemical properties of aligned carbon nanotube array and entangled carbon nanotube electrodes,” *J. Electrochem. Soc.*, vol. 155, no. 2, pp. 19–23, 2008.

[67] M. S. Bell, K. B. K. Teo, R. G. Lacerda, W. I. Milne, D. B. Hash, and M. Meyyappan, “Carbon nanotubes by plasma-enhanced chemical vapor deposition,” *Pure Appl. Chem.*, vol. 78, no. 6, pp. 1117–1125, 2006.

[68] W. K. Wong, C. S. Lee, and S. T. Lee, “Uniform-diameter, aligned carbon nanotubes from microwave plasma-enhanced chemical-vapor deposition,” *J. Appl. Phys.*, vol. 97, no. 8, 2005.

[69] S. Ahmed, A. Aitani, F. Rahman, A. Al-Dawood, and F. Al-Muhaish, “Decomposition of hydrocarbons to hydrogen and carbon,” *Appl. Catal. A Gen.*, vol. 359, no. 1–2, pp. 1–24, 2009.

[70] C. Wu, M. A. Nahil, N. Miskolczi, J. Huang, and P. T. Williams, “Production and application of carbon nanotubes, as a co-product of hydrogen from the pyrolysis-

catalytic reforming of waste plastic," *Process Saf. Environ. Prot.*, vol. 103, pp. 107–114, 2016.

[71] K. Hata, D. N. Futaba, K. Mizuno, and T. Namai, "Water-Assisted Highly Efficient Synthesis of Impurity-Free Single-Walled Carbon Nanotubes," *Science (80-.).*, vol. 306, no. November, pp. 1362–1364, 2004.

[72] G. Wu *et al.*, "High-performance Supercapacitors Based on Electrochemical-induced Vertical-aligned Carbon Nanotubes and Polyaniline Nanocomposite Electrodes," *Sci. Rep.*, vol. 7, no. December 2016, pp. 1–8, 2017.

[73] H. C. Lee *et al.*, "Synthesis of Single-layer Graphene: A Review of Recent Development," *Procedia Chem.*, vol. 19, pp. 916–921, 2016.

[74] V. Singh, D. Joung, L. Zhai, S. Das, S. I. Khondaker, and S. Seal, "Graphene based materials: Past, present and future," *Prog. Mater. Sci.*, vol. 56, no. 8, pp. 1178–1271, 2011.

[75] K. Parvez *et al.*, "Exfoliation of Graphite into Graphene in Aqueous Solutions of Inorganic Salts," *J. Am. Chem. Soc.*, vol. 136, no. 16, pp. 6083–6091, Apr. 2014.

[76] T. C. Achee *et al.*, "High-yield scalable graphene nanosheet production from compressed graphite using electrochemical exfoliation," *Sci. Rep.*, vol. 8, no. 1, pp. 1–8, 2018.

[77] X. Wang, L. Zhi, and K. Mu, "[Nano Lett.,2008,8,323]Transparent, Conductive Graphene Electrodes for Dye-Sensitized Solar Cells.pdf," 2008.

[78] J. Chen, C. Li, and G. Shi, "Graphene materials for electrochemical capacitors," *J. Phys. Chem. Lett.*, vol. 4, no. 8, pp. 1244–1253, 2013.

[79] Y. Gao *et al.*, "Transparent, flexible, and solid-state supercapacitors based on graphene electrodes," *APL Mater.*, vol. 1, no. 1, p. 7, 2013.

[80] L. F. Aval, M. Ghoranneviss, and G. B. Pour, "High-performance supercapacitors based on the carbon nanotubes , graphene and graphite nanoparticles electrodes," *Heliyon*, no. September, p. e00862, 2018.

[81] Y. Zhu *et al.*, "Exfoliation of Graphite Oxide in Propylene Carbonate and Thermal

Oxide Platelets," *ACS Nano*, vol. 4, no. 2, pp. 1227–33, 2010.

[82] H. Tang, C. Yang, Z. Lin, Q. Yang, F. Kang, and C. P. Wong, "Electrospray-deposition of graphene electrodes: A simple technique to build high-performance supercapacitors," *Nanoscale*, vol. 7, no. 20, pp. 9133–9139, 2015.

[83] A. Varea, O. Monereo, E. Xuriguera, J. Daniel Prades, and A. Cirera, "Electrospray as a suitable technique for manufacturing carbon-based devices," *J. Phys. D. Appl. Phys.*, vol. 50, no. 31, 2017.

[84] J.-X. Yan *et al.*, "Highly Conductive Graphene Paper with Vertically Aligned Reduced Graphene Oxide Sheets Fabricated by Improved Electrospray Deposition Technique," *ACS Appl. Mater. Interfaces*, vol. 11, no. 11, pp. 10810–10817, Mar. 2019.

[85] H. R. Yu, S. Cho, M. J. Jung, and Y. S. Lee, "Electrochemical and structural characteristics of activated carbon-based electrodes modified via phosphoric acid," *Microporous Mesoporous Mater.*, vol. 172, pp. 131–135, 2013.

[86] A. Muzaffar, M. B. Ahamed, K. Deshmukh, and J. Thirumalai, "A review on recent advances in hybrid supercapacitors: Design, fabrication and applications," *Renew. Sustain. Energy Rev.*, vol. 101, no. October 2018, pp. 123–145, 2019.

[87] C. Rabelais, "TUTORIALS P ROGRAMME ISEE15Cap," in *4to International Symposium on Enhanced Electrochemical Capacitors.*, 2015, no. June.

[88] J. A. Fernández, T. Morishita, M. Toyoda, M. Inagaki, F. Stoeckli, and T. A. Centeno, "Performance of mesoporous carbons derived from poly(vinyl alcohol) in electrochemical capacitors," *J. Power Sources*, vol. 175, no. 1, pp. 675–679, 2008.

[89] K. Xia, Q. Gao, J. Jiang, and J. Hu, "Hierarchical porous carbons with controlled micropores and mesopores for supercapacitor electrode materials," *Carbon N. Y.*, vol. 46, no. 13, pp. 1718–1726, 2008.

[90] Y. Zhao *et al.*, "Easy synthesis of ordered meso/macroporous carbon monolith for use as electrode in electrochemical capacitors," *Mater. Lett.*, vol. 62, no. 3, pp. 548–551, 2008.

[91] Y. Zhu, S. Murali, M. D. Stoller, A. Velamakanni, R. D. Piner, and R. S. Ruoff, “Microwave assisted exfoliation and reduction of graphite oxide for ultracapacitors,” *Carbon N. Y.*, vol. 48, no. 7, pp. 2118–2122, 2010.

[92] C. Liu, Z. Yu, D. Neff, A. Zhamu, and B. Z. Jang, “Graphene-based supercapacitor with an ultrahigh energy density,” *Nano Lett.*, vol. 10, no. 12, pp. 4863–4868, 2010.

[93] H. Ji *et al.*, “Capacitance of carbon-based electrical double-layer capacitors,” *Nat. Commun.*, vol. 5, no. Cmcm, pp. 1–7, 2014.

[94] X. Chen *et al.*, “Novel electric double-layer capacitor with a coaxial fiber structure,” *Adv. Mater.*, vol. 25, no. 44, pp. 6436–6441, 2013.

[95] J. Xia, F. Chen, J. Li, and N. Tao, “Measurement of the quantum capacitance of graphene,” *Nat. Nanotechnol.*, vol. 4, no. 8, pp. 505–509, 2009.

CHAPTER III

Compendium of papers

3.1. Paper #1: Impedance modelling of silica nanoparticle metal insulator metal capacitors.

This work is published in Electrochimica Acta, Volume 280, 2018, Pages 62-70, https://doi.org/10.1016/j.electacta.2018.05.084.

Electrochimica Acta 280 (2018) 62–70

Contents lists available at ScienceDirect

Electrochimica Acta

journal homepage: www.elsevier.com/locate/electacta

Impedance modeling of silica nanoparticle metal insulator metal capacitors

Bremnen Véliz [a, b], Sandra Bermejo [a, *], Albert Orpella [a], Luis Castañer [a]

[a] Polytechnic University of Catalonia, Dept. of Electronic Engineering, MNT Group, Barcelona, Spain
[b] Santa Elena Peninsula University, Faculty of Electronics and Telecommunications, Santa Elena, Ecuador

ARTICLE INFO

Article history:
Received 19 December 2017
Received in revised form
14 April 2018
Accepted 13 May 2018
Available online 17 May 2018

Keywords:
Metal-insulator-metal
Silica nanospheres
Electrochemical impedance spectroscopy
Warburg impedance
Constant phase element
Electrospray

ABSTRACT

In this study, we have fabricated metal-insulator-metal (MIM) capacitors where the insulator layer is made of 255 nm diameter silica nanospheres. The MIM devices have been characterized and modeled by electrochemical impedance spectroscopy (EIS) and charge-discharge transients. Fitting the results with modified Randles models agreed well with three constant phase elements, three leakage resistors, and a Warburg element. According to the results of the fitting of the charge-discharge measurements and of the modified Randles model, values of real capacitances up to thousand times larger than the theoretical capacitance of a similar capacitor with a continuous layer dielectric are found. These unexpected high capacitances seemed to be related to the ability of the nanospheres to trap electric charges due to surface hydroxyl groups that are originated by the adsorption of water molecules, thereby indicating that the environmental humidity plays a role. This has been ascertained by measurements at several temperatures above the ambient and the resulting capacitance decreases as temperatures increases. Furthermore, active and reactive parts of the complex power have been measured showing capacitive or resistive behavior depending on the frequency. These results suggest that this novel MIM device based on nanospheres may be a new baseline technology for supercapacitor technology.

1. Introduction

The current trend of increasing demand of power storage for several applications has stimulated research on supercapacitors [1] which have higher energy density than electrolytic capacitors and are able to deliver energy faster than batteries. According to the mechanism of energy storage, supercapacitors can be classified [2] into: Electrical Double Layer (EDLC) capacitors based on electrostatic charge between a microporous conducting electrode and an electrolyte (there is not charge-transfer reaction); Pseudo-capacitors [3] based on reversible redox reactions of a transition metal oxide or conducting polymers with an electrolyte, and Hybrid capacitors based on a combination of both mechanisms.

Oxide nanoparticles onto carbon electrodes have been used to increase the specific capacitance. For example, in Ref. [4] a chemical bath is used to deposit nickel oxide nanoparticles onto porous activated carbon monoliths to implement supercapacitor electrodes, and synthesized mesoporous manganese dioxide nanoparticles [5] have been used by a soft template method using a cationic surfactant to composite an electrode with carbon black.

Recent advances in nanoparticle Metal Insulator Metal structures (MIM) are discussed in this work. A layer of silica nanospheres takes the place of the insulator layer and the potential to increase the capacitance is evaluated, despite that these MIM structures are not pseudo-capacitors as silica is not a transition metal oxide, there is not a porous conducting material and no electrolyte is involved. However, despite the fact that a redox reaction does not occur in the interface of the silica, a capacitance increase has been previously reported [6] when a silica nanoparticle layer was coated on the top of the electrodes by tumbling and dip-coating methods.

In a previous paper [7] our group described a MIM capacitor that was built depositing silica nanoparticles by electrospray onto a planar aluminum plate electrode and covering the nanoparticles with a thin layer of evaporated aluminum as the second electrode.

Electrospray is a well-known technique for deposition of nanoparticle layers [8] from an aqueous dispersion using high voltage, in relatively short times and large areas compared to other methods such as vertical deposition, Langmuir- Blodgett, spin-on

* Corresponding author. Micro and Nanotechnologies Group, c/. Jordi Girona 1-3, Campus Nord, 08034, Barcelona, Spain.
E-mail address: sandra.bermejo@upc.edu (S. Bermejo).

https://doi.org/10.1016/j.electacta.2018.05.084
0013-4686/

and tumbling. As a follow up of our previous work, we report in Section 2 below the experimental approach, followed by Section 3 with a detailed description of the impedance spectroscopy results based in Randles impedance model [9]. The effect of the temperature has been also analyzed and interpreted.

2. Experimental

2.1. Fabrication

Several MIM structures were fabricated to make sure that the results were qualitatively reproducible. The MIM structures were fabricated using the steps shown in Fig. 1: A dispersion of positive photoresist is spun onto a glass substrate creating a uniform photoresist layer which is exposed to UV light through a first mask (a). The photo-layer is then patterned to create the bottom electrode (b). A thin aluminum film is then deposited by thermal evaporation and patterned by lift-off (c). A second photoresist layer is spun on the surface (d) and, with the use of a second mask, two windows are patterned (e): one to create the active area of the MIM capacitor and the second to allow the electrical contact to the bottom plate. Next a nozzle is placed at a distance of 5 cm on top of the active area window and the electrospray process is triggered when a high DC voltage is applied between the nozzle (around 5.3 kV and 6.3 kV) and the bottom plate electrode is biased to a negative voltage (typically between −1 kV and −1.4 kV). The colloidal fluid we have used is composed by a 95% DI water and a 5% of silica nanospheres. It is pumped through the nozzle with a flow rate set at 0.4 mL h^{-1} or 0.3 mL h^{-1}. The solution of 255 nm diameter nanospheres is then electrosprayed for about 10 min (f) and they are dried in nitrogen flow at 2 bars of pressure. Finally, the top electrode is created by depositing an Al film by thermal evaporation through a shadow mask (g).

The top view of the MIM structures is shown in Fig. 2. Where the active area is 20.25 mm^2.

2.2. Characterization

SEM/FIB measurements, electrochemical impedance spectroscopy, complex power and charge-discharge transient characterization were carried out to study these devices.

Real and imaginary parts of the impedance were measured for three MIM structures in this work (MIM A, MIM B and MIM C) at room temperature, using a Hioki IM3590 impedance analyzer and an Agilent 4294A covering the frequency range from 0.1 Hz to 1 MHz. The sinusoidal signal was 500 mV amplitude and 0 mV bias.

A fourth MIM (MIM D) was placed on a thermal chuck and it was heated to 30 °C, 35 °C, 45 °C and 50 °C using a STC200 temperature controller, the impedance was measured using a Hioki IM3590 analyzer impedance over the frequency range from 0.1 to 100 kHzH at 500 mV.

From the impedance spectroscopy measurements described above, a normalized AC power analysis was performed to find out how the active and reactive powers depend on the frequency.

Transient experiments have been performed using a circuit arrangement where the MIM structure is placed in series with a Ro commercial resistor and the voltage across is registered following a square wave input. An Agilent 33250A function waveform generator was used to supply a positive and periodic square waveform of 1.2 V peak amplitude. An Agilent MSO7054A digital oscilloscope

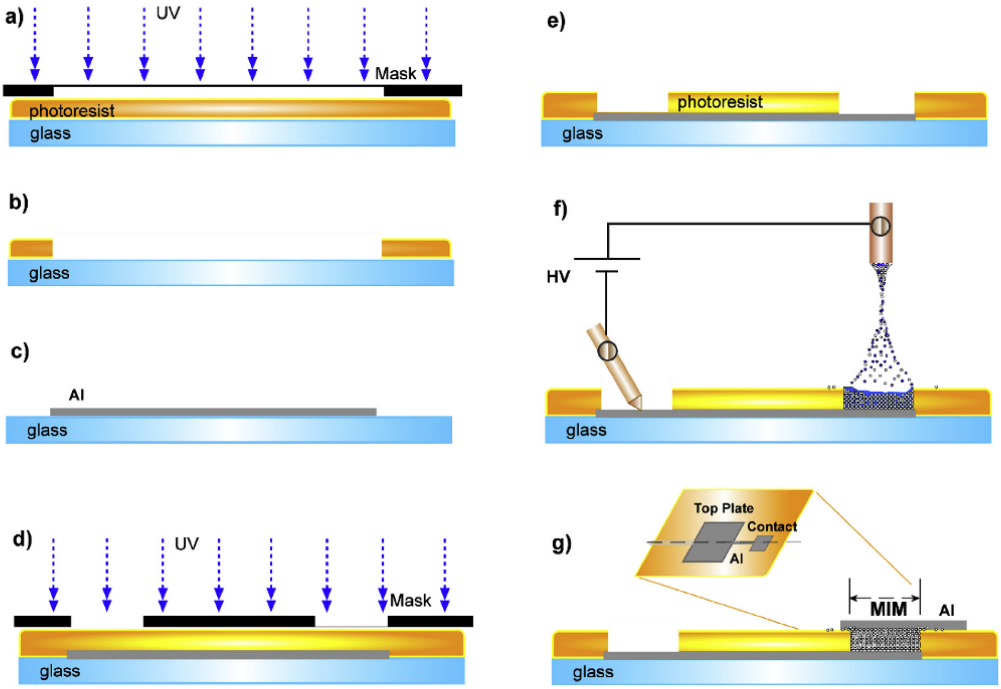

Fig. 1. Proceeding of the samples fabrication: a) Spin-coat of the photoresist and lithography, b) Definition of the bottom electrode, c) Aluminum deposition and lift-off, d) Spin-coat of photoresist and lithography, e) Opening of the bottom contact, f) silica nanospheres electrospraying, g) Aluminum deposition of the top electrode and top view.

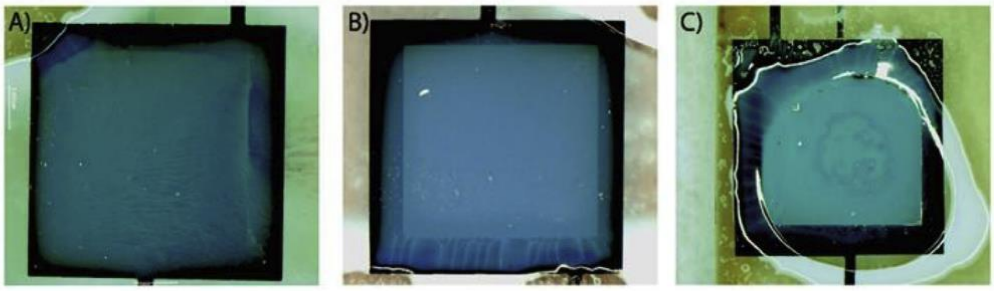

Fig. 2. Top view of MIM structures A, B and C with main parameters shown in Table 1.

was used to acquire the output signal at Ro.

3. Results and discussion

3.1. SEM/FIB characterization

Fig. 3 shows SEM cross section images after FIB drill of three MIM structures, named A, B and C, as representative of the devices we have produced during this work. A random ordering of the nanospheres is observed in the three samples: MIM A (Fig. 3. A), MIM B (Fig. 3B) and MIM C (Fig. 3C). Table 1 summarizes the thicknesses of the layers deposited. Different thicknesses are achieved by varying slightly the flow and time of the deposition. The thinnest layer is MIM C with 1.51 μm.

Regular flat surfaces are observed in all the MIM structures shown in Fig. 4 with the exception of MIM C, where an elevated region with a detached portion is observed on the upper edge of Fig. 4C, we interpret this result to be a consequence of the drying process dynamics tending to aggregate more particles in the periphery, especially in the thinnest sample, creating mountains and breaks on the borders. So this area is prone to crack.

Table 1
Metals and dielectric layers thicknesses.

MiM	Bottom metal [μm]	Top metal [μm]	Dielectric [μm]
A	0.24	0.40	11.3
B	0.39	0.42	5.49
C	0.23	0.41	1.51

3.2. Impedance spectroscopy measurements and Nyquist plots

The Impedance is a function of frequency and it is defined by the following equation:

$$Z(\varpi) = \mathrm{Re}(Z) + j\mathrm{Im}(Z) = \frac{1}{j\varpi C^*} \quad (1)$$

where Re(Z) and Im(Z) are the real and imaginary parts of the impedance and a complex capacitance C* [10] can be defined by:

$$C^* = C' - jC'' \quad (2)$$

The real part of the capacitance [11] is defined as:

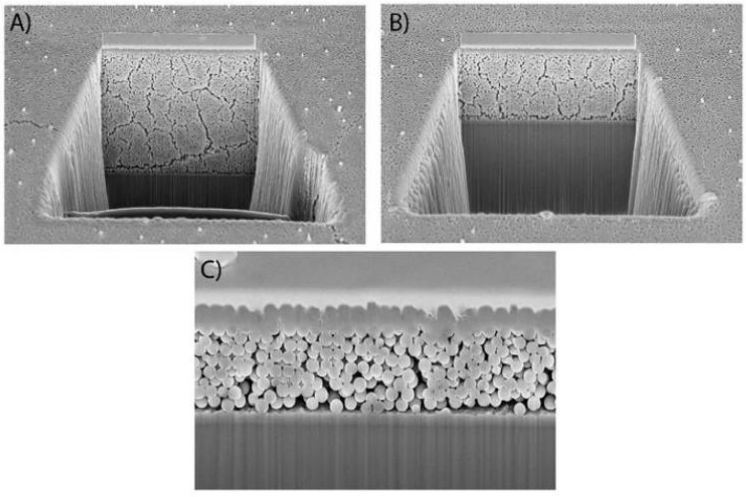

Fig. 3. Drilled cross section SEM images of the three Mim structures A, B and C. Nanospheres are arranged in disorderly between two aluminum layers.

Fig. 4. Surface top view of the MIM structures. All MIMs have flat surface, but MIM C also has on the upper edge an elevation region.

$$C' = \frac{-\mathrm{Im}(Z)}{\varpi |Z(\varpi)|^2} \tag{3}$$

C' represents the capacitance that can be measured by cyclic voltammetry or galvano-static cycling methods. C'' is the imaginary part of the complex capacitance and is related to the energy loss by the capacitor by free charge motion and dipole alignment.

Fig. 5 A, B and C show the Nyquist plots of the impedance measurements of the three MIM structures showing a lineal behavior at low frequency followed by depressed semicircular shape at higher frequency. In order to interpret the results we have fitted the measurements with the circuit model shown in Fig. 5D, consisting on the series arrangement of three parallel sub-circuits involving three constant phase elements (CPE_1, CPE_2 and CPE_3), one Warburg element (Z_W) and three resistors (R_1, R_2 and R_3). We have tried to fit the experimental measurement with equivalent circuits with less elements but the best agreement was found using such more complex model.

A constant phase element is an empirical element without an exact physical meaning [12], but it is generally attributed to a double layer. We interpret, in our case that the three constant phase elements CPE_1 CPE_2 and CPE_3 can be attributed to double layers at the nanospheres/metal interfaces and to an effective nanosphere/nanosphere interface. The CPE impedance is defined as:

$$Z_{CPE} = \frac{1}{Q_C (jw)^{\alpha}} \tag{4}$$

where the dispersion exponent is $0 < \alpha < 1$. Q_C is a coefficient

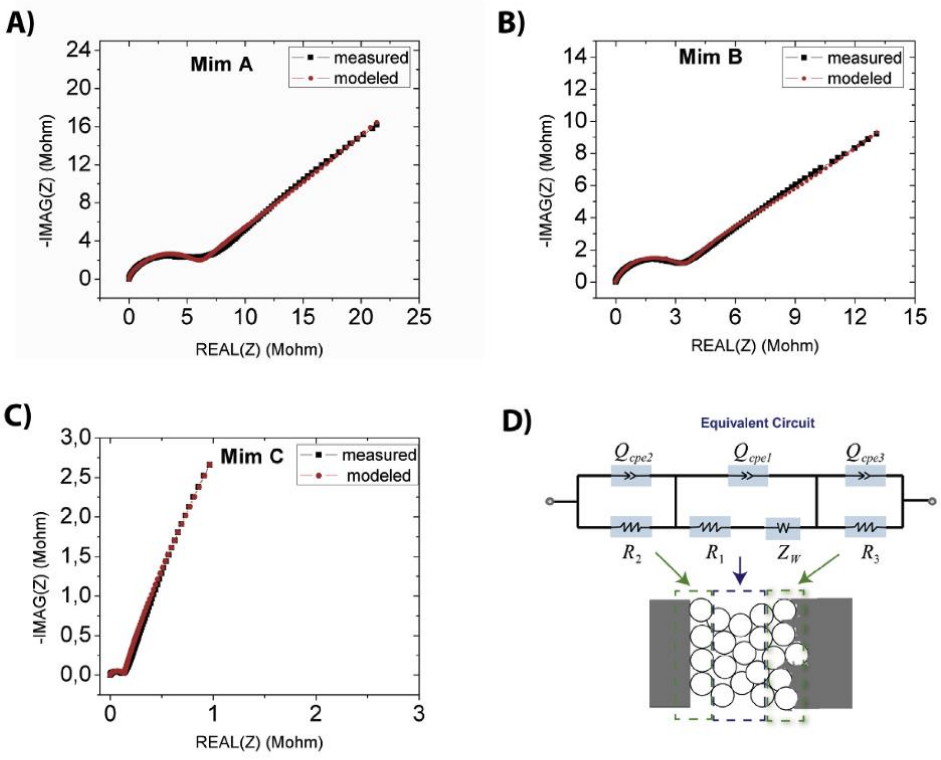

Fig. 5. Nyquist plots measured (■) and modeled (●) for the MIM structures. A) MIM A. B) MIM B and C) MIM C. D) Equivalent Circuit of our modeled MIM structures.

independent of the frequency. This impedance is a capacitance only when $\alpha = 1$. Clearly, a CPE works like a non ideal capacitor [13].

The resistances R_1, R_2, R_3 take into account dissipative processes due to the charge transfer of electrons and ions (hydrogen H^+ and hydronium H_3O^+) that can migrate through the water molecules and the hydroxyl groups [14] through the silica nanospheres and interfaces.

The Warburg element Z_W is usually associated to the diffusion of electrolytic ions and electrical double layer [15]. The only weak electrolyte used in the course of our fabrication is deionized water, so the Warburg impedance takes into account the diffusion of charges involving H^+ and H_3O^- ions around the periphery of the nanospheres. This effect has been already reported in humidity sensors made of silica nanoparticles aerogels [16,17]. The hydronium H_3O^+ ions result from the interaction of water molecules with H^+ ions bonded to hydroxyl OH^- group. Furthermore, H^+ and OH^- ions are created by self-dissociation of the water vapor. The water molecules would come from the remainder trapped water after electrospray that is located at the nanospheres interstices and from the humidity of the environment. In addition, studies [18] based on thermal gravimetric and infrared spectra analysis have reported that silica nanosphere structures have the ability to physically absorb large amount of water molecules (12%) from the ambient moisture through hydroxyl groups bond to the surface (Si-OH).

The Warburg impedance Z_W used in our model is defined [19] by the equation:

$$Z_W = \frac{A_W}{\sqrt{\omega}}(1-j) = \frac{\sqrt{2}A_W}{\sqrt{j\omega}} \tag{5}$$

where A_W is the Warburg coefficient and ω is the angular frequency.

Table 2 shows the best fit values for the equivalent circuit model for the three samples. It is difficult to assign a perfect physical origin to each sub-circuit due to the behavioral nature of them. We can however associate the left sub-circuit to the bottom contact and the right one to the upper contact whereas the Warburg sub-circuit can be associated to the nanoparticles themselves.

We have also added to Table 2 the real capacitance C′ at 0.1 Hz and the estimated value of the theoretical capacitance C_{TH} of a similar structure (same size and thickness), but with a continuous and homogeneous silicon dioxide dielectric layer with the relative permittivity equal to $\varepsilon_r = 3.9$.

As can be seen in Table 2 all C′ values are greater than C_{TH} in two to three orders of magnitude. MIM A has a ratio of 589, for MIM B is 449 and for MIM C is 1148 times. The largest capacitance value is found for the thinnest device. The 45° line in the Nyquist plot is typical of a diffusion process and the semicircle is usually interpreted as due to the conductivity of the ions and interface polarization. These are observed in the Nyquist plots of MIM A and MIM B in Fig. 5. Also, the MIM C is much more vertical and the semicircle is almost unobservable. Our fitting revealed that the linearity was better when the magnitude of the Warburg impedance was greater than the other resistors, especially R_1 and R_2. The better capacitive behavior (most linear Nyquist) is for the MIM C, whose Warburg coefficient A_W is 630 times larger than R_1, 60 times than R_2 and 90 times than R_3. For the MIM A and MIM B, the magnitude of A_W, R_1 and R_2 are of the same order.

Desorption and adsorption of water from the environment may have affected the measurements as the evaporation of water tends to increase the value of the leakage resistors compared to the Warburg impedance. This is supported by the results of humidity sensors based on oxides, as it has been demonstrated that the conductivity increases as water concentration increases [20,17,21]. In order to evaluate the effect of humidity, we have fabricated another MIM structure with a square area of 3.24 mm^2 called MIM D with a dielectric thickness of 1.013 μm and it has been heated at 30 °C, 35 °C, 45 °C and 50 °C. Nyquist plots are shown in Fig. 6A. It is observed that with the increase in temperature, the radius of the semicircle increases. The loss of water mainly is reflected in the Nyquist modeling by means of the increase of the resistors (R_1, R_2 and R_3) and the reduction of the Warburg (A_W) as is shown in Table 3. The Nyquist fit also shows a decrease in the constant element phase Q_{CPE1}. As a conclusion, when the relation between

Table 2
Fitting parameter for the equivalent circuit of the Silica nanospheres MIM Structures, $s = j\omega$.

Mim	Q_{cpe1} $nFs^{\alpha-1}$	α_1	R_1 MΩ	A_W $M\Omega s^{1/2}$	Q_{cpe2} $nFs^{\alpha-1}$	α_2	R_2 MΩ	Q_{cpe3} nF	α_3	R_3 MΩ	C′ nF	C_{TH} pF
A	20	0.83	7	14	0.6	0.93	5.0	0.62	0.92	0.900	35.88	61.85
B	38	0.79	7	7.6	1	0.89	3.2	1.2	0.99	0.110	57.26	127.31
C	430	0.9	0.01	6.3	6.0	0.83	0.11	20.0	1.00	0.024	531.7	462.87

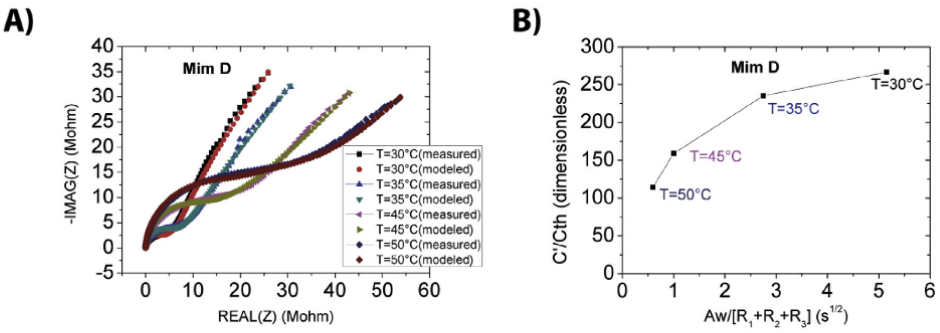

Fig. 6. MIM structure D Nyquist from 0.1Hz to 100 kHz at different temperature. A) For 30 °C measured (■), modeled (●); for 35 °C measured (▲, modeled (▼); for 45 °C measured (◀), modeled (▶); for 50 °C measured (♦), modeled (♦). B) C′ versus Aw $(R1+R2+R3)^{-1}$.

Table 3
Fitting parameter for MIM structure D at 30 °C, 35 °C, 45 °C and 50 °C.

T		Q_{cpe1}	α_1	R_1	A_W	Q_{cpe2}	α_2	R_2	Q_{cpe3}	α_3	R_3	C'	C_{TH}
°C		$nFs^{\alpha-1}$		MΩ	$M\Omega s^{1/2}$	$nFs^{\alpha-1}$		MΩ	nF		MΩ	nF	pF
30	16	0.96	0.6	34	1.1	0.96	4.2	20.0	0.95	2.0	29.44	110	
35	12	0.96	2	28	1.1	0.96	6.2	20.0	0.95	2.0	25.95	110	
45	8.6	0.96	9	24	1.4	0.96	12.0	20.0	0.95	3.0	17.52	110	
50	8.6	0.96	12	22	1.4	0.96	18.0	20.0	0.95	7.0	12.59	110	

the Warburg and the other resistors decrease then the ratio C'/C_{TH} also decreases as shown in Fig. 6B. For instance, when temperature is 30 °C, C'/C_{TH} is 267; and when temperature is 50 °C, C'/C_{TH} is 114.

3.3. Complex power characterization

The complex power S can be written in terms of the active P and reactive powers as:

$$S = P + jQ \tag{6}$$

$$P/|S| = \cos(\phi) = \frac{\mathrm{Re}(Z)}{|Z|} \tag{7}$$

$$Q/|S| = \sin(\phi) = \frac{\mathrm{Im}(Z)}{|Z|} \tag{8}$$

where φ is the phase of the impedance Z and equal to the angle of the power triangle formed by complex power S, active power P and reactive power Q.

A figure of merit [22] called dielectric relaxation time Γ_O represents the frontier from a purely resistive to a purely capacitive behavior [23] and is a measure of how fast is able to deliver charge. Γ_O is graphically derived from the frequency ($1/f_O$ or relaxation frequency) at the intersection of the P/|S| and Q/|S| curves as a function of frequency.

Fig. 7 shows such diagrams with crossing point located at P/|S| − Q/|S| − 0.707 that corresponds to φ = −45°. The power curves fit every well with the model using the value of the parameters in Table 2 for frequencies under 10 kHz, but depart at higher frequencies.

From Fig. 7C it can be seen that the results for MIM C have two crossing points at 2.57 Hz and 2.09 kHz. For frequencies bellow 2.57 Hz, it is an excellent storage capacitor because Q/|S| > P/|S|. At intermediate frequencies from 2.57 Hz to 2.09 kHz, it dissipates

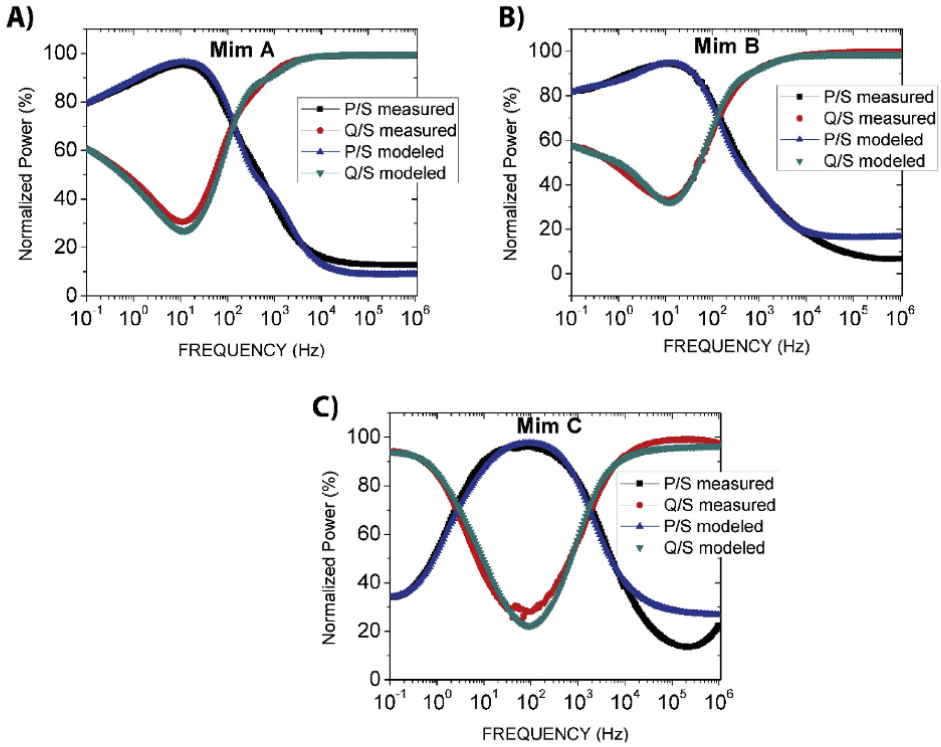

Fig. 7. Measured normalized: active power (■) and reactive power (●) versus frequency plots. Modeled normalized active power (▲) and reactive power (▼). A) MIM structure A, B) MIM structure B, C) MIM structure C.

power because Q/|S| < P/|S|. Finally, at higher frequencies it is able again to store energy. The frequency of 2.57 Hz allows to calculate a dielectric relaxation time ($\Gamma_O = 1/f_O$) equal to 0.389s.

MIM Structures A and B have very similar plots with close values of the crossing frequency, namely 141.2 Hz and 151.25 Hz for MIM structures A and B respectively. There are losses at low frequency as the behavior is resistive while above the crossing frequency have capacitive behavior. The relaxation time can be estimated to be higher than 10s.

Smaller values of relaxation time mean that the time to discharge energy is shorter. Therefore MIM C is better than MIM A and MIM B in that respect. Moreover, MIM C has a good relaxation time compared to double layer carbon capacitors in the range 1s-70s [23,24,25]. However, it is not better than Graphene-Conducting Polymers Supercapacitor 8 ms-27 ms [26] or Electrochemically Reduced Graphene Oxide Supercapacitor 1.35 ms [27].

3.4. Charge-discharge transient response

The bottom plate of the MIM structure is connected to an end of Ro. A waveform generator is connected to the other plate. The circuit analyzed is shown in Fig. 8D where $V_G = 1.2$ V, $R_O = 10M\Omega$ and $R_I = 1M\Omega$ is the oscilloscope input impedance. Vo is the output voltage measured with a digital oscilloscope.

The charge-discharge transient response has also been simulated. In order to simulate the transient behavior, we have derived a transfer function in the Laplace domain.

Replacing each CPE impedance from the Randles circuit by a fractional capacitor [28] of α order in the Laplace domain:

$$Z_{CPE}(s) = \frac{V(s)}{I(s)} = \frac{1}{s^{\alpha} Q_C} \tag{9}$$

where $0 < \alpha < 1$. The deduction of equation (9) can be easily developed using the definition of the CPE current in equation (10) and the Laplace transform of the Grünwald-Letnikov fractional operator [29] shown in equation (11):

$$i_{cpe}(t) = Q_C \frac{d^{\alpha} v(t)}{dt^{\alpha}} = Q_C [D^{\alpha} v(t)] \tag{10}$$

$$L\{D^{\alpha} v(t)\} = s^{\alpha} V(s) \tag{11}$$

With zero initial condition, the complex impedance in the Laplace domain is given by:

$$Z(s) = \frac{R_1 s^{0.5} + \sqrt{2} A_W}{R_1 Q_1 s^{\alpha_1 + 0.5} + \sqrt{2} A_W Q_1 s^{\alpha_1} + s^{0.5}} + \frac{R_2}{1 + R_2 Q_2 s^{\alpha_2}} + \frac{R_3}{1 + R_3 Q_3 s^{\alpha_3}} \tag{12}$$

We have used FOMCON Matlab toolbox supplied by Ref. [30], to find out the transfer function Vo/Vi:

$$\frac{V_o(s)}{V_i(s)} = H(s) = \frac{R_O || R_I}{Z(s) + R_O || R_I} \tag{13}$$

The time response can be derived from equation (13).

Fig. 8 shows comparisons of the transient measured with the

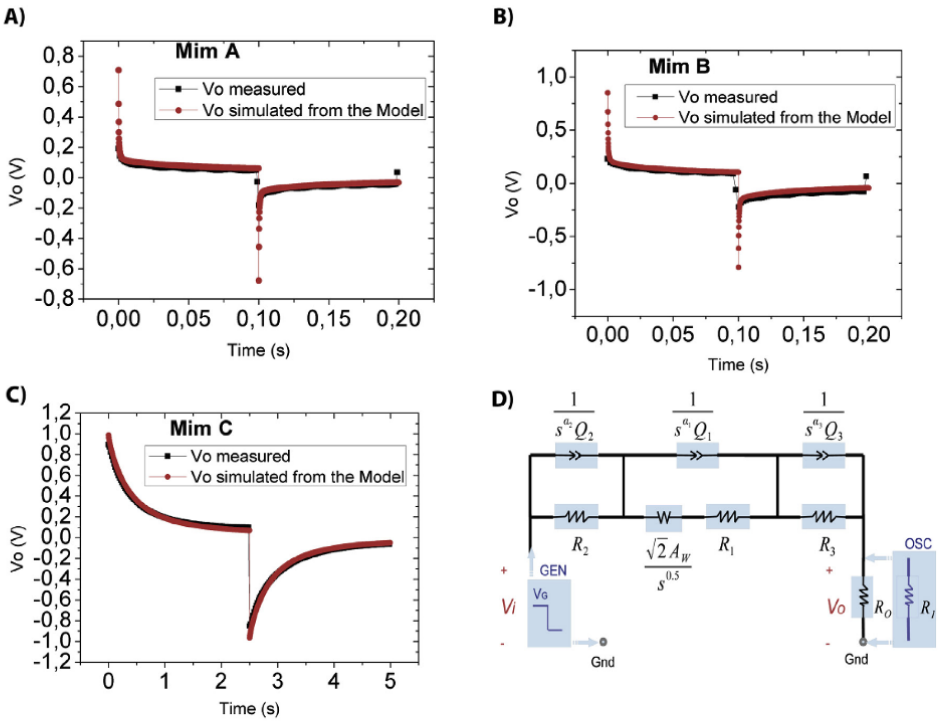

Fig. 8. Transient response measured (■) and modeled (●) at Ro placed in series with a MIM and exited by a periodic quadratic signal voltage: A) MIM A with frequency generator of 5 Hz, B) MIM B with frequency generator of 5 Hz, C) MIM C with frequency generator of 200 mHz, D) Circuit diagram.

simulated data. At the first semi-cycle, V_O is positive and decrease because the generator voltage applies a positive signal and all constant phase elements are charging. V_O has a final voltage value about 50 mV, 90 mV and 70 mV for MIM A, MIM B and MIM C respectively due to voltage divider produced by the resistors when the CPEs are fully charged as open circuits. The second semi-cycle starts when the generator voltage is zero; V_O is negative because it is in parallel with the MIM being the CPEs discharging.

The excitation signal had a frequency of 5 Hz for MIM A and MIM B; and 200 mHz for MIM C. The almost flat curves indicate that they work more as resistors than as capacitors which is reasonable since Fig. 7A and B show a greater power dissipation at that frequency.

On the other hand, Fig. 8C shows that MIM C has a better capacitive behavior confirming the analysis made in the previous sections. In fact, the MIM C curve can be approached to a first order model to extract a time constant:

$$\tau = C_P(R_P||R_O||R_I) \quad (14)$$

where the MIM circuit is considered to be formed by a C_P and a R_P in parallel. The results were $C_P - 485$ nF and $R_P - 8.8$MΩ. As can be expected, they closely resemble the value of real capacitance C′ and $A_W+R_1+R_2+R_3$ of Table 2. Surely, a greater contribution of humidity together with its finest thickness favored that the MIM C has a better performance than the others MIMs.

4. Conclusion

Metal-insulator-metal structures consisted by 255 nm diameter disordered silica nanospheres as insulator layer have been fabricated by electrospray and microelectronic techniques, their capacitive characteristics are explored by electrochemical impedance spectroscopy and charge-discharge measurements.

The MIM structures can be modeled using an equivalent circuit model formed by three constant phase elements (CPE), one Warburg element (Z_W) and three resistors (R_1, R_2 and R_3). The estimated capacitances were greater than theoretical capacitances C_{TH} in a factor of approximately 500 up to 1100 for the fabricated samples. The difference in values is primarily due to the inverse relation with the thickness of the dielectric layer. The large increase in the capacitances is attributed in part to the ability of silica nanospheres to adsorb and retain water molecules allowing the electrical conduction of ions such as H^- hydrogen and H_3O^+ hydronium. This statement was confirmed when we removed adsorbed water by heating of a MIM structure, the increase in temperature reduced the capacitance due to evaporation of adsorbed water at the nanosphere interstices.

The Randles model was used to predict the transient response when the MIM was charged and discharged connected in series with a resistance. From the transient response, a time constant for an exponential discharge of first order can be approximated to obtain a capacitance value similar to circuit model. Complex power analysis indicates that some samples exhibit a more resistive than capacitive behavior, depending on the applied frequency.

Defects inherent to the technology deposition of nanospheres such as small breaks or regions higher on the borders of the nanostructures should be enhanced, especially for thin nanoparticles layer thicknesses. The ambient humidity was no deliberately controlled, but the observed results indicate that the use of other electrolyte instead of DI water can improve the performance of the device.

Acknowledgement

This work has been supported by the Spanish Ministry of Science and Innovation under projects TEC2014-59736-R, ESP2016-79612-C3-2-R and by SENESCYT of the republic of Ecuador. The authors thank Triffon Triffonov by the measurement performed at CRNE.

References

[1] P. Jampani, a. Manivannan, P.N. Kumta, Advancing the supercapacitor materials and technology frontier for improving power quality, Electrochem. Soc. Interface 19 (2010) 57–62. https://www.electrochem.org/dl/interface/fal/fal10/fal10_p057-062.pdf.
[2] A. González, E. Goikolea, J.A. Barrena, R. Mysyk, Review on supercapacitors: technologies and materials, Renew. Sustain. Energy Rev. 58 (2016) 1189–1206, https://doi.org/10.1016/j.rser.2015.12.249.
[3] D.P. Dubal, G.S. Gund, R. Holze, H.S. Jadhav, C.D. Lokhande, C.J. Park, Solution-based binder-free synthetic approach of RuO2 thin films for all solid state supercapacitors, Electrochim. Acta 103 (2013) 103–109, https://doi.org/10.1016/j.electacta.2013.04.055.
[4] N.H. Basri, M. Deraman, M. Suleman, N.S.M. Nor, B.N.M. Dolah, M.I. Sahri, S.A. Shamsudin, Energy and power of supercapacitor using carbon electrode deposited with nanoparticles nickel oxide, Int. J. Electrochem. Sci. 11 (2016) 95–110.
[5] S. Devaraj, G.S. Gabriel, S.R. Gajjela, P. Balaya, Mesoporous MnO2 and its capacitive behavior, Electrochem. Solid state Lett. 15 (2012) 57–59, https://doi.org/10.1149/2.016204esl.
[6] K.C. Leonard, W.F. Suyama, M.A. Anderson, Evaluating the electrochemical capacitance of surface-charged nanoparticle oxide coatings, Langmuir 28 (2012) 6476–6484, https://doi.org/10.1021/la204173w.
[7] B. Veliz, S. Bermejo, A. Coll, L. Castañer, Metal-insulator-metal capacitor using electrosprayed nanoparticles, Appl. Phys. Lett. 105 (2014) 1–5, https://doi.org/10.1063/1.4889746.
[8] A. Coll, S. Bermejo, D. Hernández, L. Castañer, Colloidal crystals by electrospraying polystyrene nanofluids, Nanoscale Res. Lett. 8 (2013), https://doi.org/10.1186/1556-276X-8-26.
[9] C. Rabelais, Tutorials programme ISEE15Cap, in: 4to Int. Symp. Enhanc. Electrochem. Capacit., 2015.
[10] C. Yang, C.-Y.V. Li, F. Li, K.-Y. Chan, Complex impedance with transmission line model and complex capacitance analysis of ion transport and accumulation in hierarchical core-shell porous carbons, J. Electrochem. Soc. 160 (2013) H271–H278, https://doi.org/10.1149/2.016306jes.
[11] P.L. Taberna, P. Simon, J.F. Fauvarque, Electrochemical characteristics and impedance spectroscopy studies of carbon-carbon supercapacitors, J. Electrochem. Soc. 150 (2003) A292, https://doi.org/10.1149/1.1543948.
[12] S.M. Rezaei Niya, M. Hoorfar, On a possible physical origin of the constant phase element, Electrochim. Acta 188 (2016) 98–102, https://doi.org/10.1016/j.electacta.2015.11.142.
[13] G. Láng, K.E. Heusler, On the electrical capacitance of interfaces exhibiting constant phase element behaviour, J. Electroanal. Chem. 457 (1998) 257–260, https://doi.org/10.1016/S0022-0728(98)00301-5.
[14] H. Farahani, R. Wagiran, M.N. izar Hamidon, Humidity Sensors Principle, Mechanism, and Fabrication Technologies: a Comprehensive Review, 2014, https://doi.org/10.3390/s140507881.
[15] J.O. Bockris, A.K.N. Reddy, The electrifiec interface, in: Mod. Electrochem. Fundam. Electrodics, Second, Kluwer Academic/Plenum, New York, Boston, Dordrecht, London, Moscow, 2000, pp. 771–890.
[16] C.T. Wang, C.L. Wu, I.C. Chen, Y.H. Huang, Humidity sensors based on silica nanoparticle aerogel thin films, Sens. Actuators B Chem. 107 (2005) 402–410, https://doi.org/10.1016/j.snb.2004.10.034.
[17] C.-D. Feng, S.-L. Sun, H. Wang, C.U. Segre, J.R. Stetter, Humidity sensing properties of Nation and sol-gel derived SiO_2/Nafion composite thin films, Sens. Actuators B Chem. 40 (1997) 217–222, https://doi.org/10.1016/S0925-4005(97)80265-1.
[18] F. Gallego-Gómez, A. Blanco, D. Golmayo, C. López, Three regimes of water adsorption in annealed silica opals and optical assessment, Langmuir 27 (2011) 13992–13995, https://doi.org/10.1021/la203529s.
[19] A.I. Zia, S.C. Mukhopadhyay, Electrochemical sensing: carcinogens in beverages, in: Electrochem. Sens. Carcinog. Beverages, Springer International Publishing Switzerland, 2016, pp. 21–37, https://doi.org/10.1007/978-3-319-32655-9.
[20] J.H. Anderson, G.A. Parks, The electrical conductivity of silica gel in the presence of adsorbed water, J. Phys. Chem. 72 (1968) 3662–3668, https://doi.org/10.1021/j100856a051.
[21] H. Bi, K. Yin, X. Xie, J. Ji, S. Wan, L. Sun, M. Terrones, M.S. Dresselhaus, Ultrahigh humidity sensitivity of graphene oxide, Sci. Rep. 3 (2013) 2714, https://doi.org/10.1038/srep02714.
[22] J. Miler, in: Proceedings of the 8th International Seminar on Double-layer Capacitors and Similar Energy Storage Devices, 1998, pp. 7–9. Deerfield Beach.
[23] P. Sivaraman, S.P. Mishra, D.D. Potphode, A.P. Thakur, K. Shashidhara, A.B. Samui, A.R. Bhattacharyya, A supercapacitor based on longitudinal unzipping of multi-walled carbon nanotubes for high temperature application, RSC Adv. 5 (2015) 83546–83557, https://doi.org/10.1039/C5RA13136G.
[24] B. Batalla García, A.M. Feaver, Q. Zhang, R.D. Champion, G. Cao, T.T. Fister,

K.P. Nagle, G.T. Seidler, Effect of pore morphology on the electrochemical properties of electric double layer carbon cryogel supercapacitors, J. Appl. Phys. 104 (2008) 1–9, https://doi.org/10.1063/1.2949263.
[25] R. Farma, M. Deraman, I.A. Talib, R. Omar, J.G. Manjunatha, M.M. Ishak, Physical and electrochemical properties of supercapacitor electrodes derived from carbon nanotube and biomass carbon, Int. J. Electrochem. Sci. 8 (2013) 257–273.
[26] P.A. Basnayaka, M.K. Ram, L. Stefanakos, A. Kumar, Graphene/polypyrrole nanocomposite as electrochemical supercapacitor electrode: electrochemical impedance studies, Graphene 2 (2013) 81–87, https://doi.org/10.4236/graphene.2013.22012.
[27] K. Sheng, Y. Sun, C. Li, W. Yuan, G. Shi, Ultrahigh-rate supercapacitors based on eletrochemically reduced graphene oxide for ac line-filtering, Sci. Rep. 2 (2012) 3–7, https://doi.org/10.1038/srep00247.
[28] T.J. Freeborn, B. Maundy, A. Elwakil, Accurate time domain extraction of supercapacitor fractional-order model parameters, Proc. IEEE Int. Symp. Circ. Syst. (2013) 2259–2262, https://doi.org/10.1109/ISCAS.2013.6572327.
[29] A. Tepljakov, Fractional-order Calculus Based Identification and Control of Linear Dynamic Systems Master Thesis, TALLINN UNIVERSITY OF TECHNOLOGY, 2011. https://a-lab.ee/edu/theses/defended/52.
[30] T. Aleksei, Fractional-order Modeling and Control, 2016. http://fomcon.net/.

3.2. Paper #2: Capacitive study of a polystyrene nanoparticles capacitor using impedance spectroscopy.

This work is published in Nanotechnology. 30 (2019) 405702, doi:10.1088/1361-6528/ab2d58

IOP Publishing Journal Title
Journal **XX** (XXXX) XXXXXX https://doi.org/XXXX/XXXX

Capacitance study of a polystyrene nanoparticles capacitor using impedance spectroscopy

Bremnen Véliz[1,2], Albert Orpella[2] and Sandra Bermejo [2]

[1] Department of Electronic Engineering, GISCOR Group, Salesian Polytechnic University, Guayaquil, Ecuador
[2] Department of Electronic Engineering, MNT Group, Universitat Politécnica de Catalunya, Barcelona, Spain.

E-mail: Sandra.bermejo@upc.edu

Received xxxxxx
Accepted for publication xxxxxx
Published xxxxxx

Abstract

In this study, a metal-insulator-metal capacitor structure is fabricated using polystyrene-nanoparticles. Impedance spectroscopy is used to evaluate the performance of this capacitor in which we found out a significant magnitude increment in capacitance and loss tangent compared with an equivalent ideal capacitor with continuous polystyrene layer and same geometry. Capacitance values up to 11.7 and loss tangent values up to 387 (at 0.1Hz) larger than the expected for a continuous polystyrene MIM capacitor are achieved. The capacitor shows a good stable capacitive behavior in the frequency range from 0.1Hz to 100kHz at room temperature, 30°C, 40°C and 50°C without an effective relaxation process. Nyquist, capacitance, loss tangent and normalized powers curves are analysed by modified randles model. Also, it is observed a slight decrease in the capacitance value at 50°C that may be attributed to space charge localized at the nanoparticles interface and that are affected by the temperature changes.

Keywords: Polystyrene nanoparticles, metal-insulator-metal structure, impedance spectroscopy, electrospray, space charge polarization.

1. Introduction

The current trend to improve energy storage performance is driving to the characterization of different dielectric materials as metal oxides and polymers, as well as, the innovation in different structures at micro and nanoscale. Metal Insulator Metal (MIM) capacitors are used as a secondary power supply [1] in integrated circuits applications and are fabricated using planar and continuous films of high-k dielectrics as insulator layers. Nevertheless, 3D MIM nanostructures such as a nanoscale interdigital aluminum oxide membrane [2] or an nanotubular MIM [3] show an enhanced high density energy and high capacitance as 100μF/cm^2. Tree-dimensional nanocapacitors based on nanowires [4] or porous arrays [5] have achieved capacitances of about 10 and 2.5 times greater than for planar capacitor. Moreover, a new and simple fabrication method to self-assembly spherical nanoparticles using electrospray [6] has recently allowed the fabrication of a silica oxide nanoparticles MIM capacitor [7] which exhibited a capacitance 1000 times higher than an ordinary planar silica MIM capacitor.

On the other hand, polymers as dielectric materials are of distinctive interest for owning stable capacitances, low losses and high breakdown strengths; making them attractive in many energy store applications [8] such as film capacitors, gate dielectrics, fuel cells, organic photovoltaics, etc. For instance, the current state of art of polymer dielectric is based on biaxially oriented polypropylene (BOPP) [9] with loss tangent (tan δ) of about 0.0002 at 1khz, but modest dielectric permittivity of 2.2 and maximum operating temperature of 85°C. Recently, oligoaniline, a conductive material, was functionalized inside polystyrene film, and a dielectric constant increase around one order of magnitude was reported [10].

Polystyrene (PS) is a thermoplastic weak-polar polymer [11] constituted by large chain of styrene molecules. It owns

a dielectric permittivity of about 2.55 and a loss tangent of 0.0002 at glassy-state. Characteristics that make it a good alternative for manufacturing low cost insulators, or capacitors with low losses but low capacitance density. Also, polystyrene nanoparticles layers [12] have been successfully deposited with electrospray as a suitable alternative for giving rise to 3D colloidal structures as potential devices for nano-photonic applications such as photonic crystals [13] or inverse opals [14] [15].

Polystyrene impedance spectroscopy properties are mainly associated to two mechanisms of polarization [16] dependent on temperature: Dipolar polarization and space charge polarization. Dipolar polarization (also called Debye polarization) [17] is present till GHz frequencies and it is due to the thermal aligning of groups of proteins known as phenyl-groups [18] [19]. Space charge polarization [20] appears at metal-insulator interfaces or grain boundaries, and it is due to the diffusion of charge carries such as electrons, holes and ions.

In this paper, we report the fabrication and study of a new metal-insulator-metal capacitor structure using an array of polystyrene (PS) nanoparticles layers as insulator instead of a continue film of polystyrene. We enclosed the PS nanoparticles using electrospray and standard microelectronic fabrication techniques. Impedance spectroscopy data was measured and modelled at room temperature and at different temperatures below the glass-transition temperature. The improved capacitance and loss tangent were compared with a theoretical polystyrene film capacitor with the same planar area and thickness.

2. Experimental

2.1 Material and device fabrication

The device consists in two electrodes and some PS nanoparticles in between. The MIM capacitor was fabricated on a glass holder as a substrate, although any other thin or flexible holder could be used, reducing the cost and enhancing the feasibility. First, a photolithography step was performed to pattern a positive photoresist layer as it is shown in Figure 1a. Then a 355nm thick aluminum layer was deposited and then, the sacrificial photoresist layer was removed by a lift-off process thus creating the bottom plate electrode (20.25 mm^2) on the glass. A new layer of photoresist was spun-coated and patterned to create two cavities, one cavity for the MIM capacitor and the other for the contact with the bottom electrode.

In order to refill the first cavity with PS-nanoparticles (Figure 1b), the needle tip was placed at 6 cm from the sample and then a PS colloidal suspension was pumped at 0.3 mL/h. To form the Taylor cone [21], that is essential to electrospray the nanoparticles, a DC bias of +5.2 kV was applied at the needle and -2.1 kV at the bottom electrode. PS-nanoparticles are deposited by electrospray during 5 minutes onto the aluminum layer. The ambient temperature and ambient humidity were monitored at 26°C and 70% respectively.

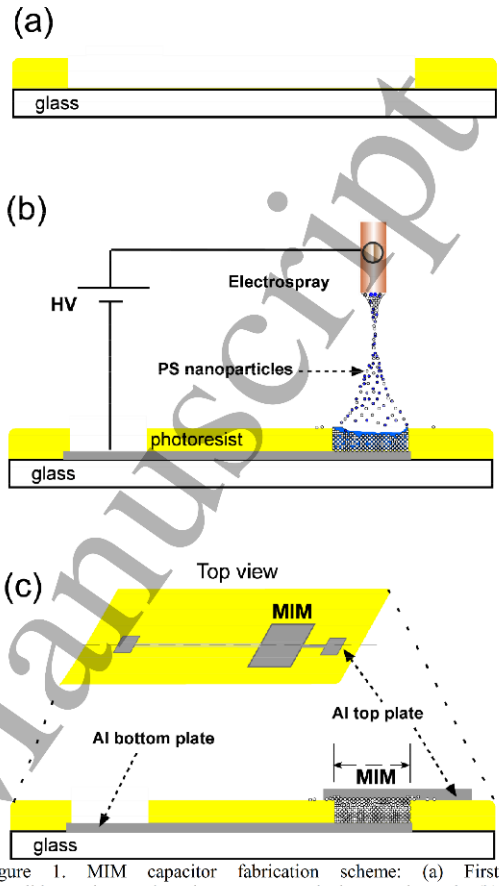

Figure 1. MIM capacitor fabrication scheme: (a) First photolithography step in order to construct the bottom electrode. (b) PS nanoparticles are electrosprayed with a high DC voltage between the needle and the bottom plate. (c) PS nanoparticles were covered by a thermal evaporated aluminium film as the top plate electrode.

The top plate electrode was also an aluminum layer but deposited by thermal evaporation onto the electrosprayed nanoparticles using a shadow mask to close the specific area of the MIM device with aluminum. A sectional top schematic of the device is shown in Figure 1c.

Regarding to the nanoparticles suspension, priory to the electrospray step, we modified the original monodisperse PS nanoparticles water suspension (295nm diameter and solid content weight 5%), mixing with propanol with a volume ratio of 6:4 respectively.

2.2 Characterization

Scanning Electron Microscope (SEM) and Focused Ion Beam (FIB) characterizations were used to obtain the top view and cross-sectional view of the resulting nanoparticle layers.

Electrical performance of the PS nanoparticle MIM capacitor was measured by impedance spectroscopy over the frequency range from 0.1 Hz to 100 kHz applying an excitation perturbation voltage amplitude of 500mV with an impedance analyzer (Hioki IM3590). The impedance measurements were first carried out at room temperature and a temperature sweep was also performed. The temperatures analysis was made using a thermal chuck with a STC200 temperature controller. In order to avoid deformation due to PS dilatation, the temperature range was maintained below the glass-transition-temperature [22]. Nyquist plot, capacitance values, loss tangent values and normalized power plots are presented.

2.3 Formulation

A MIM structure under an alternating electric voltage has an impedance Z(f) formed by a real and an imaginary component, that can be described as a complex capacitance.

$$Z(f) = Z' + jZ'' = 1/[j2\pi f C^*] \quad (1)$$

The complex capacitance C*(f) is defined by:

$$C^*(f) = [A/d]\epsilon^* = C' - jC'' \quad (2)$$

Where A is the planar area, d is the thickness and Є* is the complex permittivity.

The real capacitance C' is related to the energy storage, depends on the frequency and it is proportional to the permittivity Є'. This capacitance can be written as:

$$C' = -Z''/[2\pi f|Z|^2] = [A/d]\epsilon' \quad (3)$$

On the other hand, the loss tangent (or dielectric loss) is a dimensionless parameter defined as follows:

$$\tan(\delta) = |Z'/Z''| \quad (4)$$

Where δ is the loss angle. For an ideal capacitor tan δ = 0.

The complex power S can be defined as:

$$S = P + jQ \quad (5)$$

The normalized active power P_N and the normalized reactive power Q_N can be written as:

$$P_N = P/|S| = Z'/|Z| = \cos(\theta) \quad (6)$$
$$Q_N = Q/|S| = Z''/|Z| = sen(\theta) \quad (7)$$

Where θ is the phase angle of both the complex power S and the impedance Z(f).

In addition, a constant phase element [23] impedance can be defined by the equation:

$$Z_{CPE} = 1/[Q_C(j\omega)^{\alpha}] \quad (8)$$

Where α is a dispersion exponent that ranges between 0 to 1, Q_C is a coefficient that describes the ideal capacitance when α=1, and ω is the angular frequency.

Finally, a Warburg element [24] impedance Z_W can be defined by the equation:

$$Z_W = \frac{A_w}{\sqrt{\omega}}[1 - j] = \sqrt{2}A_w/[j\omega]^{1/2} \quad (9)$$

Where A_W is called Warburg coefficient.

3. Results and Discussion

3.1 SEM/FIB characterization

Figure 2a shows the SEM image of a top surface view of the PS-nanoparticles MIM capacitor. The orography is rough but regular in general terms, without peaks, holes or breakings. That is due to the mixture of the PS suspension with propanol favors the uniform scattering of the nanoparticles during the electrospray [12].

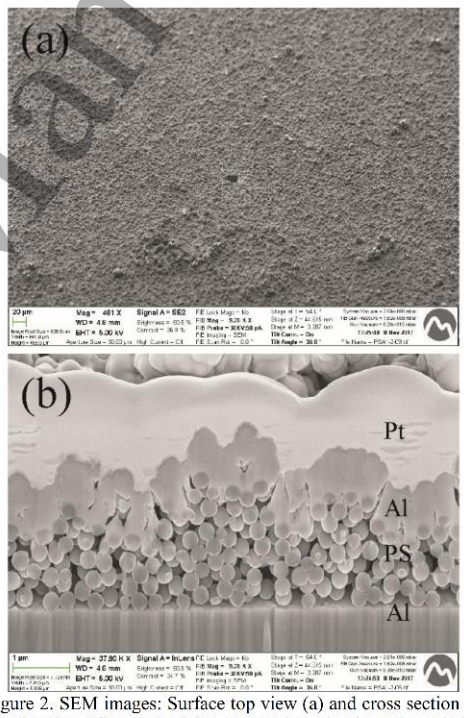

Figure 2. SEM images: Surface top view (a) and cross section view (b) showing PS nanoparticles arranged randomly and sandwiched between two aluminium layers.

Figure 2b shows a cross-section image drilled with FIB where the nanoparticles are sandwiched between the bottom and the top electrodes. A layer of platinum which was deposited with the scanning electron microscope to obtain a good image without electrostatic interference is also observed. As can be seen, the aluminum top electrode has an unevenness but smooth profile. This orography is not easy to control during the fabrication process and it makes difficult to calculate the effective contact area. However, we have estimated an averaged thickness of the PS layer of about 1.75 µm.

3.2 Impedance spectroscopy characterization at room temperature.

Figure 3a shows the Nyquist plot of the MIM capacitor at a room temperature of 21.5°C. High impedance values demonstrate a good insulation role of PS nanoparticles. The measured impedance data has been fitted with a modified randles spectral model which equivalent circuit consisted of four sub-circuits, that is shown in Figure 3c. The extracted circuit element values are shown in Table 1, where Q_{C1}, Q_{C2}, Q_{C3}, Q_{C4} are the coefficients of the four constant phase elements which represent no uniform accumulation of charges. Z_{W1} corresponds to a Warburg element that is related to a diffusion process; and R_2, R_3 and R_4 are shunt resistors.

We propose this model continuing with a previous work, where silicon oxide nanoparticles MIM capacitors [7] were analyzed using an equivalent circuit consisting of three sub-circuits that models the two contacts (top and bottom) and the SiO_2 nanoparticles. Since the top contact of the PS nanoparticles MIM is much rougher than SiO_2 nanoparticles MIM, the nanoparticles and the aluminum are contacted at different heights with respect to the bottom contact, which may suggest more than one resonance frequency. Therefore, we assume that the top contact can be represented by two sub-circuits in series. In addition, the bottom Al/PS contact is represented by a sub-circuit (Q_{C2} and R_2).

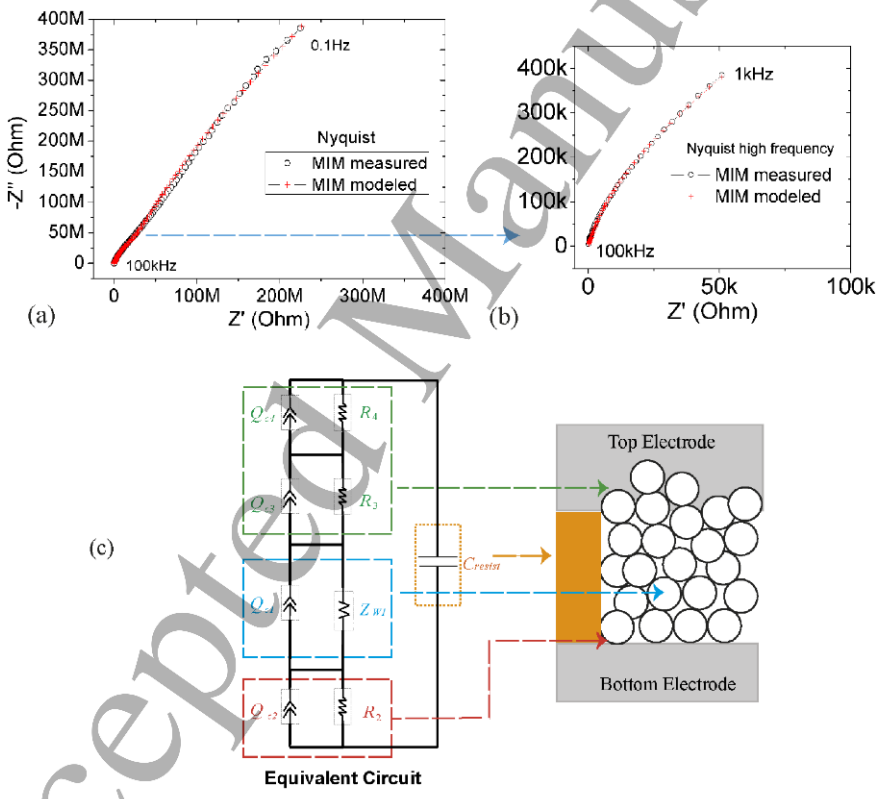

Figure 3. Nyquist plots (symbols: -o- data measured, -+- data fitted) at 500mVac and at room temperature: (a) Range frequency from 0.1Hz to 100kHz, (b) Range frequency from 1kHz to 100kHz. (c) Equivalent circuit used to fit the impedance data, where parallel sub-circuits represent the top PS/Al contact, the bottom PS/Al contact and the PS nanoparticles.

Table 1. Fitting parameter for the equivalent circuit of the PS nanoparticles MIM capacitor, s=jω

	Q_{C1}	α_1	A_{W1}	Q_{C2}	α_2	R_2	Q_{C3}	α_3	R_3	Q_{C4}	α_4	R_4	Cresist
Unit	$nFs^{\alpha-1}$		$M\Omega s^{1/2}$	$nFs^{\alpha-1}$		MΩ	$nFs^{\alpha-1}$		MΩ	$nFs^{\alpha-1}$		MΩ	pF
Value	1.55	0.97	390	2.2	0.93	22	1.4	0.99	1.5	2.5	1	0.10	33

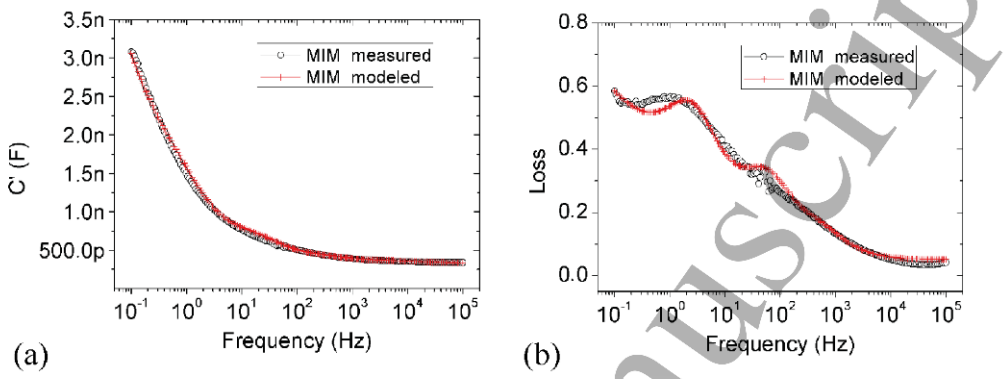

Figure 4. Experimental and modelled data (symbols: -o- and -+-) of capacitance (a) and loss tangent (b) at room temperature from 0.1Hz to 100kH

The four sub-circuits are overlapped in frequency, the resonant frequency of each sub-circuit is in the frequency range from 0.2Hz to 673Hz. These frequencies are so close that make it hard to identify the physical origin of each resonance process. Nevertheless, it seems that the sub-circuit that contains the Warburg impedance represents the nanoparticles because the diffusion is developed through the layers of nanoparticles and Q_{C1} is the result of complex mobile charges interacting with polystyrene and its free spaces, while the sub-circuits without Warburg are the MIM contacts. The top contact, where there is more contact area, is represented by the two sub-circuits whose resistances are the smallest. The second sub-circuit whose R_2 shunt resistance is the lager than R_3 or R_4 would be the bottom contact.

There is a capacitance due to photoresist localized in lateral area next to the MIM area. In order to consider the effect of photoresist, a separated Al/photoresist/Al MIM was fabricated and its capacitance was measured. Consequently, the photoresist in-between parallel plates capacitance in our polystyrene nanoparticle MIM is estimated as 33pF (C_{resist}).

As a result of the overlapping of the four resonant processes, the Nyquist plot exhibits a straight line (Figure 3a). We can say that the first sub-circuit dominates the region of lowest frequencies, the second one dominates low and intermediate regions, the third one dominates an intermediate region, while the fourth sub-circuit is prevalent for the highest frequencies. Moreover, the Warburg behavior is clearly predominant over the shunt resistors, which can be quantified by means of the ratio $A_{W1}/(R_2+R_3+R_4) \approx 16.53$ from Table 1. We found out that A_W has greater effect at low frequencies till around 2kHz. At high frequencies (>1kHz), the model also fits very well due to the other three sub-circuits. The three sub-circuits correspond to three depressed semicircles in the Nyquist plot, but due to the high Warburg coefficient, these semicircles are not observed in Figure 3b.

The parameters Q_C of the constant phase elements contribute to the capacitance C' that varies with frequency, whose maximum value is 3.1nF (at 0.1Hz) for the MIM. In order to investigate the frequency dispersion for the MIM including its modelling, capacitance C' and loss tangent curves defined by equations 3 and 4, are shown in Figure 4.

In Figure 4a, a significant decay is found in the capacitance in the range from 0.1Hz to 100Hz. This dispersion could be for a phenomena of formation of charge polarization on the nanoparticles surfaces. On the contrary, more stable frequency response is observed at frequencies from 100Hz to 100kHz. The whole capacitance of the PS layers with nanospheres and voids would be expected to be lower than a polystyrene film MIM capacitor of the same planar geometry. However, the measured capacitance is always higher, so the rate between the measured and theoretical capacitance is 11.7 at 0.1Hz whereas that at 1kHz the rate is 1.5.

Table 2. Comparison of capacitance and loss tangent: an expected theoretical PS film MIM capacitor with our novel PS nanoparticles MIM capacitor at room temperature.

	C'	Tan δ
Theoretical PS film MIM capacitor	0.26nF (1kHz)	$15x10^{-4}$ (1kHz)
Measured PS nanoparticles MIM capacitor	3.10nF (0.1Hz) 0.39nF(1kHz)	0.58 (0.1Hz) 0.13 (1kHz)

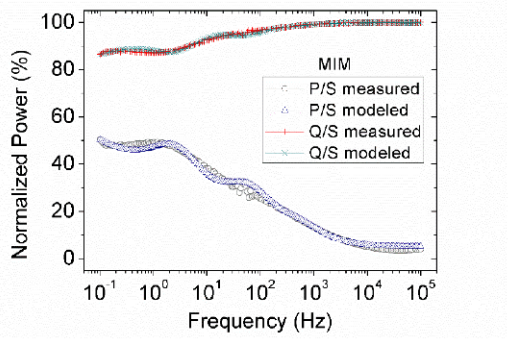

Figure 5. Experimental and modelled normalized powers where Q/|S|>P/|S|: (–○–) P/S is the measured normalized active power and (–Δ–) Q/S is the measured normalized reactive power. (–|–) P/S is the modeled active power and (–x–) Q/S is the modeled reactive power.

Table 2 shows the capacitance of an expected continuous PS film MIM capacitor compared to values of the PS nanoparticles MIM structure. We have calculated the theoretical capacitance value taking a planar area of 20.25mm^2, an average dielectric constant of 2.55 and an average thickness of 1.75 µm.

The increase in capacitance means a higher presence of charges in the nanoparticles MIM capacitor than in a conventional film MIM capacitor. We have already noticed a singular increase in capacitance with the silica nanoparticles [7] [25] in part associated to the humidity and its ions contribution, such as free hydrogens and hydroxyls groups moving on the silica surface. These charges arise from remnants of water molecules deposited by the electrospray phase. Therefore, we interpret that space charge polarization [20] is due to the free ions at the PS nanoparticles boundaries affecting positively to increase the capacitance specially at low frequency range. Nevertheless, as the frequency increases, ions cannot follow the electric field, the space charge polarization begins to disappear, and the weak dipolar polarization, the electronic and atomic polarization [26] that occur in the PS interior, remain.

As it can be seen in Figure 4b, loss tangent decreases with the frequency which is not usual in polystyrene film capacitors [27] [28]. Furthermore, loss values range from 0.58 to 0.035 meaning a stronger increment up to 387 times compared to the ordinary value found in the literature [11], as it is shown in Table 2. We believe that the boundaries between nanoparticles produce different conduction paths that are very resistive, causing more loss of energy than in a PS film MIM capacitor.

Normalized powers as a function of the frequency are observed in Figure 5. They have a perfect capacitive behaviour because reactive power is always higher than active power (Q/|S|>P/|S|) since there is not an effective relaxation process associated to a space charge relaxation. However, a relaxation point (where Q/|S|=P/|S|) could appear below the range of investigation. At high frequencies, the normalized powers are more separated, which means a better capacitive performance because the charges are stored with low loss energy.

Obviously, the cheminal nature of nanoparticle surface tends to allow the moving and orientation of surrounding ions and electrons that governing the electrical behavour. For instance, we noticed non stable capacitive behavours with silica nanoparticles MIMs reported in our former work. Paradoxically, capacities density of up to 2.63 µF/cm^2 were found at 0.1 Hz with silica nanoparticles. Meanwhile, capacitive density for the MIM of this work was 15.3 nF/cm^2. In spite of everything, the capacitance gain factor of this MIM is in the same order than nanocapacitors based on nanowires [4] (10 times greather than for planar capacitor).

3.3 Impedance spectroscopy at different temperatures

Temperature measurements have been performed at 30ºC, 40ºC and 50ºC. Table 3 shows the fitted parameters with the increase in temperature using the same circuit defined in Figure 3c.

As it can be seen in Figure 6a, a lineal behavior is kept at low frequencies exhibiting some noise as a consequence of the heating. In the range from 1kHz to 100kHz shown in Figure 6b, it is revealed that the curve tilts more toward the vertical axis as the temperature increases. This happen because Z' decreases and hence, the loss tangent also decreases at that frequencies range. For instance, the loss tangent is 0.13 at room temperature and at 1kHz as it can be observed in Table 2, while at 50°C (1kHz), the loss tangent changes to 0.058. The circuit model indicates that the reason of the Nyquist inclination is mainly due to the increase of the shunt resistor R_4. We assumed that this parameter belongs to the top contact.

All shunt resistors and the Warburg coefficient increase in value as the temperature increases. However, the increase in shunt resistances in proportion to the Warburg is a little higher, so the merit factor $A_{W1}/(R_2+R_3+R_4)$ always decreases with the temperature: 17.11 for 30°C, 15.76 for 40°C and 12.3 for 50°C. In our opinion, the charge concentration is reduced in the interface contacts due to the increase in temperature that produces a decrease in humidity, and therefore, an increase in the shunt resistors. In addition, the temperature increase produces also an increase in the Warburg impedance. We believe that the Warburg coefficient is following a similar behavior to the classic ions diffusion [29] in a solution because the coefficient has a direct relation with temperature.

On the other hand, the coefficients Q_{C1}, Q_{C2}, Q_{C3} and Q_{C4} showed a little decrease in their values as the temperature increases.

Moreover, a slight decrease in the capacitance associated with the merit factor can be predicted by looking at Figure 7, where we have plotted the ratio between the measured capacitance and the theoretical capacitance at 0.1Hz and 1Khz as a function of our merit factor. Similarly, since the space charges due to the moisture are evaporated, they can no longer contribute with more accumulation of charges. Consequently, the capacitance drops with temperature.

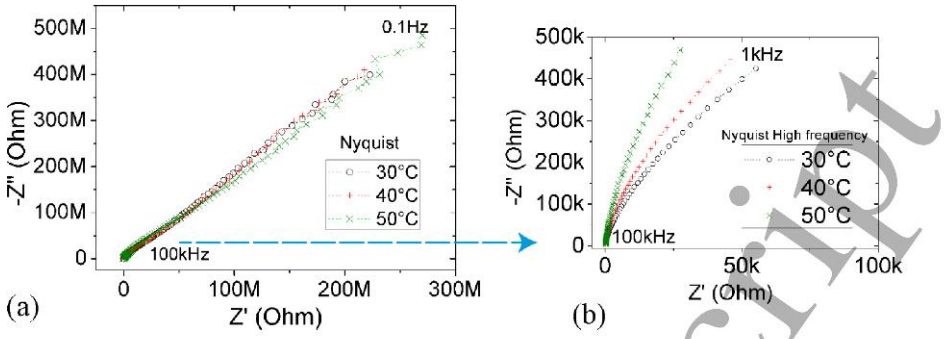

Figure 6. Nyquist plots at 30°C, 40°C and 50°C: (a) From 0.1Hz to 100kHz, exhibiting a lineal behaviour with some noise at low frequency. (b) Exhibiting a reduction Z' in the frequency range from 1 kHz to 100kHz.

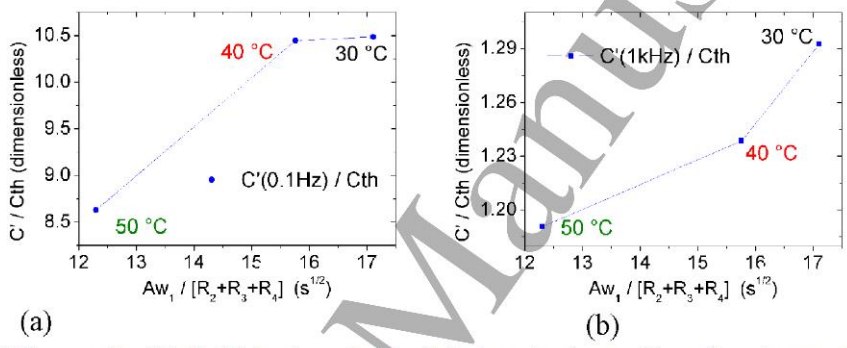

Figure 7. C' / C_{TH} versus Aw_1 / (R_2+R_3+R_4) showing a reduction with the temperature increase: (a) capacitance is measured at 0.1Hz, (b) capacitance is measured at 1kHz.

Table 3. Impedance spectroscopy parameters for the modelled polystyrene nanoparticle MIM capacitor at three different temperature T (°C).

T °C	Q_{C1} $nFs^{\alpha-1}$	α_1	A_{W1} $M\Omega^{s1/2}$	Q_{C2} $nFs^{\alpha-1}$	α_2	R_2 MΩ	Q_{C3} $nFs^{\alpha-1}$	α_3	R_3 MΩ	Q_{C4} $nFs^{\alpha-1}$	α_4	R_4 MΩ	C_{Resist} pF
30	1.60	0.97	410	2.0	0.94	22	1.3	1.0	1.8	1.9	1.0	0.16	33
40	1.60	0.97	430	1.8	0.94	25	1.3	1.0	2.0	1.8	1.0	0.29	33
50	1.40	0.97	500	1.7	0.96	35	1.1	1.0	5.0	1.8	1.0	0.65	33

Finally, we consider that dipolar polarization effect is negligible with the temperature variation, due to the nonpolar nature of the polystyrene molecules and because phenyl-groups are immobilized at temperatures below glass transition temperature either for polystyrene film (97°C to 107°C) or for PS nanoparticles (67.8 °C) [30].

4. Conclusions

A novel polystyrene (PS) MIM capacitor was fabricated using 295nm PS nanoparticles as insulator layer. Electrospray technique was used to deposit a 1.75 µm average thickness of nanoparticles film on an area of 20.25 mm^2. This device offered a higher capacitance (up to 11.7) and loss tangent (up to 387) values than the expected for an equivalent same dimensions MIM capacitor with a continuous PS film. This high capacitance is attributed in part to space charges localized at the nanoparticles interface.

Impedance spectroscopy was studied and modelled by a modified randles circuit consisting of four sub-circuits. The Nyquist plot revealed a straight line without effective relaxation points indicating a good capacitive behaviour.

The temperature study revealed a slight decrease in the capacitance in the whole frequency range as the temperature increase. Furthermore, an increment of the shunt resistances and the Warburg coefficient indicates that the deterioration of the metal contacts and the reduction of charge diffusion due to evaporation, are the main two facts that contributes to the reduction of the capacitance.

Given the higher presence of charges in the PS nanoparticles MIM capacitor than in a conventional film MIM capacitor, and the simplicity of the electrospray technique, we hope that this work will open up new possibilities for their application. The potential of this device can be explored using different type of dielectric material as insulator layer. In addition, the functionalization of the nanoparticles and the use of electrolytes electrochemically compatible with the surface of the nanoparticles can improve the overall performance of the device.

Acknowledgements

This work has been supported by the Spanish Ministry of Science and Innovation under projects TEC2014-59736-R, ESP2016-79612-C3-2-R. The activity was carried out under a programme of, and funded by the European Space Agency under project ESA AO/1-8876/17/NL/CRS. This work was also supported by SENESCYT of the republic of Ecuador. The authors thank Triffon Triffonov by the measurement performed at UPC CRNE.

References

[1] Mu J, Chou X, Ma Z, He J and Xiong J 2018 High-performance MIM capacitors for a secondary power supply application *Micromachines* **9** 1–10

[2] Han F, Meng G, Zhou F, Song L, Li X, Hu X, Zhu X, Wu B and Wei B 2015 Dielectric capacitors with three-dimensional nanoscale interdigital electrodes for energy storage *Sci. Adv.* **1** 1–7

[3] Banerjee P, Perez I, Henn-Lecordier L, Lee S B and Rubloff G W 2009 Nanotubular metal-insulator-metal capacitor arrays for energy storage *Nat. Nanotechnol.* **4** 292–6

[4] Wei L, Liu Q, Zhu B, Liu W, Ding S, Lu H, Jiang A and Zhang D W 2016 Low-Cost and High-Productivity Three-Dimensional Nanocapacitors Based on Stand-Up ZnO Nanowires for Energy Storage *Nanoscale Res. Lett.*

[5] Li L, Zhu B, Ding S, Lu H, Sun Q, Jiang A and Zhang D W 2012 Three-dimensional AlZnO / Al 2 O 3 / AlZnO nanocapacitor arrays on Si substrate for energy storage *Nanoscale Res. Lett.* **7** 1

[6] Coll A, Bermejo S and Castañer L 2014 Self-assembly of ordered silica nanostructures by electrospray *Microelectron. Eng.* **121** 68–71

[7] Véliz B, Bermejo S, Orpella A and Castañer L 2018 Impedance modeling of silica nanoparticle metal insulator metal capacitors *Electrochim. Acta* **280** 62–70

[8] Huan T D, Boggs S, Teyssedre G, Laurent C, Cakmak M, Kumar S and Ramprasad R 2016 Advanced polymeric dielectrics for high energy density applications *Prog. Mater. Sci.* **83** 236–69

[9] Treich G M, Tefferi M, Nasreen S, Mannodi-Kanakkithodi A, Li Z, Ramprasad R, Sotzing G A and Cao Y 2017 A rational co-design approach to the creation of new dielectric polymers with high energy density *IEEE Trans. Dielectr. Electr. Insul.* **24** 732–43

[10] Hardy C G, Islam M S, Gonzalez-Delozier D, Morgan J E, Cash B, Benicewicz B C, Plochn H J and Tang C 2013 Converting an electrical insulator into a dielectric capacitor: End-capping polystyrene with oligoaniline *Chem. Mater.* **25** 799–807

[11] Mark J E 1999 *Polymer Data Handbook* ed J E Mark (Oxford University Press)

[12] Coll A, Bermejo S, Hernández D and Castañer L 2013 Colloidal crystals by electrospraying polystyrene nanofluids *Nanoscale Res. Lett.* **8**

[13] John D. Joannopoulos, Steven G. Johnson, Joshua N. Winn R D M 2008 *Photonic Crystals Molding the Flow of Light* (New Jersey: Princeton University Press)

[14] Colvin V L 2001 From Opals to Optics: Colloidal Photonic Crystals *MRS Bull.* **26** 637–41

[15] Coll A, Bermejo S, Hernández D and Castañer L 2018 Al2O3/TiO2inverse opals from electrosprayed self-assembled templates *Beilstein J. Nanotechnol.* **9** 216–23

[16] Bibi F, Villain M, Guillaume C, Sorli B and Gontard N 2016 A Review: Origins of the Dielectric Properties of Proteins and Potential Development as Bio-Sensors *Sensors* **16** 1232

[17] Ahmad Z 2012 Polymer Dielectric Materials *Dielectric Material* ed M A Silaghi (Rijeka: InTech)

[18] Y.K.Kulshrestha; A.P. Srivastava; 1980 Dielectric properties of polystyrene and polystyrene-chloranil *Thin Solid Films* **71** 41–5

[19] McCammon R D, Saba R G and Work R N 1969 Dielectric properties of polystyrene and some polychlorostyrenes from 4°K to room temperature *J. Polym. Sci. Part A-2 Polym. Phys.* **7** 1721–33

[20] Baer E and Zhu L 2017 50th Anniversary Perspective: Dielectric Phenomena in Polymers and Multilayered Dielectric Films *Macromolecules* **50** 2239–56

[21] S. Wilm, Matthias; Mann M 1994 Electrospray and taylor cone theory dole's beam of macromolecules at last *Int. J. Mass Spectrom. Ion Process.* 167–80

[22] Rieger J 1996 The glass transition temperature of polystyrene *J. Therm. Anal.* **46** 965–72

[23] Jorcin J, Orazem M E, Nadine P and Tribollet B 2006 CPE analysis by local electrochemical impedance spectroscopy **51** 1473–9

[24] E. Barsoukov J R M 2005 *Impedance Spectroscopy: Theory, Experiment, and Applications* (John Wiley & Sons)

[25] Véliz B, Bermejo S, Coll A and Castañer L 2014 Metal-insulator-metal capacitor using electrosprayed nanoparticles *Appl. Phys. Lett.* **105**

[26] Vassilikou-Dova A and Kalogeras I M 2008 *Thermal Analysis of Polymers: Fundamentals and Applications* (John Wiley & Sons)

[27] P.K.C Pillai; and Rashmi 1980 Dielectric Properties of Polysrene and Some Related Polymers *Int. J. Polym. Mater. Polym. Biomater.* 255–63

[28] Electronics T 2007 Polystyrene Film & Foil 118–23

[29] J Brad, Allen & R Faulkner L 2000 *Electrochemical*

Methods: Fundamentals and Applications. (JOHN WILEY & SONS INC)

[30] Davodi B, Lashkenari M S and Eisazadeh H 2011 Fabrication and thermal degradation behavior of polystyrene nanoparticles coated with smooth polyaniline *Synth. Met.* **161** 1207–10

3.3. Paper #3: Large area deposition of ordered nanoparticle layers by electrospray.

This is published in Colloid and Interface Science Communications, Volume 25, 2018, Pages 16-21, https://doi.org/10.1016/j.colcom.2018.06.001.

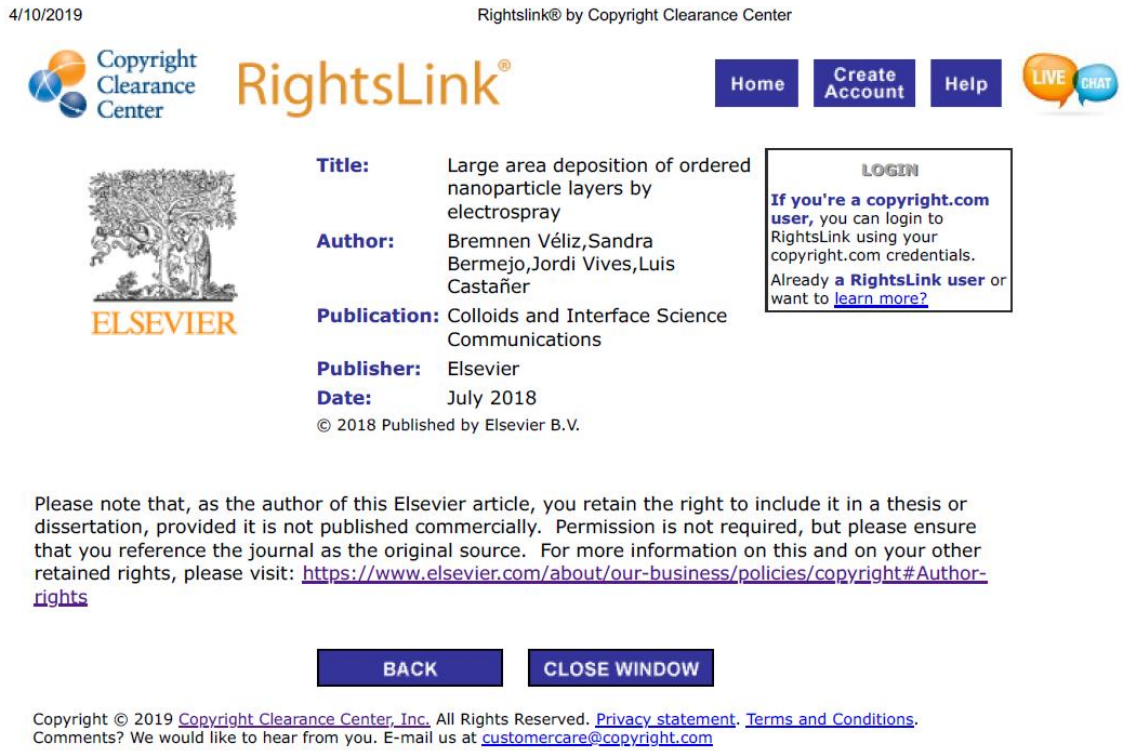

4/10/2019 Rightslink® by Copyright Clearance Center

Copyright Clearance Center RightsLink® Home Create Account Help LIVE CHAT

ELSEVIER

Title: Large area deposition of ordered nanoparticle layers by electrospray

Author: Bremnen Véliz,Sandra Bermejo,Jordi Vives,Luis Castañer

Publication: Colloids and Interface Science Communications

Publisher: Elsevier

Date: July 2018

© 2018 Published by Elsevier B.V.

LOGIN

If you're a copyright.com user, you can login to RightsLink using your copyright.com credentials.

Already a RightsLink user or want to learn more?

Please note that, as the author of this Elsevier article, you retain the right to include it in a thesis or dissertation, provided it is not published commercially. Permission is not required, but please ensure that you reference the journal as the original source. For more information on this and on your other retained rights, please visit: https://www.elsevier.com/about/our-business/policies/copyright#Author-rights

BACK CLOSE WINDOW

Copyright © 2019 Copyright Clearance Center, Inc. All Rights Reserved. Privacy statement. Terms and Conditions.
Comments? We would like to hear from you. E-mail us at customercare@copyright.com

Colloid and Interface Science Communications 25 (2018) 16–21

Contents lists available at ScienceDirect

Colloid and Interface Science Communications

journal homepage: www.elsevier.com/locate/colcom

Large area deposition of ordered nanoparticle layers by electrospray

Bremnen Véliz[a,b], Sandra Bermejo[a,*], Jordi Vives[a], Luis Castañer[a]

[a] Polytechnic University of Catalonia, Dept. of Electronic Engineering, MNT Group, Barcelona, Spain
[b] Salesian Polytechnic University, Dept. of Electronic Engineering, GISCOR Group, Guayaquil, Ecuador

ARTICLE INFO

Keywords:
Nanoparticles
Electrospray
Taylor cone
Polystyrene
Multineedle

ABSTRACT

Mass production of ordered nanostructures with enhanced optical properties such as colloidal crystals for applications such as solar cells or organic light emitted diodes demands low-cost and large-scale manufacturing techniques. In order to enlarge the deposition area of colloidal crystals, this paper presents the results of two different approaches that use the electrospray technique. Areas as large as 25 cm^2 have been achieved by using an array of needles, whereas up to 7.5 cm^2 areas were achieved by using an additional focusing electrode placed on the same plane as the needle nozzle. COMSOL simulations have been used as a guide for the set up design. The ordered deposition of the nanoparticles has been assessed by reflectance measurements and SEM/FIB observations.

1. Introduction

Electrospray has been widely used in mass spectrometry [1] [2] to identify chemical elements and cancer diagnosis [3]. In addition, due to its simplicity there has been a growing use of this technique for the manipulation of different types of nanoparticles in microelectronics [4] and photonics applications [5] [6] [7], given that it does not require vacuum conditions, it is a low cost, and inherently scalable technique, requiring significantly short deposit times.

Within the energy storage field for supercapacitors, electrospray technique has been successfully used to reduce the fabrication complexity of 3-D porous graphene [8] and carbon nanotubes electrodes [9] resulting in improved specific capacitances. Therefore, increasing the deposit area is crucial to reduce the cost of large-scale production in this industry. The supercapacitor global market reached USD 0.76 billion in 2017 and it is estimated to grow USD 2.25 billion by 2023 [10].

On the other hand, colloidal nanostructures have a wide variety of application for photonic devices [11] such as solar cells and displays, where periodic nanostructures enhance the interaction with photons. For instance, porous photonic structures using nanoparticles electrospray have demonstrated to improve light absorption in organic solar cells [12]. 2-D and 3-D colloidal crystals on silicon wafers are proved to be used as template to fabricate light trapping structures [13] known as inverse opals. Silicon nanowire solar cells have been built using 2-D colloidal crystals as etching mask for a DRIE process [14]. However, the area where the deposit has an ordered structure is usually small to cover the required area for commercial devices which is in the range of 60cm^2.

While a huge variety of self-organized colloidal structures fabrication techniques exist, electrospray has a good tradeoff between quality, deposit time, deposit area and number of monolayers. For instance, a simple technique is drop casting [15] [16] [17], where the colloidal dispersion is dropped on a horizontal surface substrate followed by a few hours slow drying of the dispersion (water). However, the obtained areas are of a few square centimeters, 3D structures are not too good and it is also necessary to have precise temperature and humidity control. Other known techniques are: Vertical Deposition [18], Langmuir-Blodgett [19], Shear Induced, Spin coating [20] [21], Wedge-cell [22], Dip-Coating [23], Temperature assisted Dip-Coating [24], and a hybrid method of spin coating and peeling draining [25]. Recently, a new method called Micro-Propulsive Injection [26] has shown a large area polystyrene (PS) structure of 1.7 m^2 with a manufacturing time of 4 h. However, only a monolayer structure can be self-assembled with this method. Fig. 1 shows a radial plot of some common self-assembly techniques described in [27] altogether with the ones presented in this work.

Previous works from our group have shown the feasibility of this technique for the fabrication of colloidal photonic crystals with polystyrene and silica nanoparticles [28] [29] and with a deposit area of 1 cm^2. Electrospray set-up uses a flow controlled syringe and a high voltage bias between the syringe needle and the substrate in order to guide the nanoparticles (which are suspended in a colloidal dispersion) toward the substrate. Not only capillary force [30], but electrostatic force [31] cause the self-assembly ordering of the resulting structures, so the electrical field must always be present during the deposition as well as the drying up.

* Corresponding author at: Micro and Nanotechnologies Group, c/. Jordi Girona 1-3, Campus Nord, 08034 Barcelona, Spain.
E-mail address: sandra.bermejo@upc.edu (S. Bermejo).

https://doi.org/10.1016/j.colcom.2018.06.001
Received 28 February 2018; Received in revised form 5 June 2018; Accepted 13 June 2018

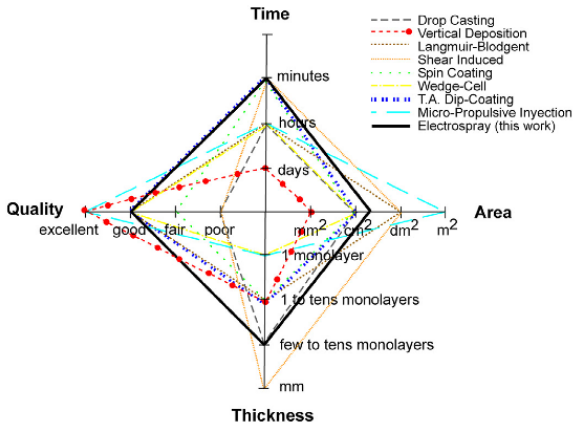

Fig. 1. Radial plot of common colloidal self-assembly methods. Four indicators are compared: Deposit time, area, thickness and quality.

The purpose of this work is to enlarge the deposit area while keeping the deposit time short and of high quality. As it can be seen in Fig. 1, the electrospray technique used in this work achieved a good quality deposit in minutes with areas of up to 25 cm^2. We have studied two modified electrospray methods; the first involves using a metallic guard ring polarized with a specific high voltage as simulations show that the resulting electric field widens the jet's dispersion, while the second method uses a four-needle matrix.

2. Experimental

The electrospray set-up was composed by a B.Braun infusion pump, a two channel Ultravolt high voltage DC source and a BD syringe containing 295 nm diameter polystyrene (PS) spherical nanoparticles in water dispersion (5% wt) supplied by Micro-particles GmbH. The nanoparticles dispersion had a pH = 7, which has been measured using a pH testing strip. The zeta-potential found in the literature [32] for polystyrene nanoparticles is around −36 mV. The metallic guard had an inner and outer diameter of 1.5 cm and 2.7 cm, respectively. In both set-ups, a stainless steel needle of 0.18 mm inner diameter and micro-tubes of 0.18 mm inner diameter were used to connect the needles, while an additional 1 mm inner diameter micro-tube was added to the four-needle setting in order to connect the syringe with a 5-way splitter implying a total distance traveled by the nanoparticle dispersion from the syringe to the needles approximately of 65 cm. For both set-ups, the positive terminal of the HV DC source was connected to the needles.

3. Results and discussion

Experiments lead to an increase in the area of about 7.5 cm^2 using one needle with a metallic guard, and 25 cm^2 using the four-needle matrix. In the first case the use of the guard ring with the appropriate voltage is responsible of the area increase whereas in the second case the increase of the number of sources covers a bigger area. Fig. 2 shows the images of both experimental arrangements. The substrate is a circular layer of aluminum previously deposited on a 4 in. silicon wafer.

The guard ring produced a dispersion of droplets resulting in an enlargement of the useful area. This happens due to the proximity of the ring to the needle, generating a strong potential gradient that achieves a bending jet with stable Taylor cone [33] [34], which in turn causes the droplets to be dispersed, but the pattern of dispersion was random as it left the center of the area as can see in Fig. 2.a. The short distance of both biased metals also caused an electrostatic buzzing, reason why this procedure was carefully carried out so as not to produce an electric discharge.

On the other hand, the four-needle approximation achieved four stable cone-jets in each needle for electrospray. The experimental stable conditions of the depositions are shown in Table.1, which includes the voltage of each channel from the HV source, the flow rate of the pumping machine, the distance between the needle(s) and the sample, deposition time (containing the time interval comprising all stable Taylor Cone's formation until the desired region is fully covered) and average drying time, which increases directly with the liquid quantity. The flow rate had to be increased up to 4 ml/h to feed four needles requiring a voltage of up to 13,500 V to control the higher flow bump. A picture of one of the four stable Taylor cones is shown Fig. 2.c.

Recently extensive research has been conducted [35] on the electrospray of DI water and depending on the value of the dimensionless α and β parameters, diverse regimes have been identified: straight jet, transition and whipping jet.

$$\alpha = \frac{\rho K Q}{\gamma \varepsilon_o \varepsilon'} \quad (1)$$

$$\beta = \frac{\sqrt{\varepsilon_O} V_a}{\sqrt{\gamma D}} \quad (2)$$

where ρ is density (Kg/m^3), K is electrical conductivity ($\Omega^{-1}\,m^{-1}$), Q is flow rate (m^3/s), γ is surface tension (Nm^{-1}), ε' is relative dielectric constant, V_a is applied voltage (V) and D is the inner diameter needle (m). In this work the experimental values were estimated for deionized water and corresponding to α = 0.65 and β = 11.2 (ρ = 1000Kg/m^3,$K = 1.2x10^{-4}\Omega^{-1}m^{-1}$,$Q = 2.78x10^{-10}m^3$/s, γ = 0.072$Nm^{-1}$,$\varepsilon' = 80.2$,$V_a = 13500V$) which would correspond to a Taylor cone jet mode of a straight-jet regime, but really close to micro-jet mode [35].

At the beginning and at the end of the experiment, small variations of the jets caused a no symmetric distribution of deposit by each needle. Surely, the water evaporation, the individual long capillary path and/or a micro-obstruction, caused that variation.

Despite the precise electrospray regime, this work concentrates in the deposition order and sample size of nanoparticle layers produced by this method concluding that the addition of bias ring and split of needles achieve larger areas of deposits.

We have also observed [28], differences when isopropanol is added to the dispersion to modify the parameters α and β, namely the forming of a cone-jet and pulverization. However, total 3D ordered nanoparticles are not achieved this way; instead the resulting structure is a disordered thin layer of nanoparticles. Although isopropanol has been used as solvent in electrospray ionization mass spectrometry to produce ion clusters [36], it has not been proved useful for our purpose.

COMSOL simulations— were performed for the two configurations in order to analyze the electric field lines, taking into consideration only the electrostatic behavior in vacuum. The distance from the needles to the substrate was set to 6 cm. Fig. 3a and Fig. 3b show the electric field lines for one needle with a metallic guard ring setting. The needle was biased at 6 kV, the guard ring at -3 kV and the sample substrate was grounded. A non-uniform distribution of electric field lines is expanded over the substrate, which will produce the desired nanoparticle dispersion. Alternative guard ring polarizations were analyzed, but led to unsatisfactory results, as the electric field lines diverged outside of the desired path.

Fig. 3c and Fig. 3d show the electric field pattern for the four-needle approach. The needles were biased at 6 kV and the substrate at -3 kV. The increase of the number of needles obviously increases the electric field lines density. Additionally, there is a higher electric field density in the sample's center. This distribution agrees perfectly with the density of nanoparticles observed in Fig. 1b, where the largest volume of deposited nanoparticles is in the center and decreases gradually towards the outside.

Scanning Electron Microscope (SEM) and Focused Ion Beam (FIB)

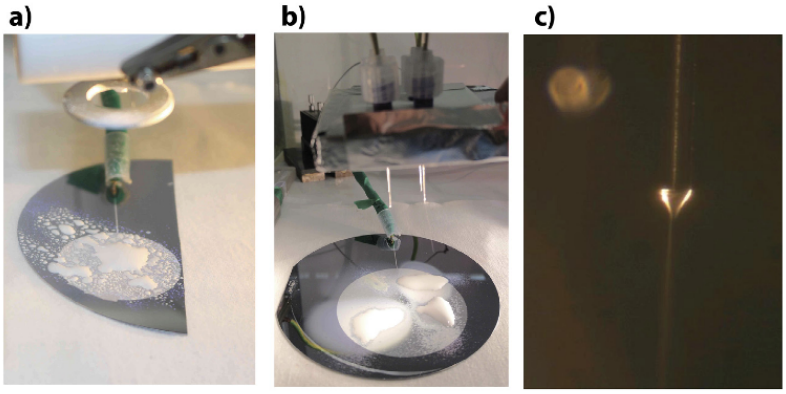

Fig. 2. Electrospray set-up: a) one needle with a metallic guard and liquid dispersion, b) 4-needle matrix and liquid dispersion, c) One of the four Taylor cones.

Table. 1
Experimental conditions in the electrospray depositions.

Electrospray System	Deposition conditions							
	Voltage	Current	Flow rate	RH	Distance	Deposition	Drying	Area
	[V]	[mA]	[ml/h]	[%]	[cm]	time [min]	time [min]	[cm^2]
1 needle with a metallic guard ring	+2850 −850	0.04	2	50	6	10	30	7.5
4-needle-matrix	10,000 −3500	0.04	4	40	7	15	40	25

Characterization— were performed to study how the nanospheres were distributed in detail, since the homogeneity and thickness of the deposition area. SEM pictures confirmed that the nanospheres formed an ordered structure as shown in Fig. 4.

Fig. 4a and Fig. 4b show that the sample's surface presents an ordered pattern, even though some minor dislocations can be observed in the deposit's surface. Also, we performed FIB measurements in order to see the 3D pattern in depth of the sample, as shown in Fig. 4c. We can observe a nanoparticle deposit of > 8 μm thick, which in turn means there are > 10 monolayers of 3D ordered structure. This structure forms a perfect colloidal crystal area. Fig. 4d, obtained by zooming out the join region between the needles, shows a dry drop with coffee stain effect. This is due to the close vicinity of the needles as the evaporation of colloidal structures drops leave behind ring-like solid residues, and it could also be caused by initial system instability. The presence dislocations and coffee stains are still limiting this method, producing loss of periodicity in the nanostructure.

Optical measurements— were made with a Shimadzu UV3600 UV-VIS-NIR spectrophotometer and are shown in Fig. 5. The reflectivity was measured three times in different random points on each sample substrate.

The reflectivity peaks are due to the ordered polystyrene (PS) nanostructure while the high reflectance values observed over all the wavelengths, are result of the presence of aluminum at the bottom, aluminum areas with few nanospheres are very reflective. Sample fabricated using the metallic guard ring arrangement shows a reflectivity peak at 700 nm. In the multiple needle case, the reflectivity peaks at 700 nm: with a reflectivity around of 85.3% for measurements on sample's central point (points 1 and 3) and great concentration of nanoparticles, and a peak of 91.4% and lower concentration (point 2).

This result is consistent with the theoretical wavelength region from 655.6 nm (λ_{min}) to 702.4 nm (λ_{max}) peaking at 679 nm (λ_P) carried out using the plane wave expansion method [37] for FCC structures and using the MIT Photonic Bands software [38].

Other authors use Bragg's law [39] [16] to approximate the reflection peak wavelength (λ_P). This law indicates that λ_P is directly proportional to the nanoparticle diameter D, and depends on an effective refractive index η_{eff} of the polystyrene/air combination and the incidence angle.

$$\lambda_P = 2\sqrt{\frac{2}{3}}.\, D.\, \sqrt{\eta_{eff}^2 - Sin^2\,\theta} \quad (3)$$

$$\eta_{eff} = \sqrt{(1-f).\,\eta_{air}^2 + f.\,\eta_{PS}^2} \quad (4)$$

where η_{AIR} is the refractive index of the air, η_{PS} is the refractive index of the PS, f is the sphere filling factor and θ is the incident angle. λ = 699.9 nm can be easily evaluated using the following values: D = 295 nm, θ = 8°, ƒ = 0.74 (for an ideal face centered cube lattice), η_{AIR} = 1 and η_{PS} = 1.59.

4. Conclusion

In this work, two different approaches for the enlargement of the deposited area of polystyrene nanoparticles forming colloidal crystals are shown. Both approaches are based on the tuning of an electrospray set-up: first by adding a metallic guard ring situated at the same height than the needle nozzle, and secondly by using a four-needle matrix. Theoretical values of dimensionless α and β parameters indicated electrospray as a straight-jet regime with a Taylor cone. SEM/FIM characterization showed that both approaches achieved good 3D ordered nanostructures and also optical measurement showed a stop band with peak reflectance at 700 nm as it was expected. In both cases a significant increase in the deposition area is achieved conversing the quality of the final structure. The guard ring approach achieves up to

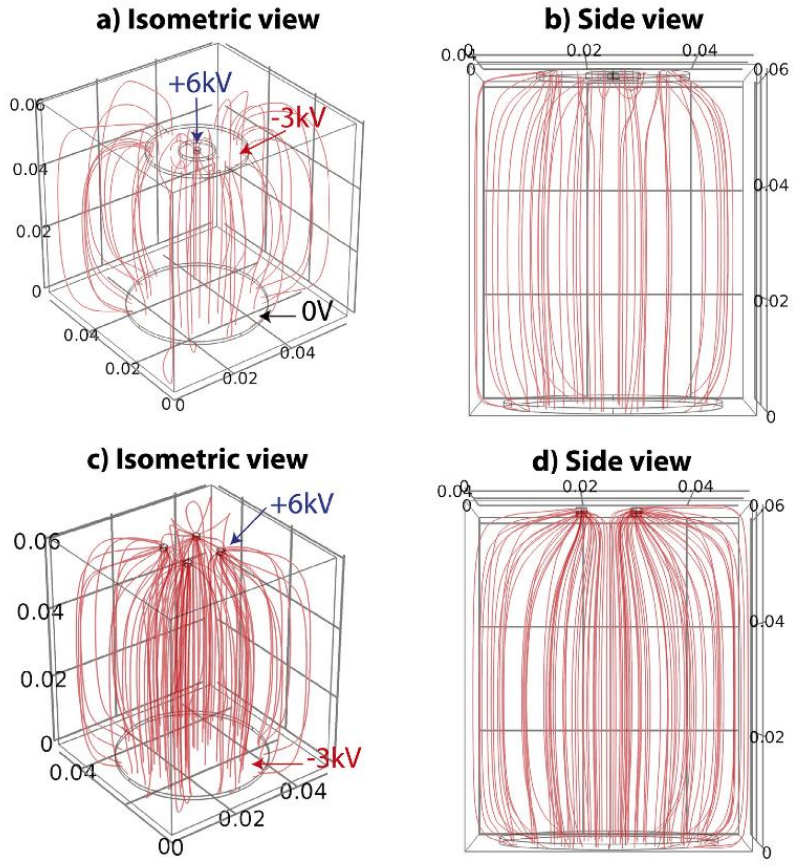

Fig. 3. Electric field lines: One single needle with a metallic guard ring, and Four-needle matrix. Isometric views are showed in (a) and (c); side views in (b) and (d).

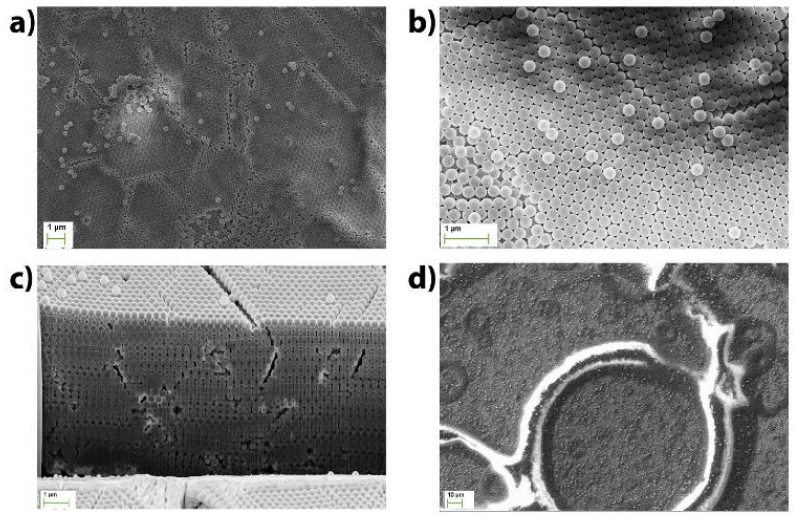

Fig. 4. SEM pictures of 295 nm diameter polystyrene nanoparticles deposit: a) and b) One needle with guard ring sample's surface, c) FIB performed on the four-needle matrix sample, d) Join region's drop on the four-needle matrix sample.

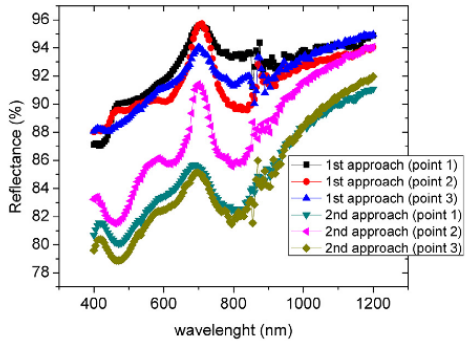

Fig. 5. Reflectance measurement: (■, ●, ▲) first approach of the guard ring, (▼, ◄, ♦) second approach of the four needle-matrix.

7.5 cm^2, while the four-needle approach obtained the desired area of 25 cm^2. Scaling-up the area of the deposit is crucial for the development of colloidal nanostructures that are able to cover larger surfaces, however, the presence of coffee stains on the join region between the needles is an issue that must be addressed in future steps.

Acknowledgement

This work has been supported by the Spanish Ministry of Science and Innovation under projects TEC2014-59736-R, ESP2016-79612-C3-2-R and by SENESCYT of the republic of Ecuador under agreement 2016-AR5G8871. The authors thank Triffon Triffonov by the measurement performed at CRNE and Gema Lopez with the support managing of the spectrophotometer.

References

[1] S.J. Gaskell, Electrospray: Principles and practice, J. Mass Spectrom. 32 (1997) 677–688, http://dx.doi.org/10.1002/(SICI)1096-9888(199707)32:7<677::AID-JMS536>3.0.CO;2-G.
[2] H. Cheng, X. Yan, R.N. Zare, Two New Devices for Identifying Electrochemical Reaction Intermediates with Desorption Electrospray Ionization Mass Spectrometry, Anal. Chem. 89 (2017) 3191–3198, http://dx.doi.org/10.1021/acs.analchem.6b05124.
[3] G.A.S. Shibdas Banerjee, Richard N. Zare, Robert J. Tibshirani, Christian A. Kunder, Rosalie Nolley, Richard Fan, James D. Brooks, Diagnosis of prostate cancer by desorption electrospray ionization mass spectrometric imaging of small metabolites and lipids, PNAS 114 (2017) 3334–3339, http://dx.doi.org/10.1073/pnas.1700677114.
[4] S. Khan, Y.H. Doh, A. Khan, A. Rahman, K.H. Choi, D.S. Kim, Direct patterning and electrospray deposition through EHD for fabrication of printed thin film transistors, Curr. Appl. Phys. 11 (2011) S271–S279, http://dx.doi.org/10.1016/j.cap.2010.11.044.
[5] S.-H. Hong, J.H. Moon, J.-M. Lim, S.-H. Kim, S.-M. Yang, Fabrication of spherical colloidal crystals using electrospray, Langmuir 21 (2005) 10416–10421, http://dx.doi.org/10.1021/la051266s.
[6] T. Kim, A. Canlier, G. Kim, J. Choi, M. Park, S. Min, J. Han, Electrostatic Spray Deposition of Highly Transparent Silver Nanowire Electrode on Flexible Substrate Electrostatic Spray Deposition of Highly Transparent Silver Nanowire Electrode on Flexible Substrate, ACS Appl. Mater. Interfaces 5 (2013) 788–794, http://dx.doi.org/10.1021/am3023543.
[7] S.N. Jayasinghe, Self-assembled nanostructures via electrospraying, Phys. E Low-Dimensional Syst. Nanostructures. 33 (2006) 398–406, http://dx.doi.org/10.1016/j.physe.2006.04.011.
[8] H. Tang, C. Yang, Z. Lin, Q. Yang, K. Feiju, C.P. Wong, Electrospray-deposition of graphene electrode: a simple technique to build high-performance supercapacitors, Nanoscale (2015), http://dx.doi.org/10.1039/C5NR00465A.
[9] A.P. Taylor, L.F. Velásquez-garcía, M. Donarelli, S. Prezioso, F. Perrozzi, A. Varea, O. Monereo, E. Xuriguera, J.D. Prades, Electrospray as a suitable technique for manufacturing carbon-based devices, J. Phys. D. Appl. Phys, https://doi.org/10.1088/1361-6463/aa798b, (2017).
[10] M. Intelligence, Super Capacitor Market - Segmented by type of capacitor (double layer, pseudo, hybrid), End-user Industry (aerospace & defense, utilities, industrial), and Region - Growth, Trends and Forecasts (2018–2023) (2018) 1 https://www.mordorintelligence.com/industry-reports/supercapacitor-market , Accessed date: 1 June 2018.
[11] J.Y. Chen, W.-L. Chang, C.K. Huang, K.W. Sun, Biomimetic nanostructured antireflection coating and its application on crystalline silicon solar cells, Opt. Express 19 (2011) 14411, http://dx.doi.org/10.1364/OE.19.014411.
[12] K.K. Khanum, J. Anakkavoor Krishnaswamy, P.C. Ramamurthy, Design and Fabrication of Photonic Structured Organic Solar Cells by Electrospraying, J. Phys. Chem. C 121 (2017) 8531–8540, http://dx.doi.org/10.1021/acs.jpcc.7b01698.
[13] E. Haugan, H. Granlund, J. Gjessing, E.S. Marstein, Colloidal Crystals as Templates for Light Harvesting Structures in Solar Cells, Energy Procedia 10 (2011) 292–296, http://dx.doi.org/10.1016/j.egypro.2011.10.193.
[14] E. Garnett, P. Yang, Light Trapping in Silicon Nanowire Solar Cells, Nano Lett. (2010) 1082–1087, http://dx.doi.org/10.1021/nl100161z.
[15] J. Zhou, Y. Zhou, S.L. Ng, H.X. Zhang, W.X. Que, Y.L. Lam, Y.C. Chan, C.H. Kam, Three-dimensional photonic band gap structure of a polymer-metal composite, Appl. Phys. Lett. 76 (2000) 3337, http://dx.doi.org/10.1063/1.126641.
[16] A. Yadav, R. De Angelis, M. Casalboni, F. De Matteis, P. Prosposito, F. Nanni, I. Cacciotti, Spectral properties of self-assembled polystyrene nanospheres photonic crystals doped with luminescent dyes, Opt. Mater. (Amst). 35 (2013) 1538–1543, http://dx.doi.org/10.1016/j.optmat.2013.03.020.
[17] E. Josten, E. Wetterskog, A. Glavic, P. Boesecke, A. Feoktystov, E. Brauweiler-Reuters, U. Rücker, G. Salazar-Alvarez, T. Brückel, L. Bergstrm, Superlattice growth and rearrangement during evaporation-induced nanoparticle self-assembly, Sci. Rep. 7 (2017) 1–9, http://dx.doi.org/10.1038/s41598-017-02121-4.
[18] P. Jiang, J.F. Bertone, K.S. Hwang, V.L. Colvin, Single-crystal colloidal multilayers of controlled thickness, Chem. Mater. 11 (1999) 2132–2140, http://dx.doi.org/10.1021/cm990080+.
[19] M. Szekeres, O. Kamalin, R.A. Schoonheydt, K. Wostyn, K. Clays, A. Persoons, I. Dékány, Ordering and optical properties of monolayers and multilayers of silica spheres deposited by the Langmuir–Blodgett method, J. Mater. Chem. 12 (2002) 3268–3274, http://dx.doi.org/10.1039/B204687C.
[20] S.S. Shinde, S. Park, Oriented colloidal-crystal thin films of polystyrene spheres via spin coating, J. Semicond. 36 (2015) 1–8, http://dx.doi.org/10.1088/1674-4926/36/2/023001.
[21] P. Jiang, M.J. McFarland, Large-scale fabrication of wafer-size colloidal crystals, macroporous polymers and nanocomposites by spin-coating, J. Am. Chem. Soc. 126 (2004) 13778–13786, http://dx.doi.org/10.1021/ja0470923.
[22] X. Chen, P. Li, H. Tong, T. Kako, J. Ye, Nanoarchitectonics of a Au nanoprism array on WO3film for synergistic optoelectronic response, Sci. Technol. Adv. Mater. 12 (2011), http://dx.doi.org/10.1088/1468-6996/12/4/044604.
[23] C. Deleuze, B. Sarrat, F. Ehrenfeld, S. Perquis, C. Derail, L. Billon, Photonic properties of hybrid colloidal crystals fabricated by a rapid dip-coating process, Phys. Chem. Chem. Phys. 13 (2011) 10681, http://dx.doi.org/10.1039/c0cp02517h.
[24] C. García Núñez, W.T. Navaraj, F. Liu, D. Shakthivel, R. Dahiya, Large-Area Self-Assembly of Silica Microspheres/Nanospheres by Temperature-Assisted Dip-Coating, ACS Appl. Mater. Interfaces. 0 (n.d.) doi:https://doi.org/10.1021/acsami.7b15178.
[25] Y. He, B. Zhu, X. Zeng, R. Yang, X. Lv, W. Yuan, Fabrication of large-area, close-packed, monolayer colloidal crystals via a hybrid method of spin coating and peeling–draining, Thin Solid Films 639 (2017) 98–106, http://dx.doi.org/10.1016/j.tsf.2017.08.035.
[26] P. Gao, J. He, S. Zhou, X. Yang, S. Li, J. Sheng, D. Wang, T. Yu, J. Ye, Y. Cui, Large-Area Nanosphere Self-Assembly by a Micro-Propulsive Injection Method for High Throughput Periodic Surface Nanotexturing, Nano Lett. 15 (2015) 4591–4598, http://dx.doi.org/10.1021/acs.nanolett.5b01202.
[27] J.F. Galisteo-Lôpez, M. Ibisate, R. Sapienza, L.S. Froufe-Pérez, Ú. Blanco, C. Lôpez, Self-assembled photonic structures, Adv. Mater. 23 (2011) 30–69, http://dx.doi.org/10.1002/adma.201000356.
[28] A. Coll, S. Bermejo, D. Hernández, L. Castañer, Colloidal crystals by electrospraying polystyrene nanofluids, Nanoscale Res. Lett. 8 (2013), http://dx.doi.org/10.1186/1556-276X-8-26.
[29] A. Coll, S. Bermejo, L. Castañer, Self-assembly of ordered silica nanostructures by electrospray, Microelectron. Eng. 121 (2014) 68–71, http://dx.doi.org/10.1016/j.mee.2014.03.031.
[30] P.A. Kralchevsky, N.D. Denkov, Capillary forces and structuring in layers of colloid particles, Curr. Opin. Colloid Interface Sci. 6 (2001) 383–401, http://dx.doi.org/10.1016/S1359-0294(01)00105-4.
[31] L. Castañer, S. Bermejo, M. Dominguez-Pumar, Effect of dielectrophoretic force in the self-assembly process of electrosprayed nanoparticles, J. Electrost. 87 (2017) 257–262, http://dx.doi.org/10.1016/j.elstat.2017.05.007.
[32] J. Dorney, Polystyrene : A Potential Standard for Developing In Vitro Cellular Tracking Methods for Nanotoxicology, Dublin Institute of Technology, 2013, http://dx.doi.org/10.21427/D75C76.
[33] Z. Zhou, X. Wu, X. Gao, L. Jiang, Y. Zhao, Parameter dependence of conic angle of nanofibres during electrospinning, 435401 (n.d.). doi:https://doi.org/10.1088/0022-3727/44/43/435401.
[34] D.H. Reneker, A.L. Yarin, H. Fong, S. Koombhongse, Bending instability of electrically charged liquid jets of polymer solutions in electrospinning Bending instability of electrically charged liquid jets of polymer solutions in electrospinning, 4531 (2013), http://dx.doi.org/10.1063/1.373532.
[35] I. Park, W.S. Hong, S.B. Kim, S.S. Kim, Experimental investigations on characteristics of stable water electrospray in air without discharge, Phys. Rev. E 95 (2017) 1–8, http://dx.doi.org/10.1103/PhysRevE.95.063110.
[36] N.B. Lentz, R.S. Houk, Negative Ion Mode Electrospray Ionization Mass

Spectrometry Study of Ammonium-Counter Ion Clusters, J. Am. Soc. Mass Spectrom. 18 (2007) 285–293, http://dx.doi.org/10.1016/j.jasms.2006.09.028.
[37] R.D.M. John, D. Joannopoulos, Steven G. Johnson, Joshua N. Winn, Photonic Crystals Molding the Flow of Light, Second, Princeton University Press, New Jersey, 2008.
[38] S.G. Johnson, J.D. Joannopoulos, Block-iterative frequency-domain methods for Maxwell ' s equations in a planewave basis, Opt. Express 8 (2001) 363–376 http://math.mit.edu/~stevenj/papers/JohnsonJo01.pdf.
[39] S. Schutzmann, I. Venditti, P. Prosposito, M. Casalboni, M.V. Russo, High-energy angle resolved reflection spectroscopy on three-dimensional photonic crystals of self-organized polymeric nanospheres, Opt. Express 16 (2008) 897, http://dx.doi.org/10.1364/OE.16.000897.

CHAPTER IV
Discussion

4.1. Electrospray deposition conditions of NP-MIMs.

Electrospray deposition method is a low cost, rapid and simple technique that can work at room temperature. Electrospray allows the targeting of the nanoparticles through a needle tip into the defined area (the MIM area) by means of a bias voltage between the needle and the substrate. An image of the electrospray set-up implemented in the electronic engineering department of the UPC North Campus is in appendix A. The parameters (Appendix A) for electrospray deposition include the colloidal suspension material, the applied voltage between terminals, the needle-substrate distances, the deposition time and the flow rate.

Modifying the electrospray deposition conditions, ordered and disordered nanostructures can be fabricated. Although, with particles larger than 255nm and under certain voltage conditions, it is likely to create ordered close-packed nanoparticles, many of the devices are composed by disordered arrays of nanoparticles. With regard to the deposition thickness, we experimentally have obtained structures from 1 to 30μm. There is a direct dependency on the flow rate and deposition time as the nanoparticles layer thickness increase.

When the deposition contains a high value of water contents the effect known as coffee stain (or coffee ring) may appear. This effect consists of the accumulation of nanoparticles that are transported to the edges by means of the evaporation gradient during the drying phase. The main problem with coffee stain is that on many occasions the top metal is cracked by nanoparticles deposited bellow.

To improve manufacturing repeatability, the original nanoparticles suspension (nanoparticles + deionized water) is mixed with isopropanol to decrease surface tension, reducing the water contents and thus having a shorter jet and Taylor cone. The result is

a structure of nanoparticles much more scattered and the elimination of coffee stains. Also linked to the modification of the suspension, the nanostructure surface roughness increases, in this case due to the fact that there is no water that left the nanoparticles at the same level as they dried.

The use of isopropanol also helps to avoid or diminish cracks in the deposition area. Keeping the NP MIM samples stored in a refrigerator while not in usage, also helps to diminish the possible cracks of the structures.

4.2. High capacitance of NP-MIM capacitors

Table 9 summarizes the areal capacitance, the capacitance gain, the electrode area, dielectric layer thickness, the specific capacitance and the deposited nanoparticles mass of the NP-MIM capacitors presented in the first two papers. The areal capacitance is the capacitance (C' derived from equation 6) divided by the area. The so noted capacitance gain refers to the rate between the measured capacitance respect to theoretical capacitance of a MIM with a continuous insulator layer of the same dimensions (in the papers it is denoted as C'/Cth). All devices have the active area of 20.25mm^2, except for the sample silica NP-MIM D that has 3.24mm^2. The measurements of the thicknesses are performed with a SEM/FIB microscopy installed at the UPC multiscale facility. Gravimetric capacitance is not presented in the papers, but it can be estimated by dividing the measured capacitance by the mass of the nanoparticles. The mass of the nanoparticles is estimated from the deposited nanoparticles volume and the density of the solid nanoparticle.

Silica and polystyrene NP-MIM capacitors showed a capacitance higher than the expected for the theoretical capacitance of an equivalent conventional MIM capacitor. For silica NP-MIMs, the specific capacitances (first paper) are 0.18, 0.28 and 2.63 µF/cm^2 (MIM A, MIM B and MIM C), that is 589, 449 and 1148 times larger than the theoretical capacitance. In contrast, the polystyrene NP-MIM capacitor exhibits a specific capacitance of 15.2nF/cm^2, and as we expected is higher than the theoretical film capacitance, but with a gain factor of 11.7.

Table 9. Summary of areal capacitance, gravimetric capacitance and capacitance gain of the reported NP-MIMs.

MIM capacitor	Areal Capacitance	Capacitance Gain [C'/Cth]	Area (mm^2)	Thickness (µm)	Gravimetric capacitance	Mass (µg)	Paper
Silica NP MIM-A	0.18 µF/cm^2	589	20.25	11.3	0.28 mF/g	124.7	#1
Silica NP-MIM-B	0.28 µF/cm^2	449	20.25	5.49	0.94 mF/g	60.57	#1
Silica NP MIM-C	2.63 µF/cm^2	1148	20.25	1.51	31.9 mF/g	16.67	#1
Silica NP MIM-D	0.91 µF/cm^2	268	3.24	1.01	16.5 mF/g	1.788	#1
Polystyrene NP MIM	15.3 nF/cm^2	11.7	20.25	1.75	0.28 mF/g	11.00	#2

The areal capacitances are in the order of the state of the art of integrated planar MIM capacitors (~µF/cm^2). This is amazing because the integrated MIMs have been developing for many years using high-k dielectric with thicknesses much smaller than the NP-MIM capacitors shown in this work, with a technology that is obviously not yet mature. Capacitance gains as high as 1000, makes them a good start point to use them as supercapacitors (SC). Nevertheless, the best areal capacitance value is 5703 times lower than activated carbon based electrodes which average value is about of 30mF/cm^2 (see Table 8 in the section 2.2). A SC assembled with two symmetry activated carbon based electrodes of 100F/g has 784 times more specific capacitance than the silica NP-MIM C. Of course it is too ambitious to believe that these early NP MIMs can compete with the current SCs. Although MIMs and SCs are electrostatic capacitors, only SCs use porous electrodes and an electrolyte. The NP-MIM capacitors use at the moment is deionized water as electrolyte, which is in fact a bad electrochemical conductor. In most fabricated NP-MIM, the maximum operating voltage is around 1.5V, higher than aqueous supercapacitors, which maximum voltage is about of 1V.

Regarding to the capacitance behaviour, we found out that the capacitance decreases when the frequency increases. To complement the mentioned, the capacitance dispersion log-log plot of our reported (paper #1 and paper #2) NP-MIM capacitors are shown in Figure 34. The largest capacitance is found for the thinnest NP-MIM. The thickness of the insulating nanoparticles layer is in brackets.

We propose that the high capacitance gain can be attributed to the interface polarization and to the humidity at the nanoparticles interstices and electrode interfaces. Therefore, electrons, hydrogens (H^+), hydroxyls (OH^-) and hydroniums (H_3O^+) moving around the periphery of the nanoparticles are the charge carries. Comparing the results of the fabricated NP-MIM samples, polystyrene NP-MIM capacitors have usually a lower capacitance or capacitance gain than silica NP-MIM. The explanation is most likely due to hydrophobic surface of the PS nanoparticles that contributes poorly to retain and transfer charges on the nanoparticles surface, whereas silica nanoparticles have the ability of attract charges from the environment.

As mentioned before, we suppose that the high capacitance gain can be attributed to the charge carries at the interstices brought by water molecules. In order to support our assumption, we proceeded to heat two specific built NP-MIM capacitors (silica NP-MIM D and polystyrene NP-MIM) till 50ºC. The effect of temperature increase is the decreasing in capacitance as it can be seen in Figure 35 and Figure 36. From our point of view, when the temperature increases, the interfacial adsorbed water concentration decreases, and thus the charge carries decrease. The reduction of the performance for both silica and polystyrene NP-MIMs also be observed in Figure 6 and Figure 7 embedded in the text of the paper #1 and paper #2 respectively.

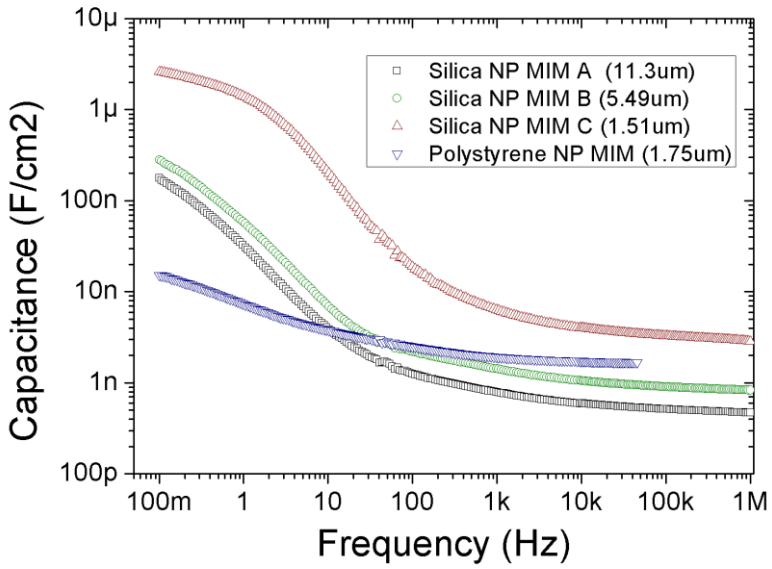

Figure 34. Capacitance behaviour of the NP MIM capacitors versus frequency at room temperature.

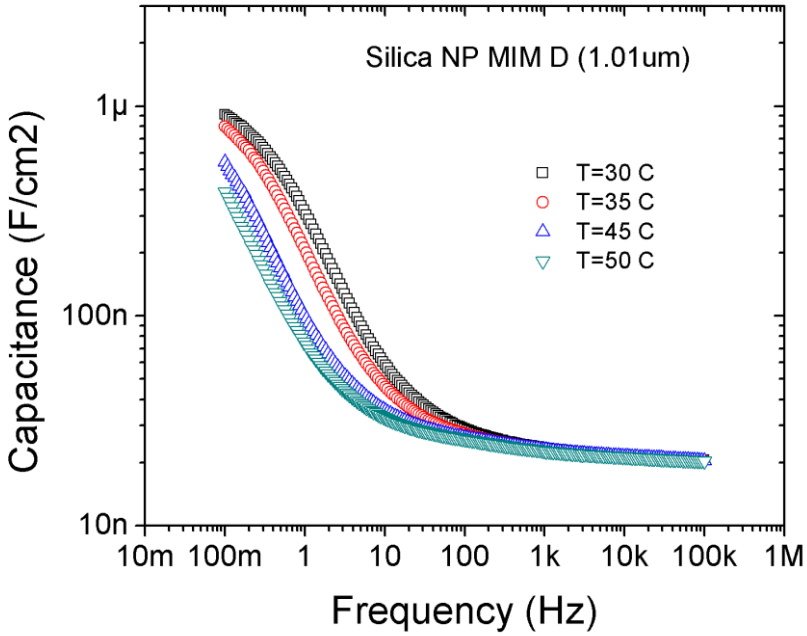

Figure 35. Capacitance versus frequency at different temperature for silica NP MIM D.

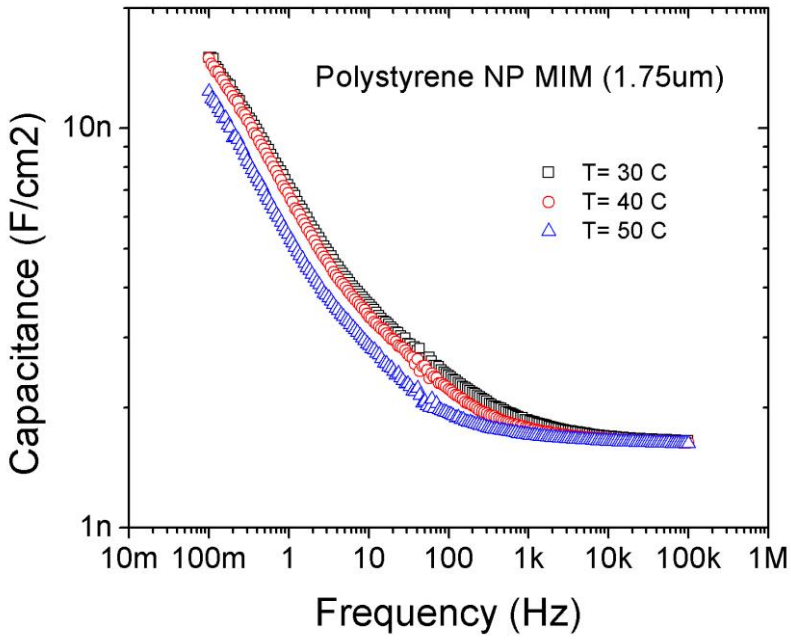

Figure 36. Capacitance versus frequency at different temperature for polystyrene NP MIM.

Furthermore, in order to know if the humidity effectively affects the NP-MIM behaviour (results not published yet), two more devices were fabricated (silica NP-MIM E and

polystyrene NP-MIM 2). The MIM area for both samples is 15.9mm^2, and the thicknesses are 3.11 µm and 5.4µm respectively. The capacitance of the NP-MIM capacitors under controlled conditions is measured using a climatic chamber (UPC south campus H9 electronic lab) at different relativity humidity values and at a constant temperature of 25ºC. As predicted the capacitance decreases when decreasing the relativity humidity as it is clearly shown in Figure 37 and Figure 38 (Appendix B), the maximum capacitance gains are 1760 and 9.41 at 90% RH for silica NP-MIM E and polystyrene NP-MIM 2 respectively. This corroborates the idea that the charges partially responsible for the capacitance enhancement are brought by water molecules at the nanoparticles surfaces.

In addition, in the case of silica nanostructures, the humidity also helps to increase the operating frequency range of the capacitive behaviour. As can be seen in Figure 43 for silica NP-MIM-E at 90% RH, the normalized reactive power is higher than the normalized active power up to the crossing point at 1.2kHz where both normalized powers match, that is, in all this frequency range the silica nanostructure behaves as a capacitor (Q/|S| > P/|S|), while above 1.2khz it has a resistive behaviour (P/|S| > Q/|S|). However, decreasing the humidity value up to 40% decreases the crossing point at 1.05Hz. In contrast, capacitive behaviour for the polystyrene NP -MIM-2 capacitor does not vary with humidity over the entire frequency range, as it can be seen in Figure 44.

4.3. NP-MIMs modelling.

The NP-MIM have been characterized by impedance spectroscopy measurements. The model used to the theoretical validation of the measurements is a modified Randle circuit formed by sub-circuits of distributed elements that are shown in Figure 5D (paper #1) for silica nanoparticles. The nanoparticles-metal interfaces are represented by sub-circuits of a CPE in parallel to a resistor, while the intermediate nanoparticles are modelled by a similar sub-circuit, but including a Warburg element in series with the resistor.

Each sub-circuits states for the physics of different parts of the NP-MIM: Since the nanoparticles have a higher contacting surface with the top metal than with the bottom metal, the top-interface resistance must be lower than the bottom-interface resistance. Therefore, the resistance of the top-metal/nanoparticles interface is R_3, whereas R_2 is the bottom-metal/nanoparticles interface ($R_3 < R_2$ as it can be observed in Table 2 in paper #1). On the other hand, the sub-circuit containing the Warburg element must be associated to the diffusion through the nanoparticles. Moreover, we believe that there is a greater

concentration of electric charges in the intermediate nanoparticles than in those located at the interfaces. Hence, this is reflected for the highest capacitance coefficient (Q_{CPE1}) of the central sub-circuit.

Different sub-circuits of the equivalent circuit can be recognized in the Nyquist plot. The depressed semicircle represents the metal-nanoparticle interface sub-circuits, while the inclined line is mainly associated to the intermediate nanoparticles sub-circuit. Figure 5 (paper #1) shows that the Nyquist plot for the silica NP-MIM C is more vertical than other silica NP-MIMs. The fitting revealed that it is because the magnitude of the Warburg impedance (Aw) is higher than the resistors (R_1, R_2, R_3) and due to the higher values of Q_{CPE1} compared to Q_{CPE2}, Q_{CPE3}.

In addition to the impedance spectroscopy characterization, we analyze the transient response of the NP-MIM capacitors. A silica NP-MIM capacitor is connected in series with a resistor, thus the response transient to a square signal is measured using a digital oscilloscope. These results matched very well with a Matlab simulation of the charge-discharge-transient response derived from the Laplace transform of the equivalent circuit. A detailed development of the impedance in the Laplace domain is shown in Annex C. In other words, the impedance spectroscopy equivalent circuit is again successfully verified.

The impedance spectroscopy equivalent circuit for the polystyrene NP MIM capacitor is also a modified Randles circuit, and the physical interpretation is the same as the defined for the silica NP MIM capacitors, but with two slight differences. First, the top interface is represented by two sub-circuits instead of one. The second sub-circuit appears may be explaining the higher value roughness, compared to the silica samples between the nanoparticles and the top-metal difference (Figure 2 in paper #2) between the nanoparticles and the top-metal are rougher than the top interface of the silica NP MIM capacitors. On the other hand, there is the inclusion of a parallel capacitance due to the photoresist that is laterally surrounding the NP MIM capacitor, as it can be observed in Figure 3 (paper #2). The photoresist in-between parallel plates capacitance in our polystyrene nanoparticle MIM is estimated as 33pF. This value affects very little because the CPE values are in the order of nF (Table 1 in paper #2), thus the photoresist can be neglected in the model.

The sub-circuit that contains the Warburg elements continues characterizing the nanoparticles. The Nyquist plot shows a very lineal shape which means a good capacitive behavior of the polystyrene NP MIM capacitor. The fitting reveals that the Warburg impedance is the impedance dominates at low frequencies and the highest value of the Warburg coefficient (Aw) compared to the resistors favors to the lineal form of the Nyquist plot.

The impedance spectroscopy modeling at different temperature reveals a slight reduction of the capacitive elements and the increase of the resistors as the temperature increase. The increase in temperature involves a reduction in humidity and in turn the loss of the carrier ions. The increase in the resistances is also an indicating of the deterioration of the metal contacts.

When comparing the temperature measurements of the PS and silica NP-MIMs, the effect of temperature is more important in the silica NP-MIM D capacitor than the polystyrene NP-MIM as can be observed in Nyquist plots (paper # 1 and paper #2). As the temperature increases, the semicircle increases for the silica NP-MIM D capacitor due to the increase of the interface resistances. Whereas the Nyquist plot of the polystyrene NP-MIM capacitor does not show any semicircle.

The same behavior is found for the silica NP-MIM E and polystyrene NP-MIM 2 (results not published yet) that are shown in Figure 41 and Figure 42 in appendix D. The measurements are taken at controlled environmental conditions for different humidity values show that the semicircle increases as the humidity decreases for the silica NP-MIM E. For the polystyrene NP-MIM 2, it is observed a shift towards the vertical axis of the lineal impedance, but without any semicircle. These last NP MIM capacitors are both modelled using the equivalent circuit showed in Figure 40 and fitted elements are shown in Table 11 and Table 12.

Summarizing the study at controlled humidity and temperature we can state for the silica NP-MIM capacitors that, as the temperature increases or the humidity decreases, the capacitance decreases, the interface resistors increases, the Q_{C1} and at least another Q_{Ci} decreases, the Warburg coefficient decreases, and the merit factor $A_W/(\sum R_i)$ decreases. The distributed elements behaviour for polystyrene MIMs is alike, but the main different is that the Warburg coefficient increases as the temperature increases or as the humidity decreases. In addition, the tendency of the merit factor to decrease does not continue as

humidity decreases. We can conclude that the Warburg impedance has a different behaviour because the diffusion of charges depends on the wettability of the nanoparticle surface. Silica surface is hydrophilic while polystyrene surface is hydrophobic. Therefore, these results have lead us to define the potential of the silica nanoparticles NP-MIM devices as humidity sensors.

4.5. Scaling-up of NP-MIMs deposition area by electrospray technique

Most of the large area deposition techniques of nanoparticles require of long process times and/or expensive equipment. Electrospray technology is a low cost easy-batch processed technique for the fabrication of NP-MIMs. The developed electrospray set-up has been tuned to produce the nanostructure on a large scale. In order to increase the deposition area of the nanoparticles structures, two electrospray approaches have been implemented and the resulting nanostructure morphology has been examined by SEM/FIB and ultraviolet-visible (UV-VIS) spectrophotometry characterization. For the tests of spherical polystyrene nanoparticles suspended in dezionized water in a solid dispersion of 5% are used. Order of the nanostructures are sought, as it may be necessary for many applications, constituting the worst scenario.

The first electrospray approach is the inclusion of a metallic ring placed at the same height as the tip needle. The metallic ring is polarized with a specific negative voltage, the needle at positive voltage and the sample at ground. The second approach was the split of the outgoing microchannel of the syringe, to make the simultaneous electrospray of a four-needle matrix.

It is possible to scale up the nanostructure deposition area using both approaches with forming of stable Taylor cones. The highest achieved area is 25cm^2 using the four-needle matrix, whereas 7.5 cm^2 is achieved using the metallic guard ring. The morphology of the structures shows a perfect three-dimensional order in all the area for both approaches, except for the joint regions on each of the four needles areas. The forming of coffee stains on the joint region is still observed, but it may be avoided by using isopropanol in the colloidal mixture.

Reflectance measurements carried out on the nanostructures show a forbidden band with a peak reflectance at a wavelength (λ_P) of 700nm due to the ordered polystyrene structure. The measured value is close to the theoretical value calculated by the Bragg law for colloidal crystals.

Scaling up the deposition area is crucial for the development of colloidal structures that are able to cover large surfaces. The results of the two electrospray approaches have been successful.

CHAPTER V

Conclusions and future works

Conclusions

Novel metal insulator metal (MIM) capacitors based on nanoparticles have been fabricated and intensively analysed by impedance spectroscopy characterisation. The structure of these nanoparticles metal insulator metal (NP-MIM) consists on building the insulator layer with arrays of nanoparticles, instead of conventional continuous layer used in MIM capacitors.

Monodispersed spherical nanoparticles of silica and polystyrene of 255nm and 295nm diameter respectively were used to create the insulator layers. Various devices with nanoparticles deposition areas of 3.24mm^2, 15.9mm^2 and 20.25mm^2 have been fabricated using the electrospray technique covering areas of up to 25cm^2.

The developed technology obtains very high capacitance values (up to 1148 higher capacitance than the equivalent capacitance for a conventional MIM structure), achieving the specific capacitance that are in the state of the art of the current MIM capacitors with high-k dielectrics, much smaller thicknesses and/or three dimensional structures. However, the specific capacitance is still low compared to supercapacitors.

The silica NP-MIM capacitors showed specific capacitances up to 2.63µF/cm^2 and a gravimetric capacitance of 31.9mF/g for a nanoparticles layer thickness of 1.5µm, corresponding to a capacitance value 1148 times higher than the theoretical capacitance of an equivalent capacitor with a continuous dielectric layer.

The polystyrene NP-MIM capacitor showed a specific capacitance up to 15.3nF/cm^2 and a gravimetric capacitance of 0.28mF/g with a layer thickness of 1.75um. The corresponding capacitance value was 11.7 times higher than the theoretical capacitance of an equivalent capacitor with a continuous dielectric layer. Difference between polystyrene and silica NP-MIM may be attributed to the hydrophobic and hydrophilic behaviour of both materials, respectively.

The enhanced capacitance values may be attributed to carriers as hydrogens (H^+), hydroxyls (OH^-) and hydroniums (H_3O^+) ions in the nanoparticle interfaces due to water molecules adsorbed from the electrospray remnant and the ambient humidity. Then, the hydrophobic/hydrophilic characteristic of the materials may play a definite role.

Models consisting on modified Randle circuits have been performed fitting the impedance spectroscopy measurements. The models define the physical behaviour of each of the NP-MIM parts: the nanoparticles-metal interfaces are physically represented by a sub-circuit that consists on the parallel of a constant phase element to a resistor, whereas the inner nanoparticles are represented by a similar sub-circuit, but including a Warburg element in series with the resistor.

As mentioned before, the enhanced capacitance values may be attributed to carriers in the nanoparticle interfaces due to water molecules. Measurements at different temperature and relative humidity clearly show an increase in capacitance with the reduction in temperature or with the increase in humidity, confirming the relation of the capacitance values with the water molecules contents.

The modelling also revealed that the contact interface resistances increases as temperature increases or as the humidity decreases, showing that the conductivity is reduced. On the other hand, warburg coefficient increases as the humidity increases or when the temperature decreases for silica NP-MIM capacitor, whereas Warburg coefficient decreases for the polystyrene NP-MIM capacitor. Therefore, the conclusion may be that the attraction and diffusion defined by the Warburg coefficient depends on the chemical nature of these nanoparticles, so, as concluded before, the hydrophobicity and hydrophilicity of the surface is playing an important role.

As a summary, the fabricated NP-MIMs have been shown as a good template for promising new coming energy sources. The current NP-MIM capacitor technology is working at 1.5V, with an energy density of 10mWh/Kg and a power density of 563kW/kg. The inclusion of specific electrolytes and change of the electrode metals may overcome the voltage challenge and increase the operating voltage. In any case, the findings in the fabrication, characterization and physical interpretation made in this thesis have defined a starting point in the development of a new MIM capacitor concept as a promising energy storage device, expanding the perspective of the MIM capacitors.

Future works

In the near and medium term, there are many new works to do. Some of them will be a natural continuation of the started work in this thesis. Other nanosphere materials may be used, as titanium oxide (TiO_2) and alumina (Al_2O_3). The attention to these materials must be addressed because they are high-k dielectrics materials.

In order to understand the conduction mechanisms of NP-MIM capacitors, the leakage current density characterization under constant voltage stresses at different temperature must be carried out.

Since in the fabrication process there are sometimes ruptures or lift-off of the nanoparticles structure, a small percentage of binder can be added to the colloidal suspensions in order to keep the nanoparticles together in the insulator structure. This is a similar approach to the one used in carbon electrodes in supercapacitors.

Adding ionogel electrolytes to the nanostructure will potentially provide electrochemical charge to the nanoparticles. Some of these ionogelmay 1-butyl-3-methylimidazolium bis-trifluoromethylsulfonylimide ([BMI][TFSI]) and lithium trifluoromethanesulfonate (LiTFSI), among others. Based on the supercapacitor reported studies, it would be expected an increase in the capacitance, operating voltage and stable mechanical strength.

The NP-MIM fabrication technology allows to include an inverse opal structure. Therefore, dielectric or carbon based shell structures filled with electrolytes may be introduced in the NP-MIM device, mimicking some of the existing supercapacitor technologies and joining the NP-MIM strengths to the supercapacitor concept.

Finally, the high charge sensitivity of the silica NP-MIM has to be analyzed as a potential humidity sensor.

Appendices

Appendix A
Electrospray and nanoparticles specifications

The electrospray system used in this thesis is composed of the following parts:

i. A glove box.

ii. An infusion pump: B Braun perfusor-space, 0.01-999.9mL/h.

iii. A bipolar high voltage DC power supply: Ultravolt, 30W, ±15 kV.

iv. A digital camera: DCC1645C-HQ with Optem zoom 125

v. Microfluidic components: a 3ml plastic pack syringe, a micro-tube (P-1531), a Luer adapter (UP-P-658), LuerTight fitting (P-837), flangeless fittings (XP-202X), a dispensing needle (stainless steel, 30 gauge, 25mm length), and needle support.

Figure 37. Electrospray system mounted in the UPC facilities.

According to the manufacture data sheet, the main specifications of the silica and polystyrene colloidal suspensions are:

Table 9. Specifications of colloidal suspension taken from micro-particles GmbH

Nanoparticle material	Concentration	Size	Classification	Colour	Odour	Density (solid NP)	Melting point
Silica	Monodisperse silica particles: 5% Deionized water: 95%	255nm	Not a hazardous substance	White aqueous suspension	Odourless	1.85g/cm^3 (20ºC)	>1000ºC
Polystyrene	Monodisperse polystyrene particles: 5% Deionized water: 95%	295nm	Not a hazardous substance	White aqueous suspension	Odourless	1.05g/cm^3 (20ºC)	74-105ºC

Experimental conditions of the nanoparticles deposition by electrospray for the fabrication of NP MIM capacitors are shown in Table 10.

Table 10. Summary of electrospray conditions used for the nanoparticle deposition in the NP MIM

Nanoparticle material	Prepared suspension	Electrospray applied Voltage	Needle to substrate distance	Deposition time	Pump flow rate	Electrospray mode
Silica	Original colloidal suspension	6.3-7.4kV	6-7cm	6-10 minutes	0.3-0.4 mL/h	Cone-jet
Polystyrene	60% original suspension + 40% propanol	7.3kV	6-7cm	5-6 minutes	0.3mL/h	Cone-jet

Appendix B.

Impedance spectroscopy of others NP-MIM capacitors at controlled environment conditions

Silica NP-MIM E and polystyrene NP-MIM 2 are fabricated with a round electrode area of 15.9mm^2. The experimental measurements in the 0.1Hz to 100kHz frequency range for different relative humidity, at a constant temperature of 25ºC are shown in Figure 38 for silica NP-MIM E capacitor. Figure 39 shows the measurements for the polystyrene NP-MIM 2 capacitor, in the frequency range from 1Hz to 100kHz. In both case, a sinusoidal signal 500mV was applied.

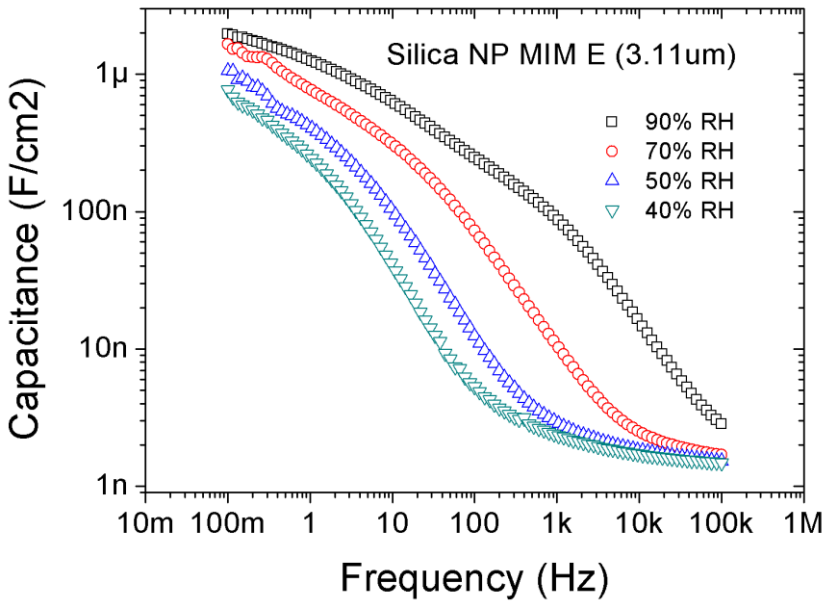

Figure 38. Capacitance versus frequency plot for the Silica NP-MIM E, at 25ºC, for different Relative Humidity (RH) values.

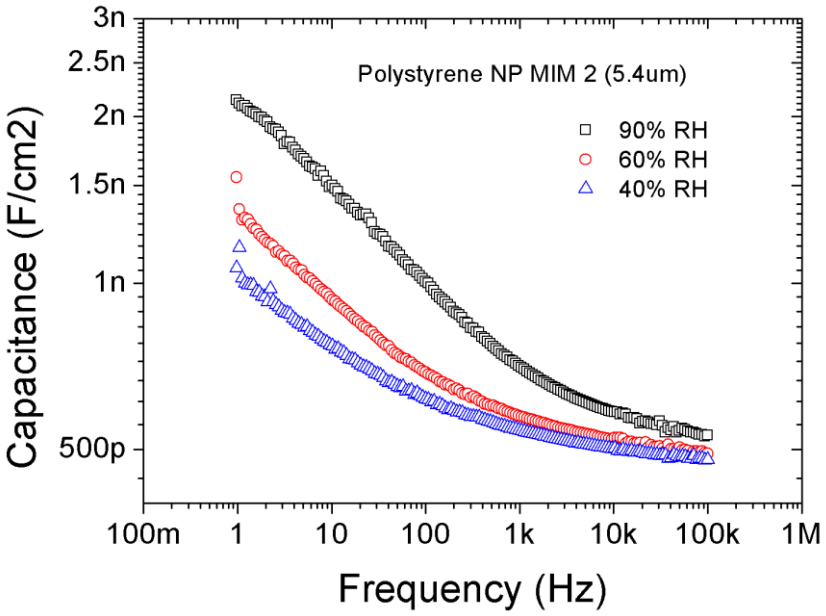

Figure 39. Capacitance versus frequency plot for the Polystyrene NP-MIM 2, at 25ºC, for different Relative Humidity (RH) values.

Nyquist plots at different relative humidity, at a constant temperature of 25ºC for silica and polystyrene NP MIM capacitors are shown Figure 41 and Figure 42. The measurements have been fitted with an equivalent circuit model showed in Figure 40.

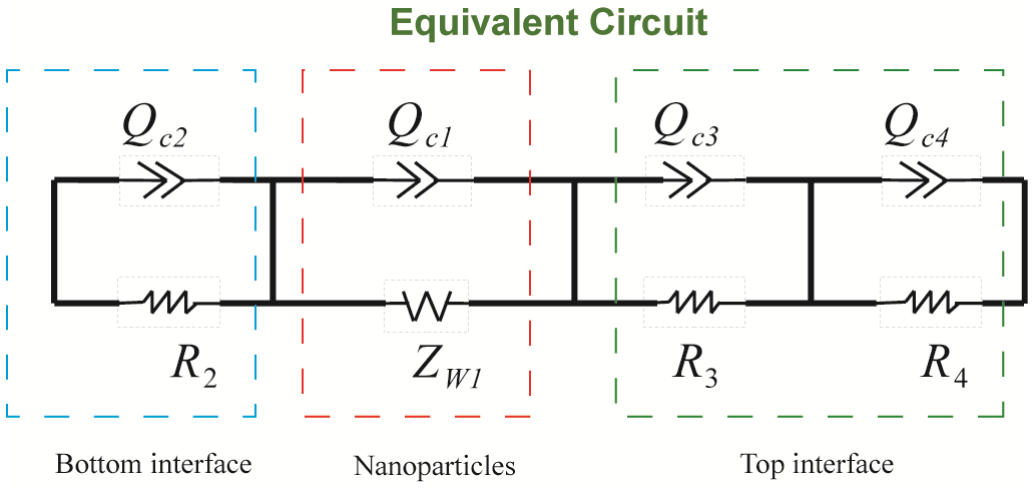

Figure 40. Modified Randles circuit used to model silica NP-MIM E and polystyrene NP-MIM 2.

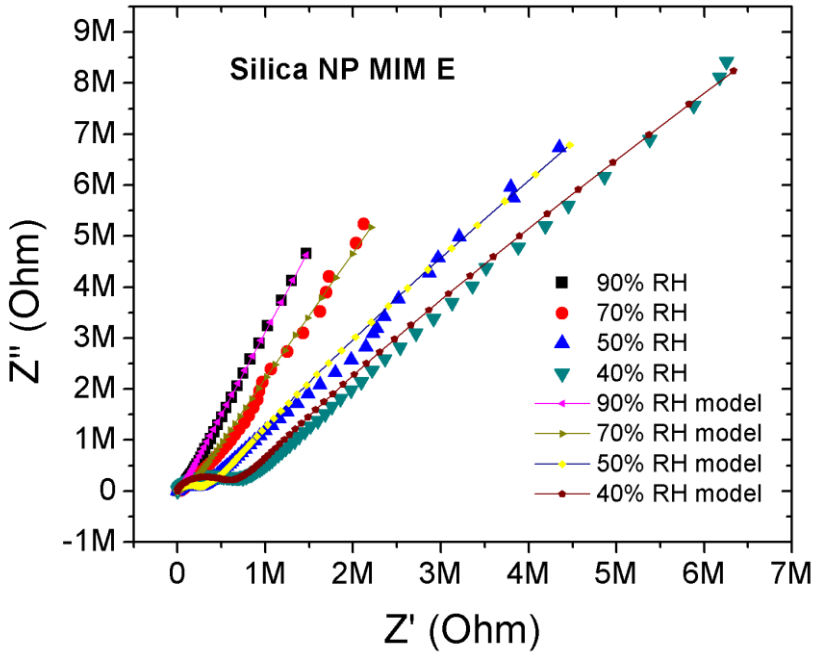

Figure 41. Nyquist plot measured for silica NP-MIM E at different relatively humidity and a temperature of 25°C. The frequency scan starts at 0.1Hz.

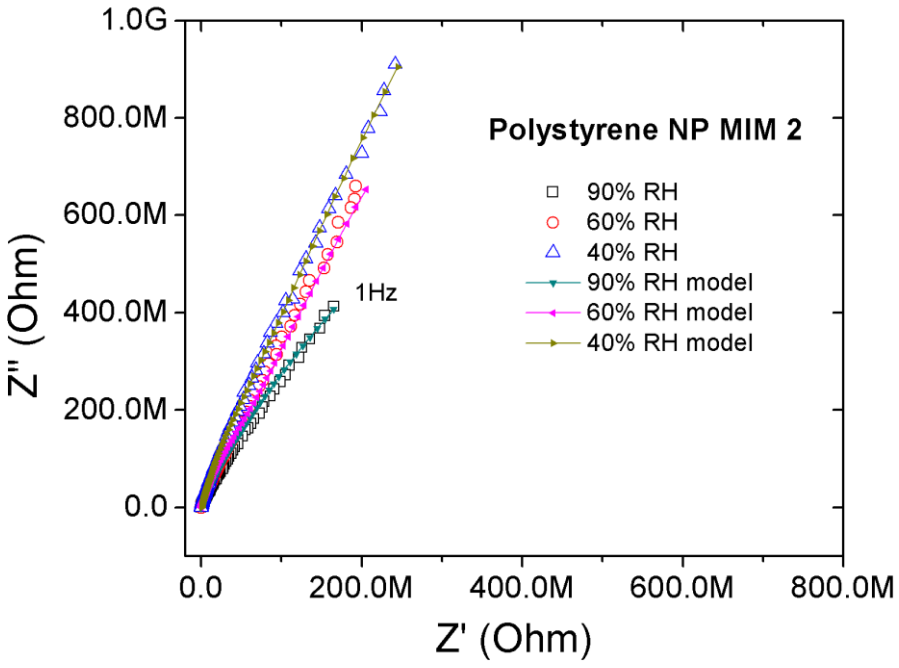

Figure 42. Nyquist plot measured for polystyrene NP-MIM 2 at different relative humidity and a temperature of 25°C. The frequency scan starts at 1Hz.

Table 11. Fitting elements for the silica NP-MIM E capacitor at 90%RH, 70%RH, 50%RH and 40%RH.

RH	Q_{C1}	A_W	α_1	Q_{C2}	R_2	α_2	Q_{C3}	R_3	α_3	Q_{C4}	R_4	α_4
%	$nFs^{\alpha-1}$	$M\Omega s^{\alpha-0.5}$		$nFs^{\alpha-1}$	kΩ		$nFs^{\alpha-1}$	kΩ		$nFs^{\alpha-1}$	kΩ	
90	300	700	0.81	120	30	0.91	1.4	2.2	0.90	90	4	0.82
70	240	40	0.78	180	100	0.88	1.4	22	0.90	40	23	0.80
50	100	8.6	0.81	100	200	0.88	0.9	230	0.92	40	58	0.82
40	57	8.6	0.82	100	200	0.88	0.9	520	0.92	40	88	0.82

Table 12. Fitting elements for the polystyrene NP-MIM 2 capacitor at 90%RH, 60%RH and 40%RH.

RH	Q_{C1}	A_W	α_1	Q_{C2}	R_2	α_2	Q_{C3}	R_3	α_3	Q_{C4}	R_4	α_4
%	$pFs^{\alpha-1}$	$G\Omega s^{\alpha-0.5}$		$nFs^{\alpha-1}$	MΩ		$nFs^{\alpha-1}$	kΩ		$pFs^{\alpha-1}$	MΩ	
90	232	1.6	0.98	1.9	8	0.98	0.9	40	0.96	300	2.4	1
60	200	4.1	0.97	0.7	45	0.98	2.0	50	0.96	400	4.5	1
40	150	6.4	0.97	0.8	45	0.98	20.0	50	0.96	700	4.5	1

Normalized powers plot shows the capacitive behaviour of the nanoparticles capacitors as a function on the frequency for different relative humidity (RH) and at an ambient temperature of 25ºC.

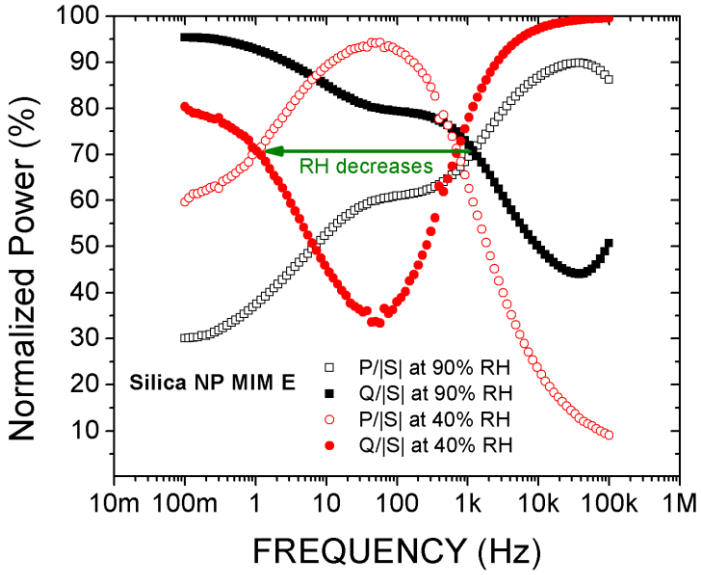

Figure 43. Normalized Power for the silica NP-MIM E sample at 90 and 40 % relative humidity (RH): Active power P/|S| and reactive power Q/|S|. The crossing point shifts to the left.

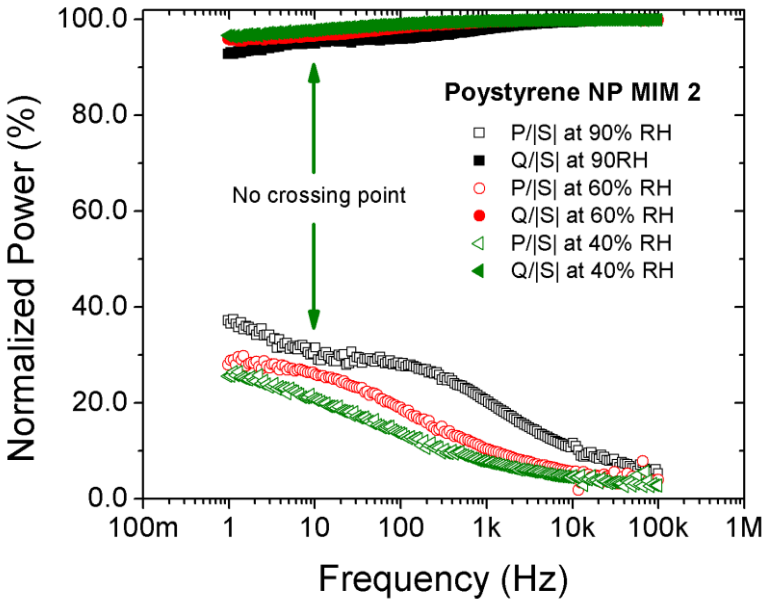

Figure 44. Normalized Powers at different relative humidity for the polystyrene NP-MIM 2 sample: Active power P/|S| and reactive power Q/|S|. There is not crossing point.

Appendix C.
Obtaining the transient response.

Fist at all, it is necessary to make the deduction of the equivalent circuit in the Laplace domain.

With 0<α<1, the definition of the Laplace-transform of the Grünwald-Letnikov fractional derivative is:

$$\mathrm{L}\{D^{\alpha}v(t)\} = s^{\alpha}V(s)$$

Where $D^{\alpha}v(t)$ means the derivate of the fractional order of the function $v(t)$.

If $v(t)$ is voltage, the CPE current is:

$$i_{cpe}(t) = Q_C \frac{d^{\alpha}v(t)}{dt^{\alpha}} = Q_C\left[D^{\alpha}v(t)\right]$$

The Laplace-transform of the CPE current is:

$$I(s) = L\left\{i_{cpe}(t)\right\} = L\left\{Q_C \frac{d^{\alpha}v(t)}{dt^{\alpha}}\right\} = Q_C L\left\{D^{\alpha}v(t)\right\} = Q_C s^{\alpha}V(s)$$

Therefore, the **CPE impedance** in the Laplace domain is:

$$Z_{CPE}(s) = \frac{V(s)}{I(s)} = \frac{V(s)}{s^{\alpha}Q_C V(s)} = \frac{1}{s^{\alpha}Q_C}$$

Similarly, the **Warburg impedance** in the Laplace domain is:

$$Z_W(s) = \frac{\sqrt{2}A_W}{s^{1/2}}$$

The impedance in the Laplace domain of the equivalent circuit for the silica NP MIM capacitors can be developed in the following steps:

$$Z(s)=\frac{1}{s^{\alpha 1}Q_{C1}}\|\left(R_1+\frac{\sqrt{2}A_W}{s^{1/2}}\right)+\frac{1}{s^{\alpha 2}Q_{C2}}\|(R_2)+\frac{1}{s^{\alpha 3}Q_{C3}}\|(R_3)$$

Where the symbol || means the impedance in parallel of two elements.

$$Z(s)=\frac{\frac{1}{s^{\alpha 1}Q_{C1}}\left(R_1+\frac{\sqrt{2}A_W}{s^{1/2}}\right)}{\frac{1}{s^{\alpha 1}Q_{C1}}+\left(R_1+\frac{\sqrt{2}A_W}{s^{1/2}}\right)}+\frac{\frac{1}{s^{\alpha 2}Q_{C2}}(R_2)}{\frac{1}{s^{\alpha 2}Q_{C2}}+(R_2)}+\frac{\frac{1}{s^{\alpha 3}Q_{C3}}(R_3)}{\frac{1}{s^{\alpha 3}Q_{C3}}+(R_3)}$$

$$Z(s)=\frac{\frac{R_1s^{1/2}+\sqrt{2}A_W}{s^{\alpha 1}Q_{C1}s^{1/2}}}{\frac{R_1Q_{C1}s^{\alpha 1+1/2}+\sqrt{2}A_WQ_{C1}s^{\alpha 1}+s^{1/2}}{s^{\alpha 1}Q_{C1}s^{1/2}}}+\frac{\frac{R_2}{s^{\alpha 2}Q_{C2}}}{\frac{1+R_2Q_{C2}s^{\alpha 2}}{s^{\alpha 2}Q_{C2}}}+\frac{\frac{R_3}{s^{\alpha 3}Q_{C3}}}{\frac{1+R_3Q_{C3}s^{\alpha 3}}{s^{\alpha 3}Q_{C3}}}$$

Finally, the **equivalent circuit impedance** in the Laplace domain is:

$$Z(s)=\frac{R_1s^{1/2}+\sqrt{2}A_W}{R_1Q_1s^{\alpha 1+1/2}+\sqrt{2}A_WQ_1s^{\alpha 1}+s^{1/2}}+\frac{R_2}{1+R_2Q_2s^{\alpha 2}}+\frac{R_3}{1+R_3Q_3s^{\alpha 3}}$$

This equation is used in the paper #1 (Impedance modeling of silica nanoparticle metal insulator metal capacitors).

Considering the resistor connected in series with NP MIM capacitor and the oscilloscope input resistance, the voltage transfer function is:

$$\frac{V_o(s)}{V_i(s)}=H(s)=\frac{R_O\|R_I}{Z(s)+R_O\|R_I}$$

The Matlab code to obtain the transcendent response to a square signal is as follows:

```
% Transfer function for silica NP-MIM C
clc;
clear;
% The parameters for this MIM:
Rs=0;
Ls=2E-8;
Q1=430E-9;
alf1=0.90;
R1=0.01E+6;
Aw=6.3E+6;
```

```
Q2=6.0E-9;
alf2=0.83;
R2=1.1E+5;
C3=20.0E-9;
R3=2.4E+4;
alf3=1;

t=0:0.001:2.5;
Z1=fotf([R1*Q1 sqrt(2)*Aw*Q1 1],[alf1+1/2 alf1 1/2],[R1 sqrt(2)*Aw],[1/2 0]);
Z2=fotf([R2*Q2 1],[alf2 0],R2,0);
Z3=fotf([R3*C3 1],[alf3 0],R3,0);
Z4=fotf(1,0,Rs,0);
Z5=fotf(1,0,[Ls 0],[1 0])
Z6=plus(Z1,Z2);
Z7=plus(Z3,Z4);
Z8=plus(Z5,Z6);
Z=plus(Z7,Z8);
Ri=910000;
Ci=14E-12;
%Gi=fotf([Ri*Ci 1],[1 0],Ri,0);
Gi=fotf(1,0,Ri,0);
GT=mrdivide(Gi,plus(Gi,Z))
y=1.2*step(GT,t);%la amplitude el escalon es 1.2V
figure(2);plot(t,y,'o');grid;
titulos={'tiempo', 'voltajeVo'};
datos(:,1)=t;
datos(:,2)=y;
xlswrite('mim_E',datos,'hoja0');
%Frequency Domain Identification
%mim_E=xlsread('mim_E','3er-modelo');
%mag=mim_E(1:268,2);
%phase=mim_E(1:268,3);
%w=mim_E(1:268,17);
%id=ffidata(mag,phase,w);
%Llamar a fotfrid
Ampli = 1.2;
tt=0:0.005:21;%
T=5;%
u = 0.5*square(2*pi()*tt/T)+0.5;
figure(3);plot(tt,u);grid;
ytren = Ampli*lsim(GT,u,tt);
figure(4);plot(t,y,'-',tt,ytren,':');grid;
datostren(:,1)=tt;
datostren(:,2)=ytren;
xlswrite('mim_E',datostren,'Hoja3');
%-------------------------------------
%señal del generador

%---------------
f=logspace(-1,6,268);
```

```
w=2*pi*f;
[mag,ph]=bode(Z,w);
H=bode(Z,w);
[re,im]=nyquist(H);
for i=1:268
   magnitud(i)=mag(:,:,i);
   fase(i)=ph(:,:,i);
   real(i)=re(:,:,i);
   imaginaria(i)=(-1)*im(:,:,i);
end
figure(1);semilogx(f,magnitud);
title('Manitud');xlabel('frecuencia'),ylabel('Magnitud');
figure(2);semilogx(f,fase);
title('Fase');xlabel('f'),ylabel('Fase');
figure(3);plot(real,imaginaria,'o');
title('Nyquist');xlabel('Real'),ylabel('Imaginaria');
```

Appendix D
Conference publications

1. Improving a nozzle tip with a guard ring for an electrospray system, Bremnen Véliz, Sandra Bermejo, Luis Castañer, 11va Spanish Conference on Electron Device, Barcelona-Spain, February 8th - 10th 2017, poster.

2. Improving and scaling-up the area of electrospray deposit of nanoparticles, Bremnen Véliz, Sandra Bermejo, Jordi Vives, Luis Castañer, 43rd International Conference on Micro and Nanoengineering, Braga-Portugal, September 18th - 22nd, 2017, poster.

3. Impedance spectroscopy of colloidal suspensions of silica and polystyrene nanoparticles, Bremnen Véliz, Sandra Bermejo, Copenhagen-Denmark, Micro and Nanoengineering Conference, September 24th - 27th, 2018, poster.

4. Metamaterials as an experimental field for fractional calculus, Bermejo S, Dominguez M, Véliz B, Fractional Calculus Meeting, Madrid-Spain, November 21th, 22th and 23th, 2018, talk.

5. Controlling electromagnetic waves with all dielectric metamaterials, S. Bermejo, S. Perera, M. Dominguez, B. Veliz, M. Cedeño, The Tenth Moscow Solar System Symposium, Moscow-Russia, October 7th – 11th, 2019, poster.

6. Metamaterials potential for photonics, energy and sensing, S. Bermejo, A. Orpella, M. Dominguez-Pumar, B. Veliz, M. Cedeño, S. Perera, J. Pons. The Biorobotics Institute, Pontedera, Italia, 23/07/2019, talk.

7. Metamaterials for photonic and energy applications, S. Bermejo, M. Dominguez-Pumar, A. Orpella, B. Veliz, M. Cedeño, S. Perera, MMS -25th World Micromachine Summit, Xi'an, China, 5-9 May, 2019, talk.

8. Nanoparticles based supercapacitors for energy harvesting, S. Bermejo, M. Dominguez, B. Véliz, M. Cedeño, Mars Atmospheric Science and Recent Mars Missions (EUROPLANET) Workshop, Madrid-Spain, May 21th - 24th, 2019, talk.

Appendix E
Thesis related projects and scholarships

Electrosprayed metal-nano-particle metal (eMIM) capacitor for energy storage. Bermejo S., Dominguez M., Orpella A., Véliz B., Cedeño M., programme of the European Space Agency (ESA) AO/1-8876/17/NL/CRS, 2019.

Solar cells with back contacts based on thin crystalline silicon substrates. State Research Agency, TEC2017-82305R, 2018-2020.

Science and technology of space instruments for the characterization of the Martian environment in multiple NASA missions: 3D Wind Sensor. Ministry of Economy and Competitiveness, ESP2016-79612-C3-2-R, 2016-2019.

Instrumentation to characterize the marcian environment in NASA missions. State Research Agency, RTI2018-098728-B-C33, 2019-2021.

SENESCYT scholarship, open call 2014 second phase, agreement 2016-AR5G8871.